Nuclear modification of electron yields from charm and bottom hadrons in Au+Au collisions at $\sqrt{s_{NN}} = 200$ GeV

Hidemitsu Asano

Depertment of Physics, Kyoto University

A dissertation submitted in partial fulfillment of the requirements for the degree of Doctor of Science

Janually, 2015

Contents

List of Figures

viii

List of Tables

Acronyms and Abbreviations

Acronyms and abbreviations used in this dissertation:

AGS Alternating Gradient Synchrotron.

ALICE A Large Ion Collider Experiment (at the LHC).
BBC Beam-Beam Counters (subsystem of PHENIX).

BNL Brookhaven National Laboratory.

BRAHMS Broad RAnge Hadron Magnetic Spectrometers (experiment at RHIC).
CMS Compact Muon Solenoid (experiment at the LHC).
DCA Distance of Closest Approach.

DCH Drift Chamber (subsystem of PHENIX).
EMCal Electromagnetic Calorimeter (subsystem of PHENIX).
LHC Large Hadron Collider.

LHCb Large Hadron Collider beauty experiment.
MB Minimum Bias.
PC Pad Chamber (subsystem of PHENIX).

PDF Parton Distribution Function.

PHENIX Pioneering High Energy Nuclear Interaction eXperiment (at RHIC).

pQCD pertavative Quantum Chromodynamics.
QCD Quantum Chromodynamics.

QGP Quark Gluon Plasma.
RHIC Relativistic Heavy Ion Collider.

RICH Ring Image Čherenkov Detector (subsystem of PHENIX).
SPS Super Proton Synchrotron (CERN).

STAR Solenoidal Tracker at RHIC (experiment).
VTX Silicon Vertex Tracker (subsystem of PHENIX).

Nomenclatures

Nomenclatures used in this dissertation:

$N_{\mathbf{coll}}$ Number of binary collisions.

$N_{\mathbf{part}}$ Number of participants.

NN Nucleon-Nucleon (collision).

p_T transverse momentum.

$\sqrt{s_{NN}}$ Center of energy per nucleon pair.

T_c psudocritical temperature.

$\mathbf{DCA}_L$ DCA along the beam axis.

$\mathbf{DCA}_T$ DCA in transverse plane.

Abstract

This dissertation details the measurement of electrons from semileptonic decay of charm and bottom hadrons from Au+Au collisions at $\sqrt{s_{NN}} = 200$ GeV by using the PHENIX detector in the relativistic heavy ion collider (RHIC).

Heavy quarks (charm or bottom) are one of suitable probes of a Quark Gluon Plasma (QGP). Due to their large masses, the production process of heavy quarks is restricted to initial nucleon-nucleon collisions. Thus, heavy quarks carry information about the entire time-evolution of the medium.

We previously measured the yields of electrons from semileptonic decays of charm and bottom hadrons inclusively in Au+Au collisions at $\sqrt{s_{NN}} = 200$ GeV. It indicated substantial modification in the momentum distribution of the parent heavy quarks due to the QGP created in these collisions. However, at that time, PHENIX was not able to distinguish electrons from charm and bottom hadrons independently. In order to understand these medium effects in more detail, the separation of electrons from charm and bottom hadrons are aimed to reveal the mass dependence of energy loss in the medium.

For the first time, by using the Silicon Vertex Tracker (VTX) installed in PHENIX to measure precision displaced tracking, we have succeeded in separating the electrons from charm and bottom hadrons in Au+Au collisions at $\sqrt{s_{NN}} = 200$ GeV in the transverse momentum (p_T) from 1 GeV/c to 8 GeV/c at midrapidity region ($|\eta| < 0.35$). The invariant yield of charm and bottom hadrons as a function of p_T were calculated. Based on this separation, the fraction of the electrons from bottom hadrons were obtained. Further, by using that for $p+p$ collision, the nuclear modification factor R_{AA} was extracted both for charm and bottom electrons.

We have observed that bottom electron is suppressed for higher p_T region ($p_T > 4$ GeV/c) in Au+Au collisions compared to $p+p$ collisions for the first time in RHIC energy. While the magnitude of suppression is smaller than that of charm in the region of $3 < p_T < 4$ GeV/c , it is similar for higher p_T region within systematic uncertainty.

Chapter 1

Overview

According to the lattice Quantum Chromodynamics (QCD) calculations [16, 17], quarks and gluons are deconfined at the high temperature above ~ 150 MeV. To date, it is well established that heavy Ion collisions at the Relativistic Heavy Ion Collider (RHIC) and the Large Hadron Collider (LHC) create a new state of matter -QGP- that is described as an equilibrated system with initial temperature in excess of $340 - 420$ MeV [18–22].

This QGP follows hydrodynamical flow behavior with extremely small dissipation, characterized by the shear viscosity to entropy density ratio η/s and is thus termed a near-perfect fluid [18, 23–25].

However, these recently established knowledge of QGP still raises new questions about the property of QGP and how QCD works in this environment.

Heavy flavor hadron (D, B) measurement has several advantages to light hadrons $(\pi, K...\text{etc.})$ to investigate the property of the QGP because of their specific production mechanism. The heavy quarks $(Q = c, b)$ are mainly produced via hard scatterings at the initial nucleon-nucleon collisions, because the large momentum transfer is needed to produce heavy quarks [26]. This heavy quarks are clean probes which experience the entire time-evolution of the QGP as they pass through it.

The PHENIX collaboration has measured transverse momentum distribution of electrons[1] from semileptonic decay of charm and bottom hadrons produced in Au+Au collisions and observed it is significantly modified compared with $p+p$ collisions from the year 2004/2005 data at RHIC. This result was unexpected, because in the perturbative QCD based calculation, parton energy loss in the QGP is believed to be dominated by gluon radiative energy loss [27], which was predicted much smaller for heavy quarks than

---

[1] Here and throughout this dissertation, "electrons" is used to refer to both electrons and positrons.

that for light partons [7]. In the past measurements before the year 2010, the PHENIX was not able to distinguish electrons from charm and bottom hadrons independently in Au+Au collisions.

In order to separate the contribution from charm and bottom, the PHENIX collaboration has developed the silicon vertex tracker (VTX) [28] and installed it covering at midrapidity region in 2010. The VTX was designed to give precise tracking reconstructions of the distance of closest approach (DCA) to the collision vertex. This enables the separation of electrons from semi-leptonic decay of charm and bottom hadrons statistically in Au+Au collisions, because the decay kinematics and life time of charm ($c\tau_{D^0} = 123$ μm, $c\tau_{D^\pm} = 312$ μm) and bottom ($c\tau_{B^0} = 455$ μm, $c\tau_{B^\pm} = 491$ μm) hadrons are different [3].

In the result, the suppression of electrons from bottom hadrons is observed for higher p_T region ($p_T > 4$ GeV/c) in Au+Au collisions compared to $p+p$ collisions for the first time in RHIC energy. It strongly implies bottom quarks suffer energy loss in the QGP medium. The magnitude of suppression is smaller than that of charm in the region of $3 < p_T < 4$ GeV/c and similar for higher p_T region within systematic uncertainty. The new analysis method using the VTX detector was established and the same method can be applied for high statistics data taken in 2014/2015.

This dissertation details the first measurement of electrons from semileptonic charm and bottom hadron decays from $Au + Au$ collisions at $\sqrt{s_{NN}} =$ 200 GeV in year 2011 using the VTX detector. The organization of this dissertation is as follows: In Chapter 2, physics backgrounds of the QGP and heavy ion collisions are reviewed.

In Chapter 3, heavy quark as a probe of the QGP and past measurements at RHIC and the LHC are reviewed. In the measurements at RHIC, charm and bottom contribution was not separated. The motivation of charm/bottom separation are also explained in this chapter.

In Chapter 4, the accelerator RHIC, the relevant PHENIX apparatus in year 2011 and the VTX detector which was installed in the end of year 2010 are introduced.

In Chapter 5, the analysis method to separate the contribution of electrons from charm and bottom using PHENIX central arms and the VTX are explained. After that, the unfolding procedure using electron DCA distributions and p_T spectra are explained.

In Chapter 6, results of invariant yield of charm and bottom hadron, bottom electron fraction, and nuclear modification factor of charm electrons and bottom electrons in Au+Au collisions are shown.

Chapter 7 is for dicussions about these results. The consistency check with previously published results of invariant yield of heavy flavor electrons

and STAR D_0 measurement shown. After that, comparison of theretical models are shown.

The conclusion of this measurement are described in Chapter 8.

Major Contributions

The major part of this dissertaion is based on the published paper "Single electron yields from semileptonic charm and bottom hadron decays in Au+Au collisions at $\sqrt{s_{NN}} = 200$ GeV by A. Adare et al." [29]. The major contributions of the author as a PHENIX collaborator are listed as follows:

- Construction, quality assurance and maintenance of pixel detectors (inner two layers of the VTX detector).

- Development of online monitoring system of pixel detectors.

- Commissioning and operation of the VTX detector during 2011 - 2014.

- Calibration of VTX sensors alignment.

- Establish the analysis method of electron DCA distributions using VTX detector.

- Publication of the paper "Single electron yields from semileptonic charm and bottom hadron decays in Au+Au collisions at $\sqrt{s_{NN}} = 200$ GeV" [29] with paper preparation group in PHENIX.

Chapter 2

Quark Gluon Plasma and Heavy Ion Collision

This chapter is dedicated to giving a brief introduction to the Quark Gluon Plasma (QGP) and the high enegy heavy ion collision. In section 2.1, the current understanding of QGP based on Quantum Chromodynamics (QCD) is reviewed. In section 2.2, the basic picture of space-time evolution of the matter created in heavy ion collisions is described. After that the geometry of collisions, which is important to understand the experimental results are explained. In the last section 2.3, the states of created matter in RHIC is explained from three important experimental results; jet quenching, strong collectivity, and temperature.

2.1   Quark Gluon Plasma

High energy Heavy Ion Collision experiments aim to create and investigate the property of a high temperature matter which consists of deconfined quarks and gluons. The new state of deconfined quarks and gluons is called a QGP. QGP is expected based on the "Asymptotic freedom" property of QCD. Asymptotic freedom was discovered in early 1970s by Gross, Wilczek and Politzer [30–32], and means that the QCD coupling constant α_s decreases with increasing the momentum transfer Q, as shown in Figure 2.1. The discovery of asymptotic freedom arises the expectation; asymptonic freedom makes interaction at very short distances (or high momenta) arbitrarily weak, so that if the temperature or net baryon density is high enough, a transition should occur from normal nuclear matter, where quarks and gluons are confined in hadrons, to the new state of matter where the quarks and gluons are deconfined [33, 34].
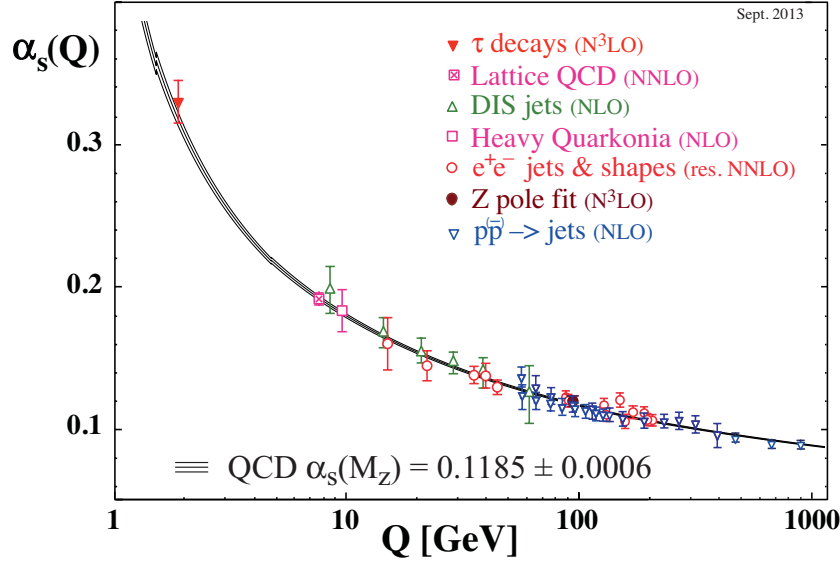
Figure 2.1: Summary of measurements of α_s as a function of the momentum
transfer Q from PDG2014 [3]. Also shown in bottom is the α_s value when
$Q^2 = M_z$ (M_z is Z boson's mass, NLO: next-to-leading order; NNLO: next-
to-next-to leading order; res.NNLO: NNLO matched with resummed next-
to-leading logs; N³LO: next-to-NNLO).

Lattice QCD calculations predict that the transition from a low tempera-
ture hadronic phase to a QGP phase should occur at a temperature of ~ 150
MeV for zero net baryon density. In early expectations, this transition could
be first−order phase transition between normal nuclear matter and QGP
phase. The QCD transition at finite-temperature and low baryon chemical
potentials (μ_b) is, however, not a real phase transition, but a rapid crossover,
meaning that it involves a rapid and smooth change, as opposed to a disconti-
nuity, as the temperature is varied [35]. μ_b at RHIC (~ 45 MeV [36]) is much
smaller than typical hadron mass. Even though there is no well-defined sep-
aration of phases because of the crossover behavior of the transition, recent
lattice QCD results by Budapest-Wuppertal collaboration [37] and HotQCD
collaboration [1], for example, show that thermodynamic properties (pres-
sure, energy density, and entropy density) really change rapidly around the
crossover region. Figure 2.2 shows the lattice QCD results on pressure, en-
ergy density, and entropy density normalized by $1/T^4$ by HotQCD Collabo-
ration [1].

Instead of genuine critical temperature at which phase transition occurs,
"pseudocritical temperature" is used to depict the phase diagram of QCD.

While there are several definitions of pseudocritical temperature T_c, an example of the pseudocritical temperature $T_c = 154 \pm 9$ MeV is shown as a vertical band in the Figure 2.2. This T_c is defined for chiral phase transition, at which up, down and strange quarks rapidly acquire their physical masses, taking chiral symmetry as order parameter [17]. There is another way to define the T_c, for example, as the inflection point of ϵ/T^4 and $(\epsilon - 3p)/T^4$, where p is the pressure and ϵ is energy density [16].
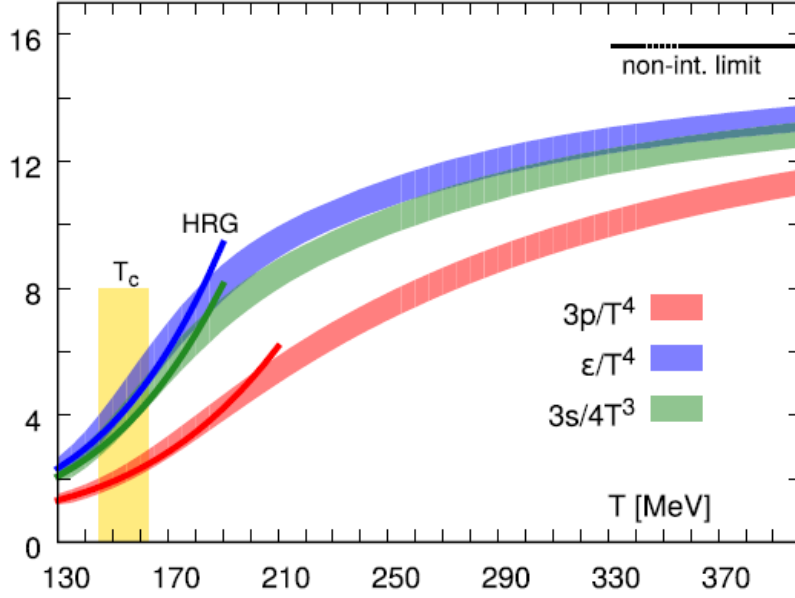
Figure 2.2: Lattice QCD results from Hot QCD collaboration [1]. The figure shows pressure, energy density, and entropy density normalized by $1/T^4$ as a function of the temperature. The dark lines show the prediction of the hadron resonance gas (HRG) model. The horizontal line at $95\pi^2/60$ corresponds to the ideal gas limit for the energy density and the vertical band marks the crossover region, $T_c = 154 \pm 9$ MeV (see also texts) .

While deconfinement and chiral phase transition have not been directly observed in RHIC and the LHC experiments, there have been several experimental results which strongly indicate the creation of QGP. Three important observations which are understood as evidence of QGP found in Au+Au collisions at RHIC, jet quenching, strong collectivity, and temperature are discussed in section 2.3. An overview of the evidence for the creation of quark-gluon matter at RHIC can be found in those summary papers [18, 19, 38, 39] from four experiments at RHIC.

2.2 High energy Heavy Ion Collision experiment

2.2.1 Nuclear stopping power

In order to create a QGP state in heavy ion collisions, sufficient energy
must be released from the two colliding nuclei into the QGP. The kinetic
energy that is removed from the nuclei depends on the amount of stopping
power between the colliding nuclei.

The stopping power can be estimated from the rapidity loss experienced
by the baryons in the colliding nuclei. The rapidity, y, of a particle is defined
as:

$$y = \frac{1}{2} \ln \frac{E + p_z}{E - p_z},$$

where E and p_z are energy and z component of momentum, respectively.

The average rapidity loss, δy, is defined as the difference, $\delta y = y_p - \langle y \rangle$
between the incoming beam rapidity y_p and the average rapidity after the
collision which is expressed as [39].

$$\langle y \rangle = \int_0^{y_p} y \frac{dN}{dy} dy \Big/ \int_0^{y_p} \frac{dN}{dy} dy$$

Here dN/dy denotes the number of net-baryons (number of baryons minus
number of antibaryons) per unit rapidity.

Figure 2.3 shows the measurement of net protons (number of protons $-$
number of anti-protons) rapidity distribution at AGS ($\sqrt{s_{NN}} = 5$ GeV Au+Au),
SPS ($\sqrt{s_{NN}} = 17$ GeV Pb+Pb) and RHIC ($\sqrt{s_{NN}} = 200$ GeV Au+Au)
data [40]. One can assume the rapidity distribution of net neutrons, net
Λs, net Σs are similar with net protons. Thus the net proton distributions
represents the net baryon distributions.

The distributions yield a strong beam energy dependence as shown in
Figure 2.3. At RHIC (red points), the distribution is almost flat up to $y \sim 3$.
It means incident nucleons do not lose all their kinetic energy and baryon
chemical potential (μ_b) at RHIC ($\mu_b \sim 25$ [39] $- 45$ MeV [36]) is quite smaller
than AGS and SPS at midrapidity. In analogy to optics, it is often said that
a nucleus becomes transparent in high energy collisions.

The average rapidity loss measured by BRAHMS is $\delta y = 2.0 \pm 0.1$. The
energy loss per participant nucleon is estimated to be ~ 70 GeV from the
rapidity loss and transverse momentum spectra of baryons [40]. Thus, the
total kinetic energy loss of two incoming nuclei at RHIC is estimated to be
~ 28 TeV (70 GeV $\times 2 \times 197$) in most central ^{197}Au $+^{197}$ Au collision.
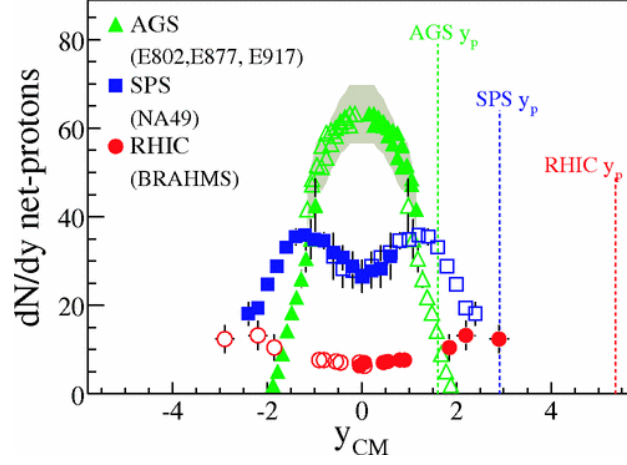
Figure 2.3:   The net-proton (number of proton $-$ number of anti-proton) rapidity distribution at AGS (green, Au+Au at $\sqrt{s_{NN}} = 5$ GeV), SPS (blue, Pb+Pb at $\sqrt{s_{NN}} = 17$ GeV), and RHIC measured by BRAHMS (red, Au+Au at $\sqrt{s_{NN}} = 200$ GeV) [40]. The data are most central collisions (0-5 % centrality. See subsection 2.2.3 for the definition of centrality). y_p denotes beam rapidity.

2.2.2   Picture of space-time evolution

The kinetic energy removed from two incoming nuclei is converted into other degree of freedom. This subsection overviews the basic space-time picture from initial collisions in partonic levels to freeze out in hadronic phase originated from the kinetic energies released in heavy ion collisions. Figure 2.4 is a simplified sketch of this sequence.
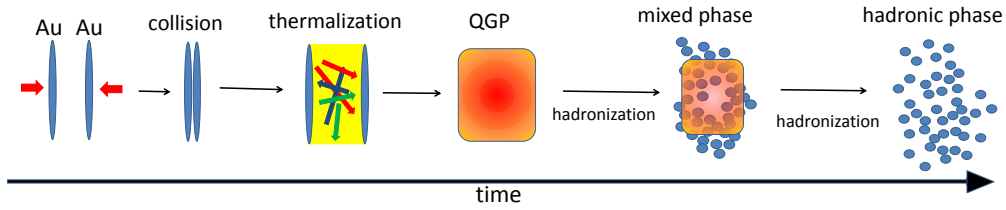
Figure 2.4:   Time evolution of heavy ion collision from initial nucleus-nucleus collision to hadronic freeze out

In high energy heavy ion collisions, two incoming nuclei are Lorentz-contracted along the collision axis. Figure 2.5 shows the parton distribution functions (PDF), which describe the initial distribution of quarks and gluons
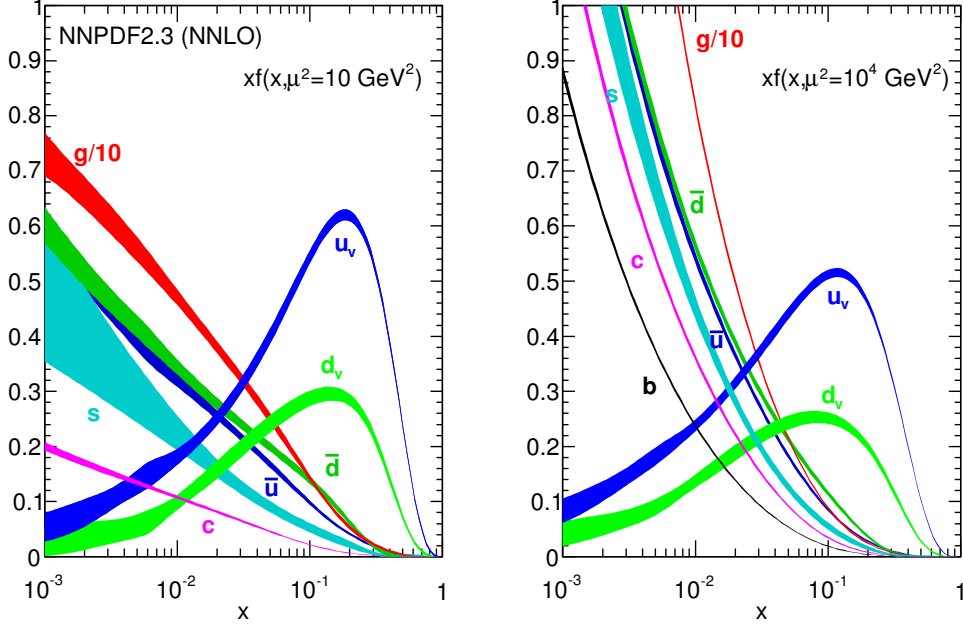
Figure 2.5:   Parton distribution function times Bjorken-x as a function of Bjorken-x obtained in NNLO NNPDF2.3 global analysis [2, 3]

in colliding two protons as a function of Bjorken-x. [1] Bjorken-x is the fraction of the nucleon's momentum carried by the struck parton:

$$x = \frac{Q^2}{2p \cdot q}.$$

Here q is the transfer of four-momentum. p is the four-momentum of a nucleon, and $Q^2 = -q^2$. As shown in Figure 2.5, there are a lot of small Bjorken-x gluons. Most of the produced hadrons at RHIC and LHC at midrapidity region are originated from those gluons.

At the initial nucleon-nucleon (NN) collision, scattering of these partons take place. After that, those partons suffer multiple elastic and inelastic scattering generating a lot of softer partons. They are supposed to be in the local thermal equilibrium within the time scale $\tau \sim 1$ fm/c $= 1/\Lambda_{QCD}$. This process is called thermalization of partons and the typical time scale for the system to relax to the local equilibrium distribution is called relaxation time. As will be discussed in 2.3.2, the assumption of rapid realization of

---

[1]The PDF for free protons are known to be modified for protons bound in nucleus [41]. Such effects which are not due to the production of a QGP are termed initial state effects.

local thermal equilibrium ($\sim$0.6 – 1 fm/c) works well to describe azimuthal
anisotropy (v_2) of produced hadrons at RHIC in hydrodynamical model.

Phenomenologically, the energy density after the initial NN collision can
be roughly estimated through Bjorken's formula [42]

$$\epsilon_{Bj}(\tau) = \frac{1}{c\tau A_\perp}\frac{dE_T}{dy},$$

where $\tau = \sqrt{t^2 - z^2}$ is the proper time, and $A_\perp$ is nuclei transverse overlap
area. E_T is a sum of transverse energies of all particles emitted in an event.
$\frac{dE_T}{dy}$ is the transverse energy per unit rapidity.

Figure 2.6 shows the PHENIX data on $\epsilon_{Bj}\tau$ as a function of number of
participants N_p at three collision energy [4]. If τ is around 1 fm/c, energy
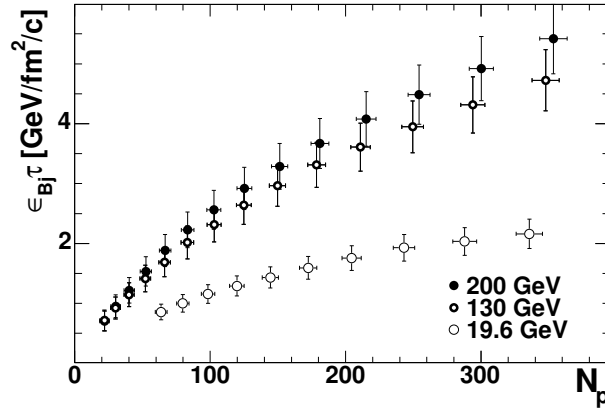
Figure 2.6:   Energy density as a function of the number of participants N_p
from PHENIX data [4].

densities at $\sqrt{s_{NN}}$=130 and 200 GeV are above 1 GeV/c /fm^3 except for
very peripheral collision. According to the lattice QCD calculation (Figure 2.2), the energy density around the pseudocritical temperature T_C is
~ 0.3 GeV/fm^3. The PHENIX data indicate energy density to be realized at
RHIC is high enough to create a QGP.

As the QGP system expands, the energy density and temperature decrease. When the temperature gets smaller than T_c, quarks are confined
and color neutral hadrons are produced. The cooling down process is called
"freeze out". It is expected to happen gradually, in the later stage of collision, so that confined phase and deconfined phase are mixed (mixed phase),
as illustrated in Figure 2.4,.

The hadronization process is explained by fragmentation and recombination of partons [43]. As shown in Figure 2.7, transverse momentum p_T

spectrum above 6 GeV/c is dominated by fragmentation, which can be fit
by a power law function as it is characteristic in pQCD at large transverse
momentum. The region below 4 GeV/c is dominated by so-called recombi-
nation (coalecense) process.
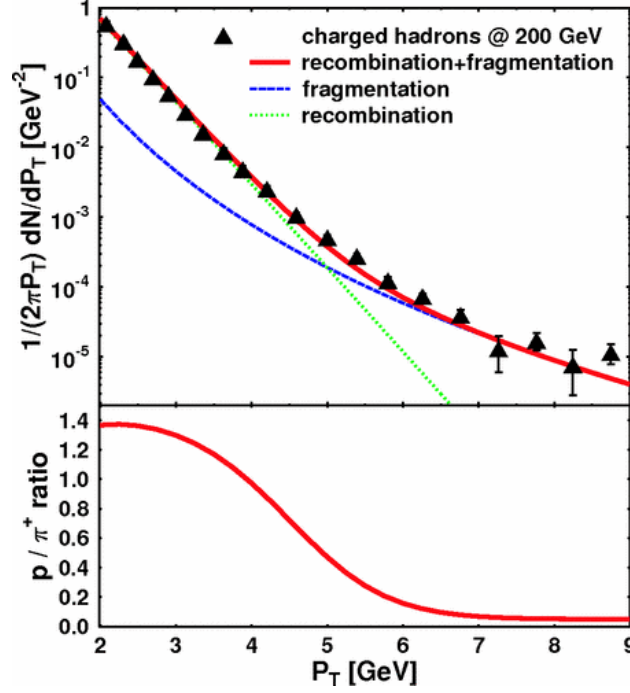
Figure 2.7: p_T spectrum of inclusivce charged hadrons and theoretical ex-
planation from [43]. Top: inclusive charged hadron p_T spectrum in central
Au+Au collisions at $\sqrt{s_{NN}}$ = 200 GeV from PHENIX data [44]. Bottom:
ratio of proton to π^+ as a function of p_T.

In the recombination picture, three quarks or a quark-antiquark pair
which are close enough in a phase space can form a baryon or meson, respec-
tively. The p_T spectrum of hadron generated from recombination falls off
faster than fragmentation with increasing p_T. Eventually, the total amount
of hadrons are fixed after the hadronization process. After that, produced
hadrons are allowed to free-stream and particle spectra at this moment are
seen by the detector.

2.2.3   Collision Geometry

The geometry of the collision must be taken into account in the analysis
and interpretation of the experimental data. The impact parameter (b in

Figure 2.8) can be changed from 0 to the transverse nuclear size. The space-
time evolution of collision may be different in central and peripheral collisions.
In the centre-of-mass frame, owing to Lorentz contraction in the longitudinal
direction, the two nuclei can be seen as two thin disks of transverse size
$2R_A \simeq 2A^{1/3} fm$. Some relevant quantities which characterize the collision
geometry are listed below:

1. N_{part}: The number of participant nucleons involved in a heavy ion
   collision. This is the total number of protons and neutrons which take
   part in the collision.

2. N_{coll}: The total number of binary collisions (NN collisions).

3. centrality: The value to quantify the overlap of two colliding nuclei.
   As illustrated in Figure 2.9, centrality takes a range from 0% to 100%
   as the impact parameter ranges b=0 to b $= R_A + R_B$. 0% centrality
   means the most central collision. When collisions are not selected by
   centrality, it is called minimum bias (MB) collision (or event).

The geometrical quantities listed above (N_{part},N_{coll}, centrality) are usually
estimated by a probabilistic model generally called "Glauber model" [5, 45,
46].

The Glauber Model

In Glauber model, a collision of nucleus A and nucleus B is treated as
the multiple independent nucleon-nucleon interactions. The nucleons travel
on straight-line trajectories and do not change their trajectories after the
collisions at all. This approximation works well since the crossing time of
Au+Au is 0.12 fm/c at $\sqrt{s_{NN}} = 200$ GeV and the nucleon can move to
transverse direction 0.12 fm at maximum. This is much smaller than the
radius of nucleon ($\sim$ 0.8 fm). The simplest version of the Monte Carlo
approach, a nucleon-nucleon collision takes place if the nucleons' distance, d
in the plane orthogonal to the beam axis satisfies

$$d \leq \sqrt{\sigma_{in}^{NN}/\pi},$$

where σ_{in}^{NN} is the total inelastic nucleon-nucleon cross section in vacuum. At
RHIC, it is assumed $\sigma_{in}^{NN} = 42$ mb at 200 GeV which is extracted from fits
to the total and elastic cross section of other experiments [3]. Secondary
particle production and possible excitation of nucleons are not considered in
this model.
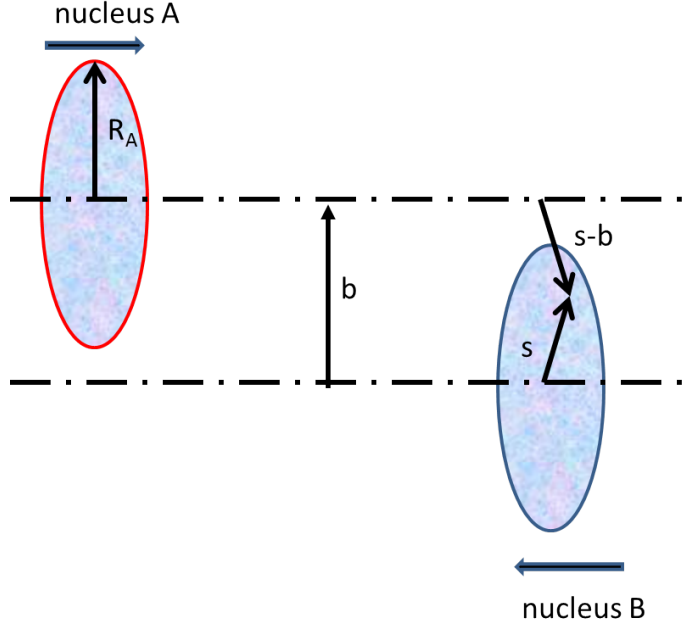
Figure 2.8: Geometry of a collision between nucleus A and B.

The probability per unit transverse area of finding a nucleon at the transverse position $\mathbf{s}$ in Figure 2.8 is

$$T_A(\mathbf{b}) = \int dz\rho(z, \mathbf{s}),$$

where $\rho(z, \mathbf{s})$ is the nucleon number density at location $(z, \mathbf{s})$ ($\int d^3r\rho(z, \mathbf{s}) = 1$).

Then, the product $T_A(\mathbf{s})T_B(\mathbf{s} - \mathbf{b})d^2\mathbf{s}$ gives the probability per unit area of nucleons being located in the overlapping area of nucleus A and nucleus B. Integrating this product over all values of $\mathbf{s}$ defines the nuclear overlap function, $T_{AB}(\mathbf{b})$, with impact parameter, $\mathbf{b}$ as follows:

$$T_{AB}(\mathbf{b}) = \int T_A(\mathbf{s})T_B(\mathbf{s} - \mathbf{b})d^2\mathbf{s},$$

For a heavy and spherical nucleus such as Au or Pb, the Woods-Saxon parametrization is a good approximation:

$$\rho_A(r) = \frac{\rho_{nm}}{1 + \exp{(r - R_A)/a}},$$

where $\rho_{nm} = 0.16$ fm^{-3} is the normal density of nuclear matter. R is the nuclear charge radius, a is the skin depth: for ^{197}Au, $R = 6.38$ fm and $a = 0.535$ fm [47].

The number of participants (N_{part}), and the number of binary nucleon-nucleon collisions, (N_{coll}), in the Glauber model are expressed as follows,

$$
\begin{aligned}
N_{\text{part}}(b) \quad &= \int d^2\mathbf{s}\, T_A(\mathbf{s})\left(1 - \exp\left(-\sigma_{NN}^{in} T_B(\mathbf{s})\right)\right) \\
&+ \int d^2\mathbf{s}\, T_B(\mathbf{s} - \mathbf{b})\left(1 - \exp\left(-\sigma_{NN}^{in} T_A(\mathbf{s})\right)\right),
\end{aligned}
\tag{2.1}
$$

$$
\begin{aligned}
N_{\text{coll}}(b) \quad &= \int d^2\mathbf{s}\, \sigma_{NN}^{in} T_A(\mathbf{s}) T_B(\mathbf{s} - \mathbf{b}) \\
&= \sigma_{NN}^{in} T_{AB}(b).
\end{aligned}
\tag{2.2}
$$

Figure 2.10 shows the number of binary nucleon-nucleon collisions (N_{coll}) and the number of participants (N_{part}) in Au+Au collisions as function of impact parameter.

2.2.4 Nuclear Modification Factor: R_{AA}

Once the number of binary collisions (N_{coll}) is obtained from Glauber model, experimental observables in Au+Au can be compared with those in $p+p$ as baseline, by using nuclear modification factor R_{AA}, which is defined as

$$
R_{AA}(p_T, y; b) = \frac{d^2 N_{AA}/dy dp_T}{N_{\text{coll}} \times d^2 N_{pp}/dy dp_T}.
$$

The numerator represents the observed hadron (or photon, lepton) spectra for species X in nucleus-nucleus collision, and the denominator represents the corresponding spectra produced in proton-proton collision scaled with the number of binary collisions (N_{coll}). Since hard scattering, QCD process which involves large momentum transfer, is point-like with distance scale $1/p_T \leq 0.1$ fm, the cross section $p(d)+A$ or $A+B$ collisions, compared to $p+p$, is proportional to the relative number of possible point-like encounters. This binary-scaling property in Au+Au collisions is seen in high-p_T direct photon spectra (subsection 2.3.3) and total yield of charm (section 3.1).

2.3 States of created matter at RHIC

2.3.1 Jet quenching and energy loss

At RHIC, high p_T particles ($p_T \geq 5$ GeV/c) are produced from hard collision processes. In this subsection, parton production and its energy loss
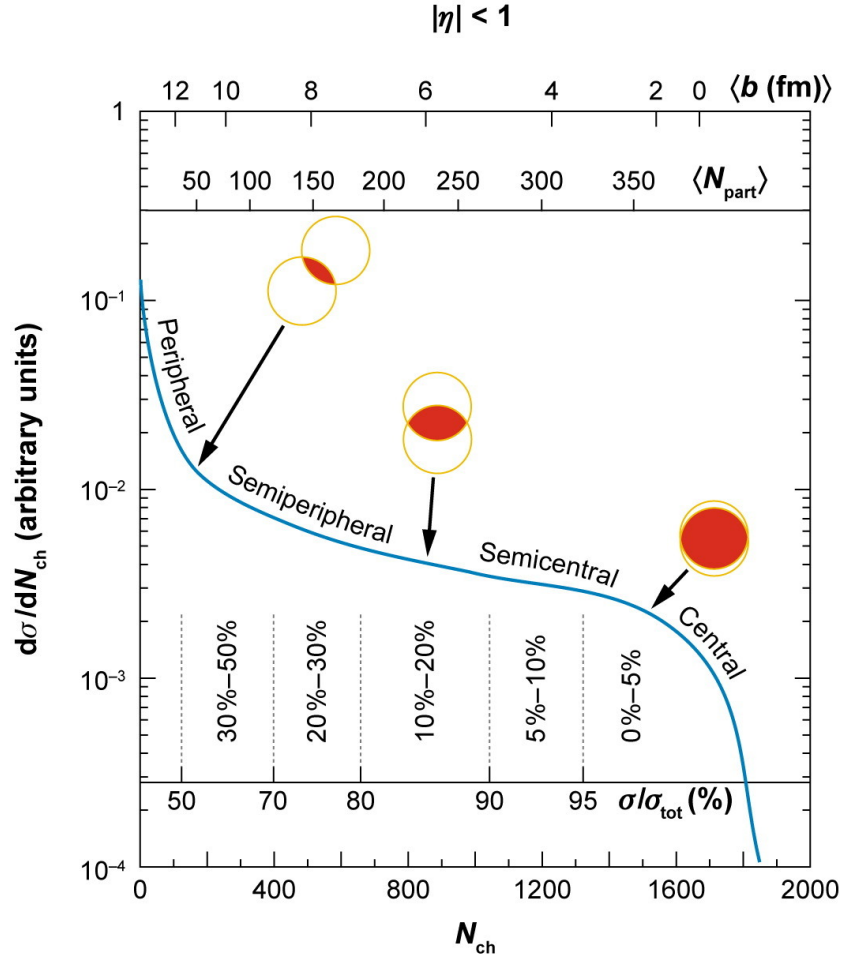
Miller ML, et al. 2007.
Annu. Rev. Nucl. Part. Sci. 57:205–43

Figure 2.9: An illustrated example of the relationship of the impact parameter (b), N_{part}, overlap area of colliding nucleus, the multiplicity distribution and centrality taken from [5].

Figure 2.10:   Number of participants (N_{part}) and Number of binary colli-
sions (N_{coll}) for Au+Au and Cu+Cu collisions from Glauber Monte Carlo
calculation [5]. The lines represent the mean values.

in the medium in nucleon-nucleon collision is reviewed. After that, so-called
jet quenching discovered in Au+Au collision at RHIC is also discussed.

The definition of jet is ambiguous. Here the most commonly used defini-
tion for hadron-hadron collision is introduced [48, 49]: a jet is a concentration
of transverse energy E_T in a cone of radius R, where

$$R = \sqrt{(\Delta\eta)^2 + (\Delta\phi)^2}.$$

Here ϕ is the azimuthal angle and η is the pseudorapidity variable:

$$\eta = -\ln\tan(\theta/2).$$

In the two-dimensional η, ϕ plane, curves of constant R are circles around the
axis of the jet. Jet production in hadronic collisions is a hard QCD process.
An elastic parton scattering $(2 \rightarrow 2)$ or inelastic parton scattering $(2 \rightarrow 2 +
X)$ of two partons from each of the colliding nuclei results in the production
of two or more high-p_T partons in the final state. The jet observable can
not be the residue of a single parton because of color conservation, energy
momentum conservation, and quantum-mechanical interference [50].

One of major discoveries that established the formation of dense partonic
matter at RHIC is the strong suppression of high-p_T particles in central

16

Au+Au collisions [44, 51]. This phenomena is called "jet quenching", which
is originally suggested by Bjorken in 1980's [52].

Figure 2.11 shows the nuclear modification factor (R_{AA}) for π^0 in cen-
tral (0-10%) and peripheral (80-92%) Au+Au collisions and minimum-bias
d+Au collisions at mid-rapidity. The suppression provides direct evidence
that Au+Au collisions at RHIC have produced matter at extreme densities,
greater than ten times the energy density of normal nuclear matter [18, 53].
The R_{dA} measurement in Figure 2.11 provides a test of the possible con-
tribution of initial state nuclear effects to the observed suppression above
and demonstrates that there is no significant initial state effect of nuclear
parton distributions compared to the Au+Au R_{AA} with $p_T > 2$ GeV/c at
mid-rapidity. Thus, the suppression of high p_T hadrons in Au+Au collisions
is interpreted as final state effect of the produced dense medium. The data
suggest a small enhancement in d+Au collisions, consistent with expectations
due to the Cronin effect [54]. The Cronin effect is expected to come from the
multiple scattering of the incident partons while passing through the nucleus
before the collision, which smears the axis of the hard scattering relative to
the axis of the incident beam, leading to the enhancement in mid-rapidity
region [55, 56].

The suppression of the high p_T hadrons ($R_{AA} < 1$) from the fragmen-
tation of a parton is due to energy loss in the created matter in the reac-
tion. The energy loss of a particle in a medium, ΔE, provides important
information on its properties. In general, ΔE depends both on the particle
characteristics (energy E or transverse momentum p_T and mass m) and on
the plasma properties (temperature T, particle-medium interaction coupling
α, and path-length of the matter L). The recent theoretical developments
are reviewed in [49, 57]

The total energy loss ΔE of a particle traversing a plasma with temper-
ature T is the sum of collisional and radiative loss : $\Delta E = \Delta E_{\text{coll}} + \Delta E_{\text{rad}}$
Collisional energy loss is the energy loss process through elastic scatter-
ing inside a QGP of temperature [52, 58]. This was thought to domi-
nate at low particle momentum. Radiative energy loss happens through
the bremsstrahlung of gluons. This loss is believed to dominate at higher
momentum.

Compared to the radiative energy loss, collisions energy loss was usually
considered to be small for light flavor (leading) partons, especially when the
energy of the jet is sufficiently high. However in recent realistic calculation
of nuclear modification factor R_{AA} at RHIC and LHC energies, collisional
energy loss may give non-negligible contribution [59–61].

17
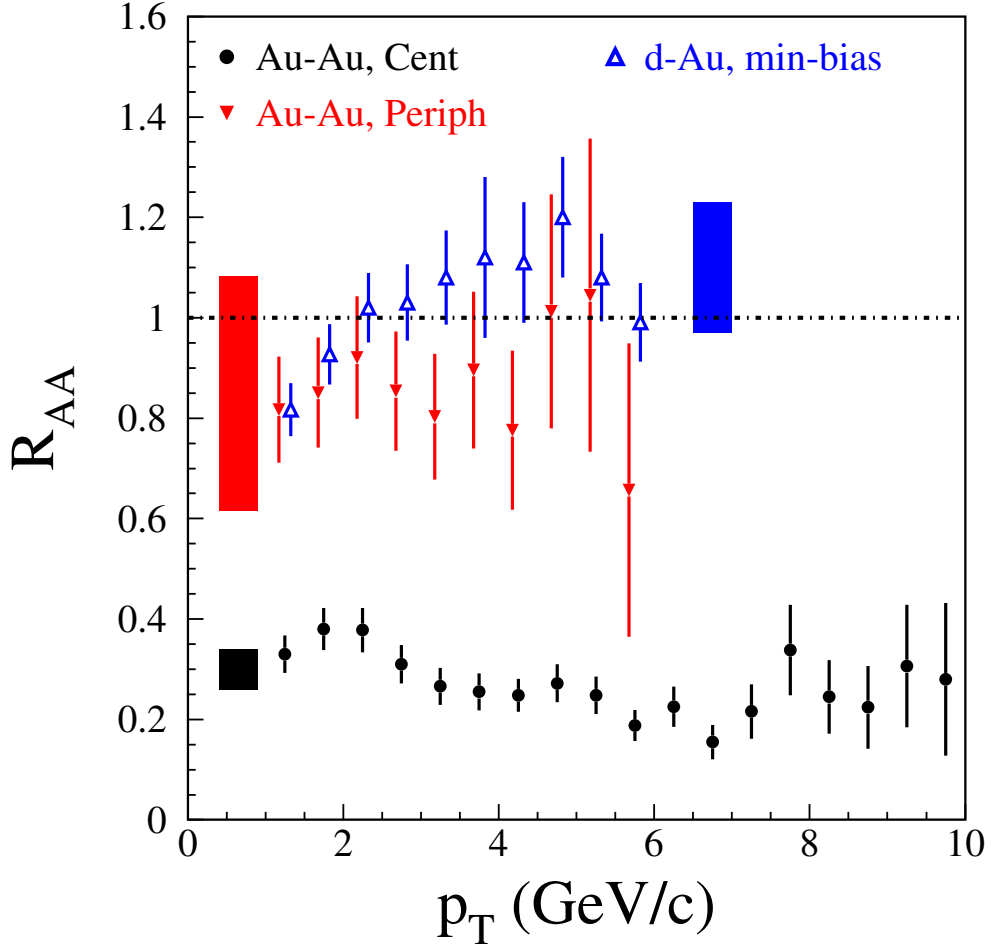
Figure 2.11: Nuclear modification factor, R_{AA}, for π^0 in central (0-10%) and
peripheral (80-92%) Au+Au collisions and minimum-bias d+Au collisions at
mid-rapidity. The shaded boxes on the left show the systematic errors for
the Au+Au R_{AA} values resulting from overall normalization of spectra and
uncertainties in the nuclear overlap function T_{AB}. The shaded box on the
right shows the same systematics error for the d+Au points. Reprinted from
[18] with permission from Elsevier.

2.3.2 Collectivity of the QGP

In addition to the discovery of jet quenching, RHIC experiments found
one more important observable related to the collectivity of created matter.
The collectivity is described by hydrodynamics and called "flow".

In Au+Au non-central collision, the reaction zone of nucleus-nucleus col-
lision is elliptic around the beam axis as illustrated in Figure 2.12. If the
mean free path among the produced particles is much larger than the typical
size of the system, the azimuthal distribution of particles does not depend on
azimuthal angle on average due to the symmetry of the production process.
On the other hand, if the mean free path is very small compared to the size
of reaction zone, hydrodynamics can be applied to describe the space-time
evolution of the system. In the absence of viscosity, initial multiple scatter-
ing of partons should transform the initial state spatial asymmetry (elliptic
shape) into asymmetry in momentum space [62], because the pressure gradi-
ent in x-axis is larger than y-axis as illustrated in Figure 2.13. This is called
"elliptic flow", which is quantitatively characterized by v_2 variable defined in
the following paragraph.
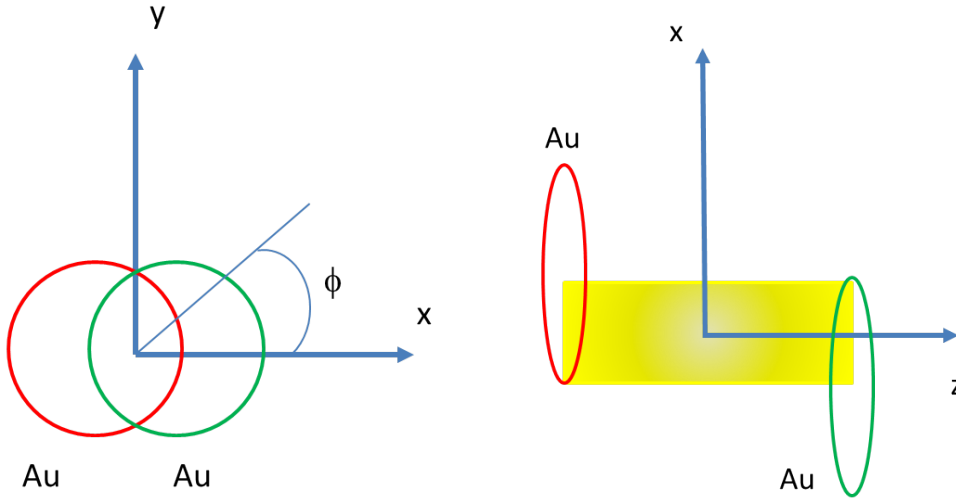
Figure 2.12: Illustration of the collision geometry in a non-central heavy ion
collision. Left figure illustrates reaction zone in the transverse plane. Right
figure illustrates reaction plane of the collision.

The method of analyzing flow is summarize in Ref. [63]. The azimuthal
distribution of the associate particles with respect to reaction plane can be
expanded into a Fourier series :
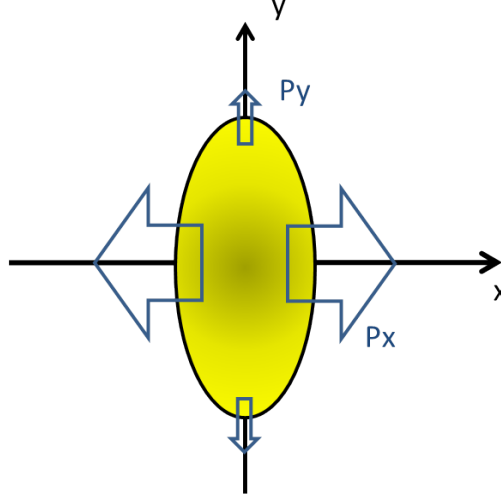
Figure 2.13: Illustration of pressure gradient originated from spatial asymmetry of reaction zone.

$$\frac{dN}{d\phi} = \frac{N}{2\pi}[1 + 2v_1\cos(\phi) + 2v_2\cos(2\phi) + \cdots],$$

$$v_n = \frac{\int d\phi \cos(n\phi)\frac{dN}{d\phi}}{\int d\phi \frac{dN}{d\phi}} = \langle\cos(n\phi)\rangle,$$

where ϕ is the azimuthal angle of momentum and v_n are the Fourier coefficient of n-th harmonics. Because of the symmetry around the y-axis in Figure 2.12, the sine terms vanish in this expansion.

At RHIC, STAR discovered large v_2 of inclusive charged hadrons from the first RHIC run [64]. A lot of observables, particle dependence of v_2, v_2 with different collision system, and $v_1, v_3, \cdots$ has been also measured after that. At low p_T, below around 2 GeV/c , the measurements of v_2 is well fit by hydrodynamical calculations which assume equilibrium established early in the collision ($\sim 0.6 - 1$ fm/c) and small viscosity over entropy density (for example, $\eta/s \sim 0.16$ from Ref. [6]). It is often termed a near-perfect fluid [18, 23–25].
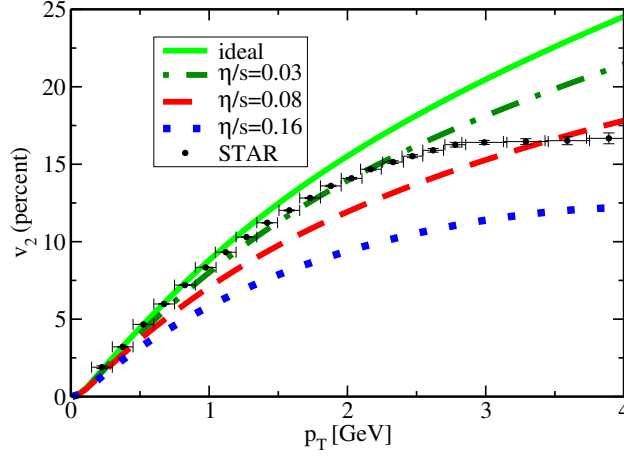
Figure 2.14: STAR measurement of v_2 with hydrodynamical predictions for minimum bias Au+Au at $\sqrt{s_{NN}} = 200$ GeV from [6]

2.3.3 Temperature of the created matter

"Direct photons" stands for the photons which emerge directly from a parton collision. In this subsection, the direct photon measurements are reviewed.

They do not suffer medium effect and carry information about the circumstances of their production [65]. The direct photon is called electromagnetic probe of QGP, as they interact only weakly ($\alpha = 1/137 \ll \alpha_s$) and their mean free path is larger than the typical system size (~ 10 fm). Thermal radiation from the QGP phase is predicted to be the dominant source of direct photons with $1 < p_T < 3$ GeV/c in Au+Au collisions at RHIC [66]. The measurement of direct photons at low p_T will allow the determination of the initial temperature of the matter.

As shown in Figure 2.15, PHENIX observed the enhancement of direct photon yield in Au+Au collision compared with $p+p$ collision in the low p_T (< 3GeV/c) region [20]. The results were compared with several hydrodynamical models of thermal radiation from QGP at RHIC energies. The models assuming the formation of QGP with initial temperature ranging $T_{init} \sim$ 300 – 600 MeV at times $\tau \sim 0.6$–0.15 fm/c are in qualitative agreement with the data [20, 67–70]. It it well above T_c predicted by lattice QCD.

The main background photon source is hadron decay, such as $\pi^0 \to \gamma\gamma$. Their contribution to the photon spectrum is large and subtraction of the decay background from inclusive photon spectrum was a very challenging task. In the data analysis of PHENIX results in Figure 2.15, "internal conversion" method which measure the virtual photons , instead of real photon is used to
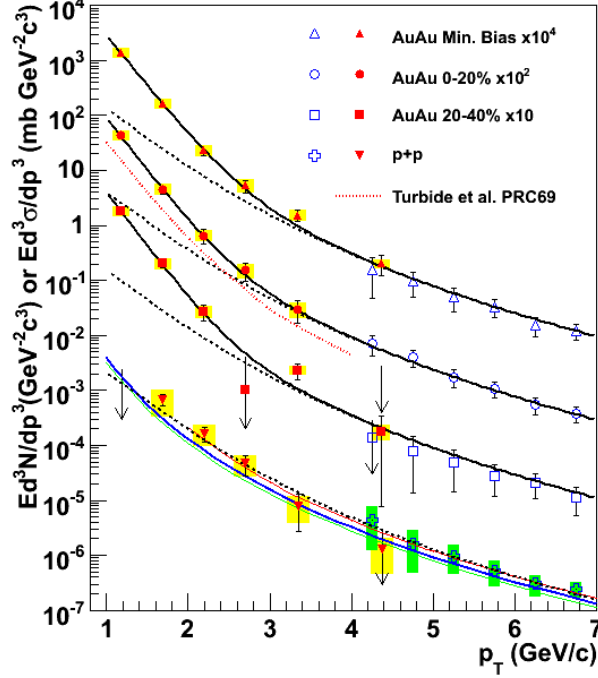
Figure 2.15: Invariant cross section $(p+p)$ and invariant yield (Au+Au) of
direct photons as a function of p_T from [20]. The filled points are from virtual
photon measurements and open points are from real photon measurements.
The three curves on the $p+p$ data represents NLO pQCD calculations, and
the dashed curves show a modified power-law fit to the $p+p$ data, scaled by
T_{AA}. The dashed (black) curves are exponential plus the T_{AA} scaled $p+p$
fit. The dotted (red) curve near the $0-20$ % centrality data is a theory
calculation [66].

separate direct photons from decay background in the low p_T region (filled
points). In general, any source of high energy photons can also emit virtual
photons, which convert to low mass e^+e^- pairs. For example, gluon Compton
scattering $(q+g \rightarrow q+\gamma)$ has an associated process that produces low mass
e^+e^- pairs through internal conversion $(q+g \rightarrow q+\gamma^* \rightarrow q+e^+e^-)$.

The mass distribution of the e^+e^- from pseudo scalar meson decay $(\pi^0, \eta \rightarrow \gamma\gamma)$ follows the Knoll-Wada formula [71].

$$\frac{1}{N_\gamma}\frac{dN}{dM_{ee}} = \frac{2\alpha}{3\pi}\sqrt{1-\frac{4m_e^2}{M_{ee}^2}}(1+\frac{2m_e^2}{M_{ee}^2})\frac{1}{M_{ee}}(1-\frac{M_{ee}^2}{M^2})^3|F(M_{ee}^2)|^2, \qquad (2.3)$$

Here M_{ee} is the mass of the electron pair; m_e is the mass of electron; M is

22

the mass of the parent meson; and $F(M_{ee}^2)$ is a hadronic form factor. The
formula above is normalized as decay rate per photon, and therefore it differs
from the total Dalitz decay rate by a factor of 2 for π^0, η since these mesons
decay into two photons. In the hadron decay, M_{ee} does not exceed parent
hadron mass M, so the part $(1 - \frac{M_{ee}^2}{M^2})^3$ in the above formula becomes 0 if
$(M_{ee} \to M)$.

On the other hand, there is no parent hadron for direct photon, there is no
phase space limitation above in M_{ee} from direct photon. Then, if $e^+ e^-$ pair
yield with large M_{ee} is measured as shown in Figure 2.16, the contribution
from hadron decay is strongly suppressed. Since 80% of the hadronic photons
are from π^0 decays, the signal to background (S/B) ratio for the direct photon
signal improves by a factor of five for $M_{ee} > M_{\pi^0} = 135$ MeV/c^2 in PHENIX
measurement [20].
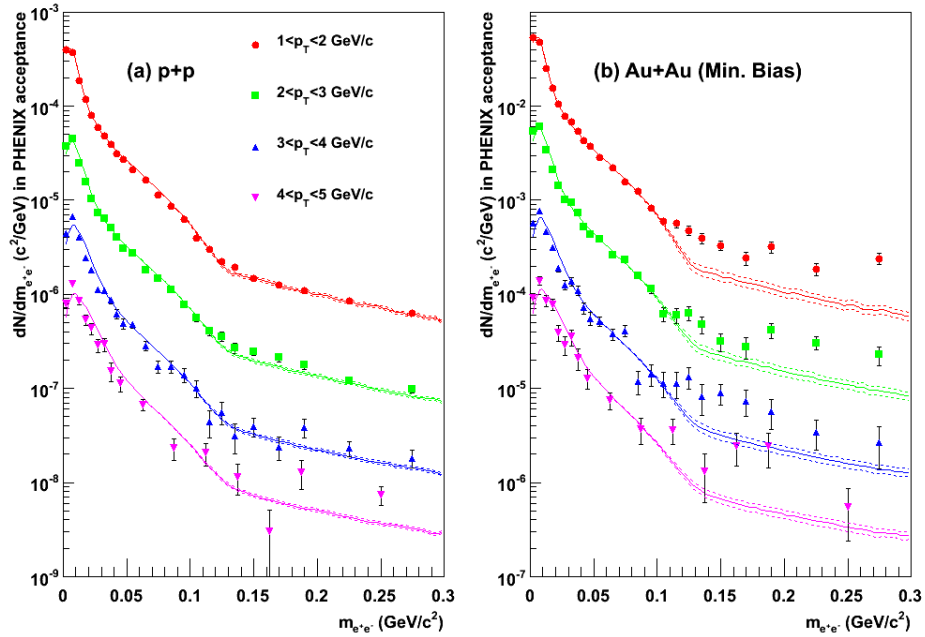
Figure 2.16: Electron pair mass distribution for $p+p$ and Au+Au (Minimum
Bias) taken from [20] The p_T ranges are shown in the legend. The solid curves
represent an estimate of hadronic sources; the dashed curves represent the
uncertainty in the estimate.

Chapter 3

Heavy quark as a probe of the QGP
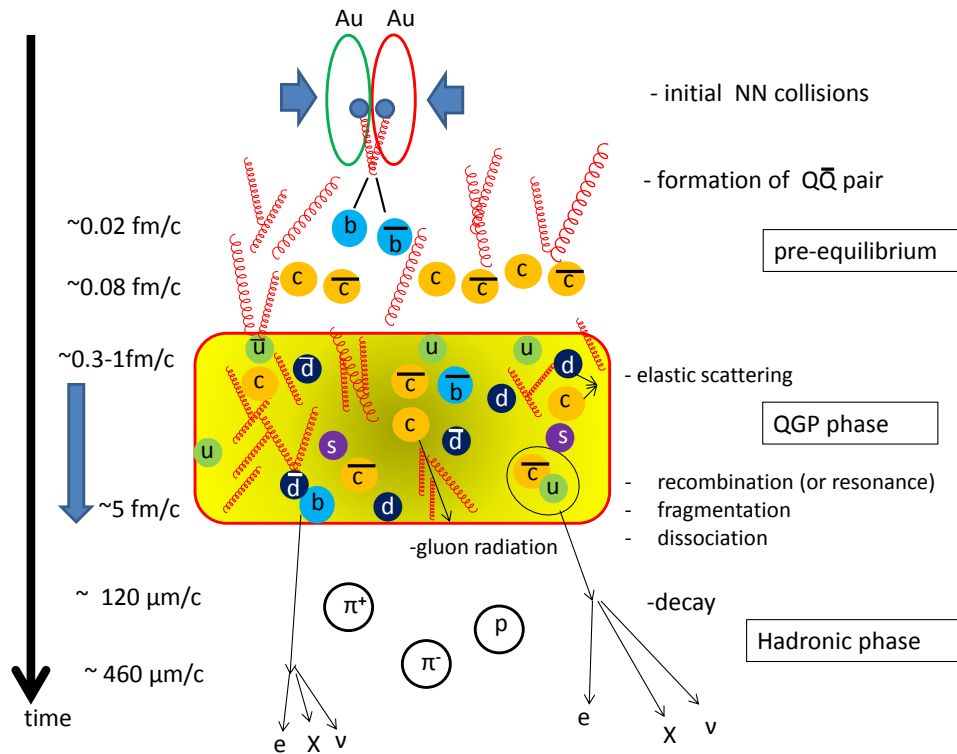
Figure 3.1: Schematic view of time evolution of heavy quarks.

As discussed in the previous chapter, it is well established that the QGP is created in RHIC and the LHC above T_c. Heavy quarks (charm or bottom)

is the suitable probe of the QGP created in high energy heavy ion collisions.

Heavy quarks (Q), including charm (c) and bottom (b) quarks, may exist either as bare quarks inside the QGP, or as bound states of $Q\bar{Q}$ when the medium temperature is still above T_c but not too high [72]. The former state is called as "open" heavy quark and the latter as heavy quarkonium (charmonium or bottomonuim). Bound states of heavy and light quarks ($Q\bar{q}, \bar{Q}q, Qqq...$) such as D, B, Λ_c are also named "open" heavy flavor hadrons.

In this dissertation, the dynamics of open heavy flavor in heavy-ion collisions is concentrated. While, study of heavy quarkonium is also important to investigate property of the QGP, it is out of scope of this dissertation.

The most important property of heavy quarks is their large masses ($m_c \approx$ 1.3 GeV, $m_b \approx 4.7$ GeV [3]) which are much larger than $\Lambda_{QCD} \approx 200$ MeV and the QGP temperature $T \approx 300 - 600$ MeV at RHIC. The heavy quarks ($Q = c, b$) are mainly produced via hard scatterings at the initial nucleon-nucleon collisions, because the large momentum transfer is needed to produce heavy quarks [26]. The production of charm (bottom) quark pairs takes place at timescale $1/(2m_Q) \sim$ 0.08 (0.02) fm/c.

After the heavy quark production, it is expected that the total number of heavy quarks stays constant because $m_c, m_b \gg T_c$ and they are not destroyed by the strong interaction. This is experimentally confirmed within uncertainties [11, 73, 74]. Thus, heavy quarks carry information about the entire time-evolution and transport properties of the QGP or the pre-equilibrium phase before the formation of the QGP as illustrated in Figure 3.1.

On the other hand, light quarks can be generated during the evolution of the medium and even from the mixed phase by low momentum gluon fusion. Light hadron measurements are less sensitive to the energy loss mechanism and transport properties of the early stage of the QGP phase.

3.1   Heavy flavor hadron production

Heavy flavor hadron production in nucleon-nucleon collisions is described by pQCD calculations. For heavy flavor hadrons, pQCD approach is warranted for all momenta since their large quark mass introduces large Q^2 even at zero momentum. This is specific contrast to gluon and light quark jets which can be treated by pQCD only at high p_T.

The experimental results and theoretical calculations of their cross section are useful as a base line of heavy quark energy loss in Heavy ion collisions (the denominator of R_{AA}). Heavy flavor hadron production ($D, B \cdots$) in nucleon-nucleon collisions is described by the QCD factorization approach. This calculation is performed by a convolution of three terms: the parton

distribution function of nucleon 1 and nucleon 2 ($f_1^{N_1}$, $f_2^{N_2}$, respectively), the hard parton scattering cross section $d\hat{\sigma}^{f_1 f_2 \to fX}$, and the fragmentation function (D_f^h).

$$
\begin{aligned}
d\sigma^{N_1 N_2 \to hX} \quad &= \sum_{f_1, f_2, f} \int dx_1 dx_2 dz f_1^{N_1}(x_1, \mu_{FI}^2) f_2^{N_2}(x_2, \mu_{FI}^2) \times \\
&\quad d\hat{\sigma}^{f_1 f_2 \to fX}(x_1 p_1, x_2 p_2, p_h/z, \mu_{FI}, \mu_{FF}, \mu_R) \times D_f^h(z, \mu_{FF}^2)
\end{aligned}
\tag{3.1}
$$

Here,

- The fragmentation function $D_f^h(z, \mu_{FF}^2)$ describes the probability that the outgoing parton fragments into the observed hadron h with fractional momentum $z = p_h/p_f$, μ_{FF} is the factorization scale of fragmentation function.

- $d\hat{\sigma}^{f_1 f_2 \to fX}(x_1 p_1, x_2 p_2, p_h/z, \mu_{FI}, \mu_{FF}, \mu_R)$ is perturbative partonic cross section computable up to a given order in α_s. μ_R is the renormalization scale, and μ_{FI} is the factorization scales of parton distribution function.

The production cross section of charm hadrons at RHIC($\sqrt{s_{NN}} = 200$ GeV, $p+p$) [75, 76], at Tevatron ($\sqrt{s_{NN}} = 1.96$ TeV, $p+\bar{p}$) [77–79] and at the LHC ($\sqrt{s_{NN}} = 2.76$ TeV and 7 TeV, $p+p$) [80–82] are found to be larger than such calculations (NLO MNR calculation [83] and Fixed Order plus Next-to-Leading Logarithms (FONLL) calculation [8, 84]), which is still compatible with the theoretical uncertainties as shown in Figure 3.2 [82].

The production cross section of bottom hadrons at RHIC($\sqrt{s_{NN}} = 200$ GeV, $p+p$) [13, 14], at Tevatron ($\sqrt{s_{NN}} = 1.96$ TeV, $p+\bar{p}$) [85–87], UA1 ($\sqrt{s_{NN}} = 630$ GeV, $p+\bar{p}$) [88] and at the LHC ($\sqrt{s_{NN}} = 2.76$ TeV and 7 TeV, $p+p$) [89–91] are well described by FONLL [84].

Most dominant charm and bottom production process is gluon fusion $g + g \to Q + \bar{Q}$ ($Q = c, b$) and flavor excitation $g + g \to Q + \bar{Q} + g$ [92]. This is a result of the large fraction of gluons in parton distribution function as shown in Figure 2.5.

In RHIC, measurement in $p+p$ collision at $\sqrt{s_{NN}} = 200$ GeV, the total charm-anticharm quark cross section is 551 ± 57 (stat.) ± 195 (sys.) μb [11]. Almost 99% of produced charm quarks and bottoms quarks are known to form open heavy flavor hadrons. The total cross section of J/ψ is 4.0 ± 0.6(stat.)± 0.6(syst.)± 0.4(abs.) μb [93]. The total bottom-antibottom quark cross section is $3.2^{+1.2+1.4}_{-1.1-1.3}$ μb [13].

In Au+Au collisions, medium effects, such as energy loss of charm or bottom in the QGP, can only influence the momentum distribution of charm
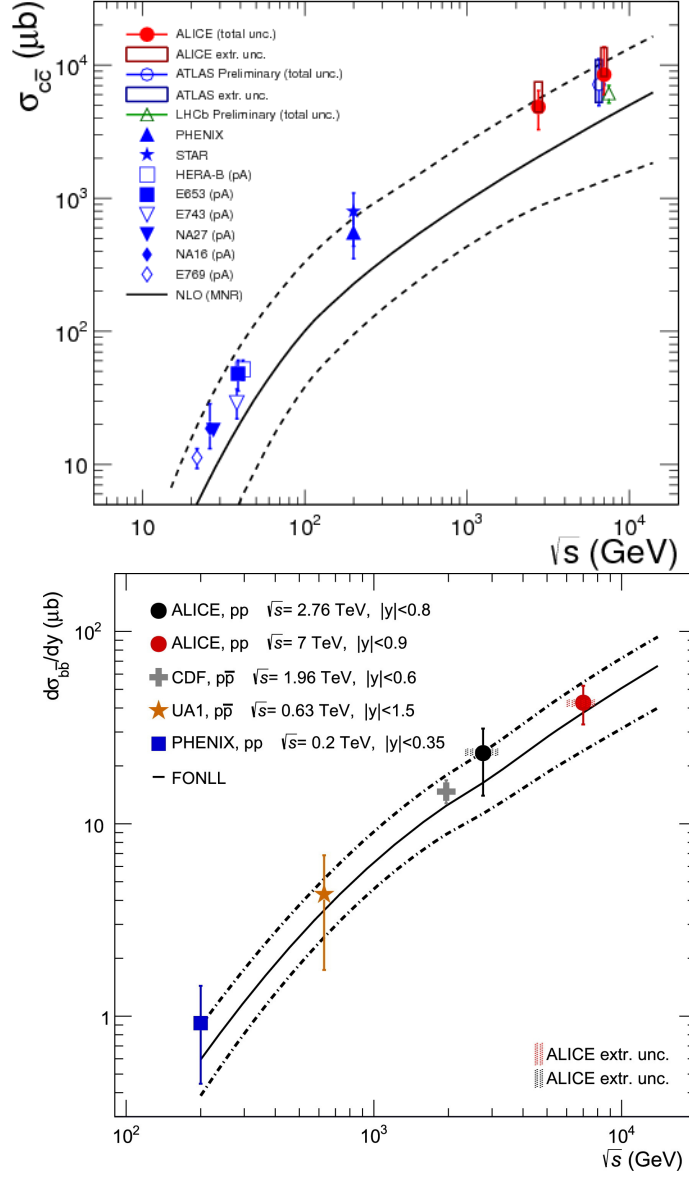
Figure 3.2: Heavy quark production cross section in $p+p$ or $\bar{p}+p$ collisions as a function of center of mass energy in $p+p$ or $\bar{p}+p$ collisions. (Top) charm production cross section from [82]. (Bottom) Inclusive bottom production cross section per rapidity unit measured at mid-rapidity along with the comparison to FONLL calculations from [91].

or bottom, and the number of heavy quarks produced by binary nucleon-nucleon collision are conserved [11, 73, 74]. Namely,

$$\int \int R_{AA}(Q) dp_T dy = 1$$

The thermal production of heavy quarks, are believed to be very small at RHIC energy, because their mass ($m_c \approx 1.3$ GeV, $m_b \approx 4.7$ GeV [3]) is much larger than $\Lambda_{\mathrm{QCD}} \approx 200$ MeV and the QGP temperature $T \approx 300 - 600$ MeV.

Figure 3.3 shows the centrality dependence of the yield of electron from heavy flavor as well as the yield in $p+p$ [74]. Those results show that the centrality dependence of charm quark production is consistent with N_{coll} scaling. The N_{coll} dependence of the yield was fit to $N_{\mathrm{coll}}^{\alpha}$ and found $\alpha = 0.938 \pm 0.075(\text{stat.}) \pm 0.018(\text{sys.})$, showing that the total yield of charm-decay electrons is consistent with binary scaling.
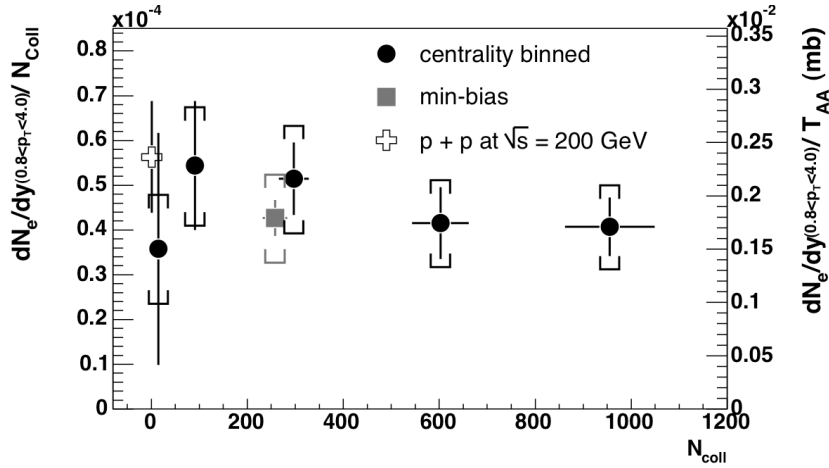
Figure 3.3: Electron from heavy flavor yield ($0.8 < p_T < 4.0$ GeV/c) measured in Au+Au collision at $\sqrt{s_{NN}} = 200$ GeV scaled by the number of binary collisions (N_{coll}) from [74]. The yield in $p+p$ collisions is also shown.

3.2 Decay of charm and bottom hadrons

Open heavy flavor hadrons can be measured by the direct reconstruction (invariant mass reconstruction) or part of their decay products. Some important decay channels of the relevant hadrons for identify open heavy flavor hadrons in measurements are summarized in Table 3.1 and 3.2.

As will be discussed in the section 3.3, PHENIX has been measured electrons from semi-leptonic decay of charm and bottom hadrons (heavy flavor electron). The advantage of semi-leptonic decay is relatively large branching ratio of heavy flavor hadrons ($\sim 10\%$). The contribution from electrons from light neutral mesons and photon conversion are not negligible, but they can be subtracted by cocktail method and isolation cuts (they will be introduced in chapter 5.

Table 3.1: Decay modes, Branching ratios (B.R.), decay momentum* (p) and life times for main charm hadrons from PDG [3]. Charge conjugates are abbreviated.

Particle	Decay mode	B.R. (%)	p (MeV/c)	$c\tau$ (μm)
D^+	e^+ anything	16.07 ± 0.30		311.8
	μ^+ anything	17.6 ± 3.2		
	$e^+ \overline{K}^0 \nu_e$	8.83 ± 0.22	869	
	$e^+ \overline{K}^{*0} \nu_e$	3.68 ± 0.10	722	
	$K^- \pi^+ \pi^+$	9.13 ± 0.19	846	
D^0	e^+ anything	6.49 ± 0.11		122.9
	μ^+ anything	6.7 ± 0.6		
	$e^+ K^- \nu_e$	3.55 ± 0.04	867	
	$e^+ K^{*-} \nu_e$	2.16 ± 0.16	719	
	$K^- \pi^+$	3.88 ± 0.05	861	
D_s^+	e^+ anything	6.5 ± 0.4		149.9
	$e^+ \eta \nu_e$	2.67 ± 0.29	908	
	$e^+ \phi \nu_e$	2.49 ± 0.14	720	
	$\phi \pi^+$	4.5 ± 0.4	712	
D^{*+}	$D^0 \pi^+$	67.5 ± 0.5	39	$(2.1 \pm 0.5) \times 10^{-6}$
Λ_c^+	e^+ anything	4.6 ± 1.7		59.9
	$e^+ \Lambda \nu_e$	2.1 ± 0.6	871	
	$p K^- \pi^+$	5.0 ± 1.3	823	

∗ For a 2 body decay, p is the momentum of each decay product in the rest frame of the decaying particle. For a 3 or more body decay, p is the largest momentum any of the products can have in this rest frame.

Table 3.2: The same as table 3.1 but for bottom hadrons from PDG [3]. Charge conjugates are abbreviated.

Particle	Decay mode	B.R. (%)	p (MeV/c)	$c\tau$ (μm)
B^+	$e^+\nu_e X$	10.8 ± 0.4		492.0
	$l^+\overline{D}^0\nu_l$	2.26 ± 0.11	2310	
	$l^+\overline{D}^{*0}\nu_l$	5.70 ± 0.19	2258	
	$J/\psi K^+$	0.1016 ± 0.0033	1683	
B^0	$e^+\nu_e X$	10.1 ± 0.4		455.4
	$l^+ D^-\nu_l$	2.18 ± 0.12	2309	
	$l^+ D^{*-}\nu_l$	4.95 ± 0.11	2257	
	$J/\psi K_s^0$	0.0437 ± 0.0016	1683	
B_s^0	$l^+\nu X$	9.5 ± 2.7		449
	$J/\psi\phi$	$0.109~^{+0.28}_{-0.23}$	1588	
Λ_b^0	$l^-\overline{\nu}_l\Lambda_c^+$ anythinag	9.8 ± 2.3		427
	$l^-\overline{\nu}_l\Lambda_c^+$	$6.5~^{+3.2}_{-2.5}$	2345	
	$l^-\overline{\nu}_l\Lambda_c^+\pi^+\pi^-$	5.6 ± 3.1	2335	

$*$ For a 2 body decay, p is the momentum of each decay product in the rest frame of the decaying particle. For a 3 or more body decay, p is the largest momentum any of the products can have in this rest frame.

3.3 Heavy flavor hadron measurement in RHIC and the LHC

3.3.1 Overview of heavy flavor measurement

Measurement of heavy flavor hadrons is much more difficult than light hadrons because their production cross section is small. Various methods of heavy flavor detections are so far applied in RHIC and the LHC as follows,

- Single electron (or muon) measurement (from admixture of charm and bottom).

- electron-hadron correlation to separate charm and bottom (only available in $p+p$).

- Invariant mass measurements for charm hadron and bottom hadron. (Direct reconstruction method)

- Non-prompt J/ψ ($B \rightarrow J/\psi X$) measurement.

- Displaced single electron (or muon) track to separate charm and bottom contribution.

While heavy flavor measurements in heavy ion collisions are useful to investigate the property of the QGP, reference measurements in $p+p$ collisions are also important from two points of view. First, these data provide an experimental reference for corresponding measurements in heavy ion collisions. Such a reference is necessary for the denominator of R_{AA}. Second, these data provide an important testing ground for pQCD calculations which, due to the large masses of the charm and bottom quarks, should be able to predict open heavy flavor observables even at low p_T [11].

In following subsections, the previous single electron measurements at PHENIX are emphasized as it is the first observation of suppression of heavy quarks. The other recent measurements in RHIC and the LHC are also reviewed after that. In the end of this section, the new method to separate charm and bottom contribution Au+Au collisions, which is the main goal of this dissertation, is briefly introduced.

3.3.2 Single electron measurements at PHENIX

method

Both charm and bottom mesons (D, B) have relatively large branching ratios ($\sim 10\%$) to single electrons or single muons. Thus the single elec-

tron measurement has an advantage to other methods in terms of statistic. A disadvantage is that kinematics of parent heavy flavor hadron is smeared through the decay, thus it is rather insensitive to the heavy quark momentum. The other disadvantage is that it cannot distinguish between the contributions from the charm and bottom hadrons without additional information.

The inclusive single electron spectra consist primarily of four components:

1. electrons from open heavy flavor decays,

2. photonic background from Dalitz decays of light neutral mesons (for example, $\pi^0 \rightarrow e^+e^-\gamma$ and photon conversions in the material,

3. nonphotonic background from $K \rightarrow e\pi\nu$ (K_{e3}) and dielectron decays of light vector mesons, and

4. heavy quarkonia ($J/\psi, \Upsilon$) and Drell-Yan background processes.

The dominant source of electron is charm hadrons in total as the bottom production cross section is small. However due to the large Q-value for bottom decays, electrons from bottom hadrons can have an excess at high p_T region. According to the FONLL calculation [8], at about $p_T = 4$ GeV/c the contributions from charm and bottom decays are in the same level, and towards higher p_T, bottom decays become the dominant source of electrons.

Of the three background sources, the "photonic" background is the largest. To extract the heavy flavor electron signal, the various background contributions listed above have to be subtracted from the inclusive electron spectra. So-called "cocktail subtraction" method ($p_T > 1.6$ GeV/c) and "converter subtraction" method ($0.3 < p_T < 1.6$ GeV/c) are used for this measurement.

A cocktail of electron spectra from background sources is estimated by using a Monte Carlo simulation of hadron decays and then subtracted from the inclusive electron spectra. The PHENIX measurements of the relevant electron sources are precise enough to constrain the background within a systematic uncertainty better than 15% for all p_T [11].

The yields of photonic and nonphotonic electrons are obtained by measuring the difference between inclusive electron yields with and without a photon converter of precisely known thickness: a brass sheet of 1.680% radiation length (X_0).

results and interpretations in Au+Au and $p+p$ collisions

After subtraction of various background, PHENIX first observed the suppression of electrons from heavy flavor in Au+Au collision from year 2004

data (RUN4), comparing with $p+p$ collision from year 2005 data (RUN5) [11]. Figure 3.4 shows the PHENIX measurement of R_{AA} (and v_2) of electrons from open heavy flavor in the 2004/2005 data in 0-10% central and minimum bias collisions, and corresponding π^0 data [11, 94].
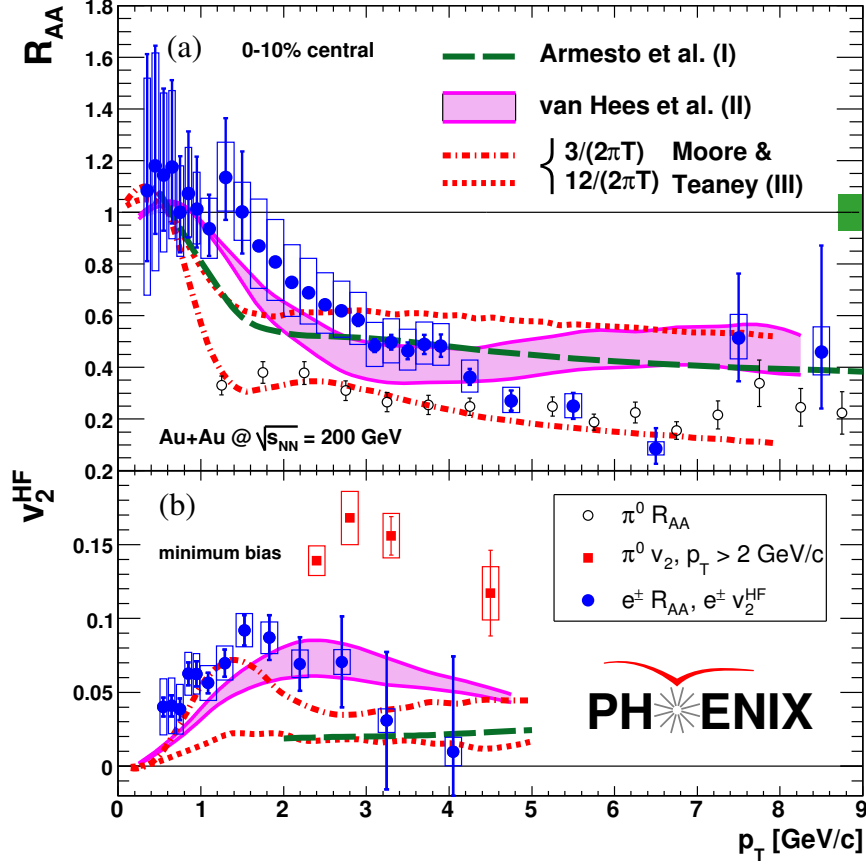
Figure 3.4: PHENIX measurement of R_{AA} and v_2 of electron from heavy flavor from 2004/2005 data [11]. Top panel shows R_{AA} of heavy flavor electrons in 0-10% central collisions compared with π^0 data. Bottom panel shows the elliptic flow parameter v_2 of heavy flavor electrons in minimum bias collisions compared with π^0's v_2.

While at low p_T the suppression is smaller than that of π^0, R_{AA} of electrons from open heavy flavor approaches the π^0 value for $p_T \geq 4$ GeV/c . In this p_T region, the contribution of electrons from bottom hadrons was naively expected to be large due to their large Q-value. In the 2004 Au+Au collision data, PHENIX did not have capability to separate charm and bottom.

Although the charm and bottom contributions are not separated in this measurement, this suppression of heavy flavor electrons was unexpected be-

cause the radiative loss of heavy quarks were thought to be small due to the dead cone effect, (see subsection 3.4.1), and collisional energy loss was believed to be negligible at high p_T.

Those data indicate strong coupling of heavy quarks to the medium. Figure 3.4 shows a quantitative comparison of model calculations. Curve I [95] shows radiative energy loss calculation with the BDMPS formalism [96]. Curves II [97] and III [98] show a calculation which considers elastic scattering mediated by the excitation of D or B meson like resonant states in the medium. In those calculation, heavy quark is put into a thermal medium and Langevin-based transport model are applied for the heavy quark motion in the QGP. Ref. [97] shows that the bottom contributions can dominate above $p_T \sim 3.5$ GeV/c and it reduces both suppression and elliptic flow, which was not confirmed in this PHENIX measurement.

Initial state effect

The nuclear modification factor R_{AA} is also expected to contain effects come from normal nuclear matter. The presence of the normal nuclear matter can change the kinematic distributions of the observables compared to $p+p$ without the QGP ever being formed. This effect is generally referred to as "initial state effect".

Figure 3.5 shows the nuclear modification factors for heavy flavor electron at midrapidity in central d+Au, Cu+Cu, and Au+Au collisions at $\sqrt{s_{NN}}$ = 200 GeV [99]. The d+Au data show the enhancement relative to $p+p$ collisions between $1 < p_T < 5$ GeV/c .

Such an enhancement is termed "Cronin effect" [54] as explained in subsection 2.3.1 and expected to moderate the large suppression of heavy flavor electron in Au+Au collisions at $\sqrt{s_{NN}}$ = 200 GeV, but this is not fully understood.

In the d+Au collision, it is expected that there is no QGP effect and thus it is good control experiment to evaluate cold nuclear matter effect. This assumption is, however, challenged by phenomena recently found in $p+Pb$ (LHC) and d+Au (RHIC) collisions (for example, "ridge"), which may come from hydrodynamics or gluon saturation [100–105] .
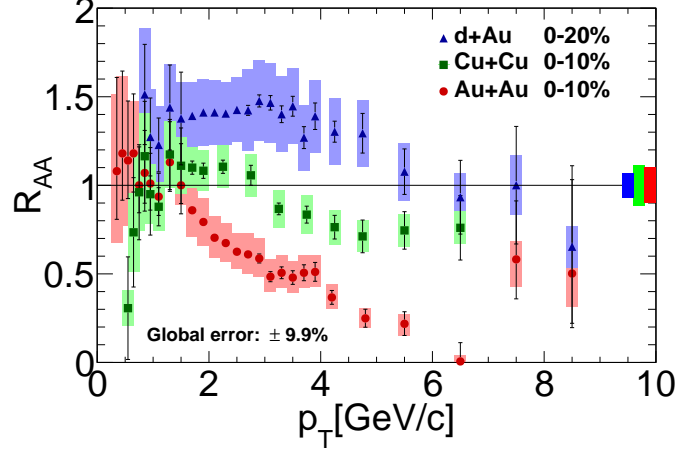
Figure 3.5: The nuclear modification factors for heavy flavor electron at midrapidity ($\eta < 0.35$) in central d+Au, Cu+Cu, and Au+Au collisions at $\sqrt{s_{NN}} = 200$ GeV with PHENIX [99]. The boxes around 1 are global uncertainties, which include the N_{coll} scaling error. The global error given in the legend is from the p+p yield.

3.3.3 Electron-hadron correlation

In p+p collision, there is an alternative approach to access bottom hadrons. Both PHENIX and STAR developed bottom and charm hadron separation techniques based on electron-hadron correlation measurement, utilizing the difference of decay property between charm and bottom hadrons. Due to the fact that the combinatorial background in electron-hadron correlation measurements increases dramatically with particle multiplicity, this method can not be used in heavy ion collisions.

In the PHENIX, the separation of the relative contributions from charm and bottom decays was carried out based on the decay channel $D/\bar{D} \to e^{\pm} + K^{\mp} X$ [13]. A correlation of the invariant mass distribution is observed for unlike charge-sign electron-hadron pairs ($e^{\pm} K^{\mp}$) below the D-meson mass, because of the charge correlation in D-meson decays.

In the STAR, the relative contribution from B decays to heavy flavor electron yields was measured using the azimuthal correlations between heavy flavor electrons and charged hadrons, and between heavy flavor electrons and D^0 mesons [14].

Figure 3.6 shows the distribution of the azimuthal angle between heavy flavor electrons and hadrons for two electron p_T ranges. The distribution is normalized to the number of heavy flavor electrons. The shapes of these

distributions are different because the decay kinematics of the charm and bottom hadron decays are different (some of them are shown in table 3.1 and table 3.2). Figure 3.6 also shows the template distributions made by PYTHIA simulation [106] reflecting the expected shapes of the electron-hadron azimuthal distributions from charm hadrons and bottom hadrons.

The contribution of bottom decays relative to the sum of charm and bottom decays was obtained from a fit to the azimuthal angle distributions using a linear combination of the charm and bottom templates with the relative normalization as a fit parameter. In this way, charm contribution and bottom contribution can be separated statistically.

STAR also performed an independent measurement using electron - D^0 correlation, where D^0 is identified by the invariant mass reconstruction of K and π. In this measurement, the azimuthal angle distribution in the away-side ($\phi \sim \pi$) are dominated by charm hadrons due to the back-to-back correlation of $c\bar{c}$ jets. Again, template distributions obtained by PYTHIA simulation were used to statistically separate charm and bottom. MC@NLO [107] simulation, which is a Monte Carlo event generator with Next-to-Leading-Order calculations of rates for QCD processes, is used for the fitting in this analysis the average value with the result from the PYTHIA simulation for the final value.

The observed away-side correlation signal in the electron-D^0 azimuthal angle distribution was attributed to prompt charm hadron pair production ($\sim 75\%$) and bottom hadron decays ($\sim 25\%$), while the near side correlation signal was mainly due to bottom hadron decays ($B \to De\mu$).

The contributions of bottom decays to the total electron spectrum from heavy-flavor hadron decays obtained with these two methods are compared in the right panel of Figure 3.6 as functions of the electron p_T. The STAR apparatus has larger acceptance compared to PHENIX, which is a clear advantage for such multi-particle measurements.

3.3.4 Direct reconstruction measurement

This method uses hadronic decays of heavy flavor hadron by detecting all decay products to observe invariant mass peaks. This measurement requires wide acceptance of detectors and good capability of particle identification as well as high statistic data. STAR has measured D^0 mesons via a hadronic decay channel $D^0 \to K^- + \pi^+$ [15] in Au+Au collisions at $\sqrt{s_{NN}} = 200$ GeV. STAR also measured D^0 and D^{*+} via $D^0 \to K^- + \pi^+$ and $D^{*+} \to D^0\pi^+ \to K^-\pi^+\pi^+$ [108] in $p+p$. By comparing them, they reported the nuclear modification for D^0 meson (i.e. $R_{AA} < 1$) in the central collisions while no suppression was seen in peripheral collisions (Figure 3.7).
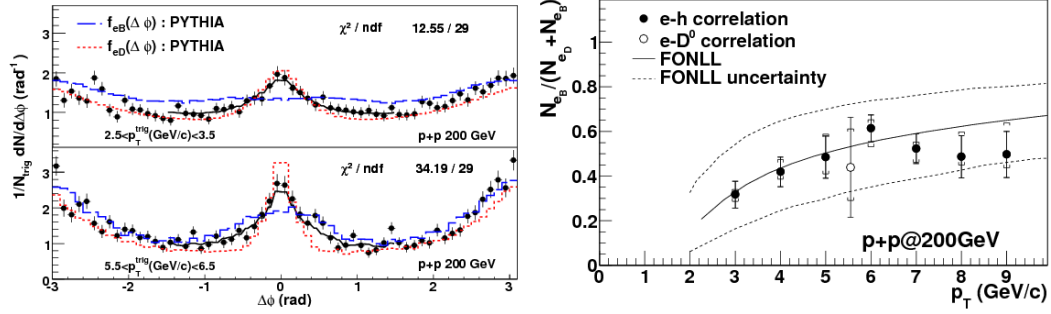
Figure 3.6: (Left) The azimuthal angle between heavy flavor electrons and hadrons measured with STAR in $p+p$ collisions is compared to charm and bottom decay templates obtained with PYTHIA simulations for two electron p_T ranges. (Right) Relative contributions of bottom decays to the total yield of electrons from heavy flavor hadron decays as functions of the electron p_T are compared to predictions from FONLL pQCD calculations [8]. Both figures are from [14].

In STAR, Time Projection Chamber (TPC) [109] is the main tracking detector, covering the full azimuthal angle at pseudorapidity $\eta \leq 1$. It measures the charged-particle momenta and provides particle-identification (PID) capability via the ionization energy loss (dE/dx) in the TPC gas, allowing separation between charged kaons and pions up to momentum $p \sim 0.6$ GeV/c . In addition to that, Time Of Flight detector (TOF) [110] gives good pions and kaons separation up to $p_T = 1.6$ GeV/c .

In Pb+Pb and $p+p$ collision at the LHC at $\sqrt{s_{NN}} = 2.76$ TeV, ALICE reports similar modification via $D^+ \rightarrow K^-\pi^+\pi^+$, $D^0 \rightarrow K^-\pi^+$ and $D^{*+} \rightarrow D^0\pi^+$ (and their anti-particle) [111, 112].

This direct reconstruction method also could be applied for B meson. However, since the mean multiplicity of the final state in B meson decay is larger than D meson decay, it is rather difficult compared to D meson reconstruction. So far, Large Hadron Collider beauty experiment (LHCb) measured $B^+ \rightarrow J/\psi K^+$ with $J/\psi \rightarrow \mu^+\mu^-$ in $p+p$ at $\sqrt{s_{NN}} = 7$ TeV [113]. The CMS has the preliminary result of measurement via $B^+ \rightarrow J/\psi K^+$, $B^0 \rightarrow J/\psi K^*(892)$ and $B_s \rightarrow J/\psi\phi$, with $J/\psi \rightarrow \mu^+\mu^-$ in $p+p$ and $p+Pb$ collisions at $\sqrt{s_{NN}} = 5.02$ TeV. [114].

3.3.5 Non-prompt J/ψ measurement

An alternative approach for bottom hadron production is the measurement of J/ψ emitted from displaced decay of bottom hadron vertices, uti-
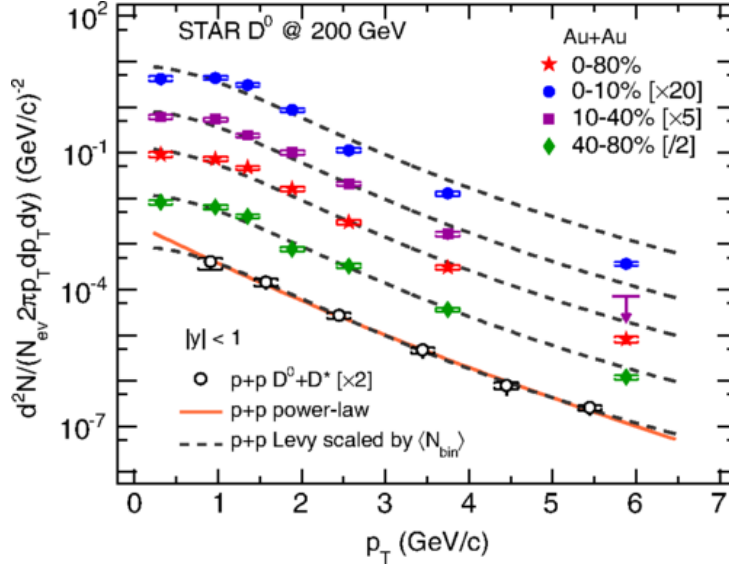
Figure 3.7: Centrality dependence of the D^0 p_T differential invariant yield with STAR in Au+Au collisions (solid symbols) [15]. The curves are number-of-binary-collision-scaled Levy functions from fitting to the $p+p$ result (open circles) [108]. The arrow denotes the upper limit with a 90% confidence level of the last data point for 10%-40% collisions. The systematic uncertainties are shown as square brackets.

lizing relatively large life time (see table 3.2). Those J/ψ s are called "non-prompt J/ψ". This measurement requires high resolution vertex detector to precisely separate primary and secondary vertices.

The Compact Muon Solenoid (experiment at the LHC) (CMS) measured non-prompt J/ψ via the reconstruction of secondary $\mu^+\mu^-$ vertices in Pb+Pb and in $p+p$ collision at $\sqrt{s_{NN}} = 2.76$ TeV and observed $R_{AA} \sim 0.4$ [115].This is the first measurement which disentangled the charm and bottom production in Pb+Pb collision at the LHC. After that, CMS further improved their analysis and reconstructed b-jet [116]. Experimentally, the jet associated with a b hadron is commonly referred to a "b jet", although the b quark is not guaranteed to be the leading parton of the jet. By reconstructing a jet total energy, it is more sensitive to the parton energy loss compared with measurement of fragmented J/ψ. The b-jet R_{AA} is found to be ~ 0.4 in the most central collisions and it is qualitatively consistent with that of inclusive jets above $p_T^{\text{jet}} \sim 100$ GeV/c [117].

3.3.6   Separating charm and bottom

The single electron measurement reviewed in subsection 3.3.2 has an advantage in terms of statistics in the limited acceptance of detectors compared with direct reconstruction method, however the relative charm and bottom contribution are unclear.

Since the large difference of lifetime of charm hadrons and bottom hadrons (see section 3.2) are useful to separate charm and bottom contribution in the single electron measurement, the PHENIX Collaboration proposed displaced track measurement to separate charm and bottom contribution from single electron data and has developed Silicon Vertex Tracker (VTX).

The Silicon Vertex Tracker (VTX) was installed in the RHIC-PHENIX detector in the end of year 2010. The VTX was designed to give precise tracking reconstructions of the distance of closest approach (DCA) to the collision vertex in order to distinguish prompt particles from in-flight decays. In this way, electrons from semi-leptonic decay of heavy flavor hadrons are able to be statistically separated. The detail of this method is described in chapter 5.

3.4   Energy loss of heavy quark in the QGP

In this subsection, the energy loss mechanism and the early theoretical prediction for charm and bottom quarks before the experimental results from the year 2004 PHENIX data [11] are reviewed. After that, the recent theory development motivated by the PHENIX results are also explained.

Before the measurement of single electron from PHENIX [11] (see subsection 3.3.2), the energy loss of fast partons in-medium was expected to be dominated by gluon bremsstrahlung (radiative energy loss) [118]. Radiative loss of heavy quark in-medium was thought to be much smaller than light partons due to the "Dead cone effect" [7].

3.4.1   Dead Cone effect

Gluon bremsstrahlung from a heavy quark is suppressed from that of light partons at angles smaller than the ratio of the quark mass M to its energy E, due to kinematics constraints.

The double differential distribution of gluons of transverse momentum $k_\perp$ and energy ω radiated by a heavy quark $\omega\frac{dP_{rad,HQ}}{d\omega dk_\perp^2}$ is expressed as,

$$\omega\frac{dP_{rad,HQ}}{d\omega dk_\perp^2} = \frac{\alpha_s C_F}{\pi}\frac{k_\perp^2}{(k_\perp^2 + \omega^2\theta_0^2)^2},$$

where

$$\theta_0 \equiv \frac{M}{E} = \frac{1}{\gamma},$$

α_s is the strong coupling constant and C_F is the Casimir factor and for the quark case here $\frac{N_c^2-1}{2N_c} = 4/3$. In the small angle approximation ($k_\perp \sim \omega\theta$), it differs from the bremsstrahlung spectrum from the light partons $\omega\frac{dP_{rad,0}}{d\omega dk_\perp^2}$ by the factor

$$\omega\frac{dP_{rad,HQ}}{d\omega dk_\perp^2} \approx \omega\frac{dP_{rad,0}}{d\omega dk_\perp^2} \cdot (1 + \frac{\theta_0^2}{\theta^2})^{-2}$$

This formula means that gluon radiation at small angles with respect to the quark momentum vector is reduced by $(1 + \frac{\theta_0^2}{\theta^2})^{-2}$. This effect, termed "dead cone effect" [7] is larger for bottom than for charm; Thus, $R_{AA}{}^\pi < R_{AA}{}^c < R_{AA}{}^b$ was expected against the PHENIX single electron measurement [11].
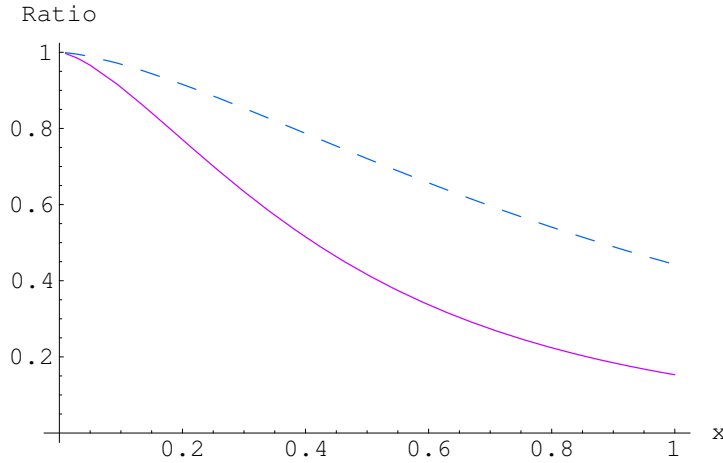
Figure 3.8: The ratio of gluon spectra off charm and light quarks for transverse quark momenta $p_\perp = 10$ GeV (solid line) and $p_\perp = 100$ GeV (dashed) in QGP matter (the path length $L = 5$ fm), $x = \omega/p_\perp$, from Ref. [7].

3.4.2 Recent theoritical development

Along with dead cone effect, which suppress the radiative loss of heavy quarks in the QGP medium, there are a number of theoretical developments. In this subsection, some of them are briefly introduced. Both collisional energy loss and radiative energy loss have been reconsidered.

The propagation of heavy quark in the QGP has been often treated within the framework of Fokker-Planck equation [98, 119–123]. For slowly moving

heavy quarks in the QGP, the dominant interaction is elastic scattering and at high momentum, radiative energy loss (gluon bremsstrahlung) is believed to eventually become the dominant energy loss mechanism. It is currently not known at which p_T this transition occurs [120].

Transport Models

Brownian motion of heavy quarks can be considered for the collisional energy loss. The typical momentum transfer from a thermal medium to a heavy quark is small compared to the heavy quark thermal momentum p_{th}. Non-relativistically, the typical kinetic energy of heavy quarks with temperature T

$$p_{th}^2/2m_Q \simeq 3k_B T/2, \qquad (3.2)$$

where k_B is Boltzman constant. Then,

$$p_{th}^2 \simeq 3m_Q k_B T. \qquad (3.3)$$

This is much larger than the typical momentum transfer from the medium of light partons, $Q^2 \sim (k_B T)^2$. This allows a Brownian Motion approach (Fokker-Plank equation) for heavy quarks as follows,

$$\frac{\partial}{\partial t} f_Q(t, \boldsymbol{p}) = \gamma \frac{\partial}{\partial p_i}[p_i f_Q(t, \boldsymbol{p})] + D \Delta_{\boldsymbol{p}} f_Q(t, \boldsymbol{p}) . \qquad (3.4)$$

Here, f_Q is the phase-space distirbution of a heavy quark and the γ is the drag (or friction) coefficient, which determines the relaxation rate of the average momentum to its equilibrium value: $< \boldsymbol{p} > = \boldsymbol{p_0} \exp{(-\gamma t)}$.

The spatial diffusion constant D, characterising the dynamics of heavy non-relativistic particles (mass M and momentum $\boldsymbol{p}$) traversing the plasma, is connected, via the Einstein relations

$$D = T/(M\eta_D) = 2T^2/\kappa \qquad (3.5)$$

to the momentum diffusion coefficient κ - the average momentum gained by the particle per unit time. The smaller values of D yield a stronger coupling.

Recent several calculations of Ref.[124–127] provide the prediction of charm and bottom fraction as a function of p_T using the Langevin-type approach, but the treatment of coupling between heavy quark and medium are different in their models.

T-matrix approach

Several lattice QCD calculations have found indications that hadronic resonances (or bound state) of heavy quarks survive up to $\sim 2T_C$ or more higher temperature [72, 128, 129]. Refs. [124, 130] assume that heavy-light quark ($Q\bar{q}$ or $\bar{Q}q$) resonance (D or B meson) persist as hadron in the QGP and include this effect in the collisional energy loss. The formation of those resonance state is non-pertavative process. To solve this, a Brueckner-type in-medium T-matrix approach for heavy-light quark scattering in the QGP has been applied in Ref. [124].In this calculation, it is assumed that the effective in-medium potential can be extracted from lattice QCD calculations of the color-singlet free energy and two different calculation are used for this [131, 132]. Both of them are suppressed in high p_T in T-matrix calculations than in pQCD calculation [97].

DGLV theory

Recent calculations of radiative energy loss via gluon emission is described in [133, 134], using the Djordjevic, Gyulassy, Vogt, and Wicks (DGLV) theory, which is extended from GLV reaction-operator method for light-parton radiative energy loss in the QGP [135].

This model assumes an effectively static medium and the medium effect in this approach is characterized by two parameters: the gluon density $\rho(\tau)$ of the scattering centers (or the mean free path λ_g of the radiated gluon) and the Debye screening mass μ_D which is introduced to regulate the infrared behavior of single scattering cross section.

Figure 3.9 shows the c and b quark distributions at midrapidity before fragmentation as well as decay electron ($c \to e$ and $b \to e$) distribution from Ref. [133]. Note in this calculation, only the energy loss by medium-induced gluon radiation is taken into account.

Those results depends on the gluon density $\frac{dN_g}{dy}$, which comes from the assumption: the medium is uniformly and cylindrically expanding, i.e $\rho(\tau) \approx \frac{dN_g}{dy}\tau\pi R^2$ with $R = 6$ fm in central collisions.

In Figure 3.9. the electron decay distributions, $c \to e$ and $b \to e$, are seen to cross each other at $p_T \sim 5.5$ GeV/c when $\frac{dN_g}{dy} = 0$ (no suppression), the crossing point is reduced to $p_T \sim 3$GeV/c for $\frac{dN_g}{dy} = 3500$.
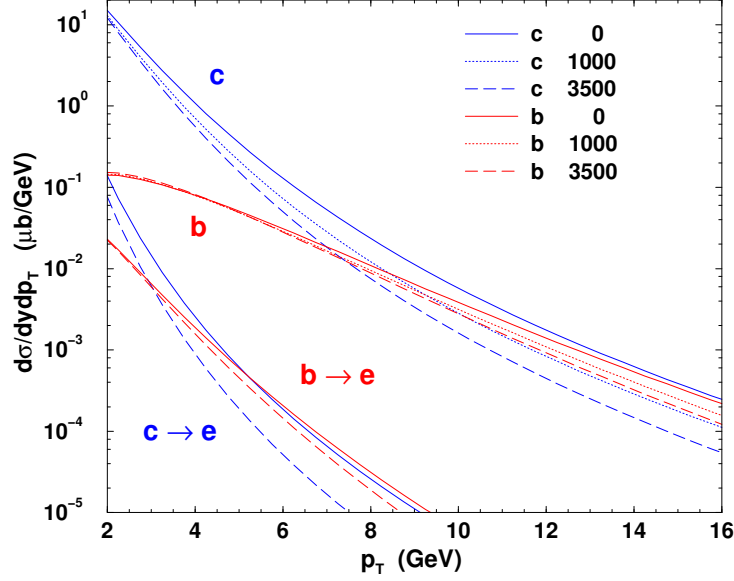
Figure 3.9: The differential cross section (per nucleon pair) of charm (upper blue) and bottom (upper red) quarks calculated to NLO in QCD [8] compared to single electron distributions calculated with the fragmentation and decay scheme of Ref.[8]. The solid, dotted and long dashed curves show the effect of DGLV heavy quark quenching with initial rapidity densities of $dN_g/dy = 0, 1000,$ and 3500, respectively. This figure is taken from [133].

3.5 Motivation of separating charm and bottom

As reviewed previous sections, heavy quarks (charm or bottom) are suitable probes to charactarize the property of the QGP. Although electrons from heavy flavor from the admixture of charm and bottom and D meson have been measured in RHIC and those data indicate that heavy quarks strongly interact with the medium, the energy loss mechanism of heavy quarks is still unclear.

The collisional and radiative energy loss can not be distiguished directly in experiments. However, since the different models predict different energy loss for charm and bottom quarks due to their large mass difference ($m_c \approx 1.3$ GeV, $m_b \approx 4.7$ GeV [3]), the charm and bottom separation in single electron spectrum plays an important role to discriminate those models or limit their model parameters which characterize the property of the QGP, for example, gluon density in DGLV theory or diffusion constant of heavy quarks in the Langevin-type approach.

As described in section 3.3.6, the large difference of lifetime of charm hadrons ($c\tau_{D^0} = 123$ μm, $c\tau_{D^\pm} = 312$ μm) and bottom hadrons ($c\tau_{B^0} = 455$ μm, $c\tau_{B^\pm} = 491$ μm) are useful to separate charm and bottom contribution in the single electron measurement. This feature brings us to develop the Silicon Vertex Tracker (VTX) which enables precision displaced tracking with a resolution < 100 μm and install it in PHENIX.

Chapter 4

Experiment

The data analyzed in this dissertation are Au+Au collisions at $\sqrt{s_{NN}} = 200$ GeV collected at the RHIC with the PHENIX detector at Brookhaven National Laboratory (BNL) in the year 2011. In this chapter the accelerator complex (section 4.1) and the details of the PHENIX detector (section 4.2) and its Data acquisition (DAQ) (section 4.3) are explained. After that, the detail of new VTX detector are described (section 4.4).

4.1   Relativistic Heavy Ion Collider (RHIC)

The Relativistic Heavy Ion Collider (RHIC) is a superconducting hadron collider located at Brookhaven National Lab (BNL) in Upton, New York. In the RHIC, the Heavy Ion collision(Au+Au,d+Au,U+U,Cu+Au..etc.) as well as polarized p+p collision experiment has been performed from the year 2000 [136]. Collisions are delivered to 6 interaction regions spread around the ring, four of which are occupied by the experiments PHENIX, STAR, PHOBOS, and BRAHMS. The PHOBOS and BRAHMS detectors completed data taking in 2006 and PHENIX and STAR are currently taking data at RHIC.

Table 4.1 shows the nuclear species,energies and integrated luminosity that RHIC delivered from 2000 to 2014. The analysis in this dissertation uses the data from Au+Au collisions at $\sqrt{s_{NN}} = 200$ GeV in data taking in year 2011 (RUN11).

The layout of the facility is shown in Figure 4.1. The accelerator complex consists from Tandem Van de Graaff, Booster Synchrotron (BS), Alternating Gradient Synchrotron (AGS) and the RHIC.

The Au ions with negative charge (Au$^-$) originate from a pulsed sputter ion source and are delivered to the Tandem Van de Graaff. The Au ions

45
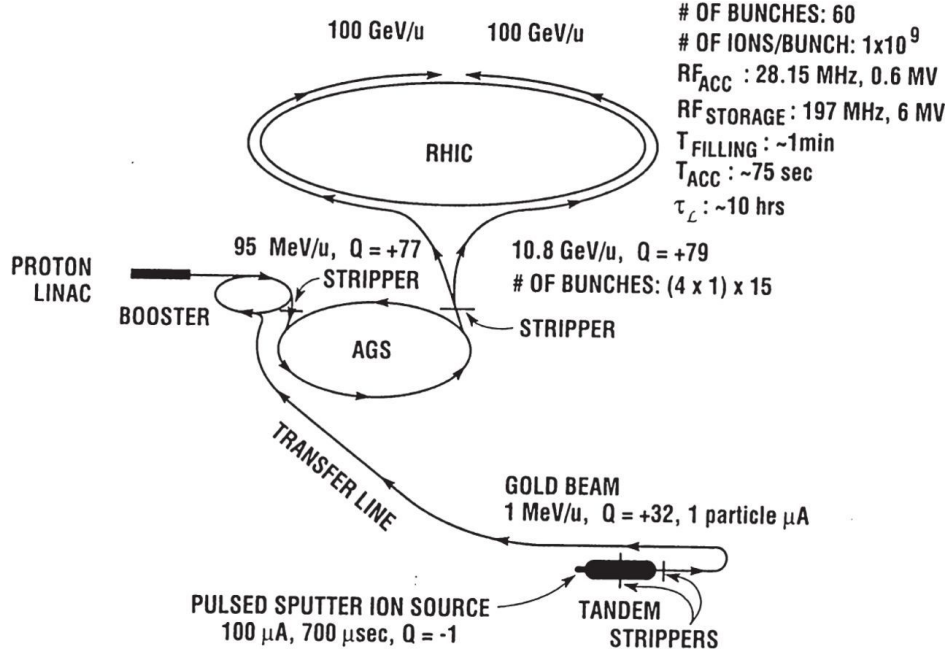
Figure 4.1:   Au ion pass through three accelerators (Tandem Van de Graaff, AGS Booster, and AGS) and four charge-stripping stations to prepare the fully stripped Au ions for injection to the RHIC ring [9].

are partially stripped of their atomic electrons with a foil located inside the Tandem's high voltage terminal, and accelerated up to ~ 1 MeV/nucleon. After further stripping at the exit of the Tandem and charge selection by bending magnets, beams of Au ions with a charge state of Au^{+32} are delivered to the Booster Synchrotron and accelerated to 95 MeV/nucleon. The ions are stripped again at the exit from the Booster to reach a charge state of Au^{+72} and injected to the AGS, where the Au ions are accelerated further to 10.8 GeV/nucleon, which is the require injection energy for the RHIC. Au ions, injected into the AGS in 24 bunches, are debunched and then re-bunched to four bunches at the injection front porch prior to acceleration. These four bunches are ejected at the top energy, one bunch at a time, and transferred to RHIC through the AGS-to-RHIC Beam Transfer Line. The final k-shell electrons are removed at the exit from the AGS and Au ions are fully stripped to a charge state of Au^{+79}.

The RHIC ring consists of two quasi-circular concentric rings on a common horizontal plane, one ("Blue Ring") for clockwise and the other ("Yellow Ring") for counter-clockwise beams. The rings are oriented so that the counter-rotating beams intersect with one another at six locations along their

3.8 km circumference with equal distance from one to the next, and collide head-on at intersections where detectors are located.

Table 4.1: Summary of data sets with collision species, collision energy, and integrated luminosity delivered to PHENIX.

RHIC run (year)	beam species	collision energy $\sqrt{s_{NN}}$	integrated luminosity
1 (2000)	Au+Au	130 GeV	7 μb^{-1}
2 (2001/2)	Au+Au	200 GeV	93 μb^{-1}
	p+p	200 GeV	0.35 pb^{-1}
3 (2002/3)	d+Au	200 GeV	24.2 nb^{-1}
	p+p	200 GeV	2.0 pb^{-1}
4 (2003/4)	Au+Au	200 GeV	1260 μb^{-1}
	p+p	200 GeV	3.0 pb^{-1}
5 (2005)	Cu+Cu	200 GeV	15.2 nb^{-1}
	p+p	200 GeV	12.6 pb^{-1}
6 (2006)	p+p	200 GeV	43.6 pb^{-1}
7 (2007)	Au+Au	200 GeV	3270 μb^{-1}
8 (2008)	d+Au	200 GeV	238 nb^{-1}
	p+p	200 GeV	19.2 pb^{-1}
9 (2009)	p+p	500 GeV	57.8 pb^{-1}
	p+p	200 GeV	60.7 pb^{-1}
10 (2010)	Au+Au	200 GeV	5.01 nb^{-1}
11 (2011)	p+p	500 GeV	89.9 pb^{-1}
	Au+Au	200 GeV	4.97 nb^{-1}
12 (2012)	p+p	200 GeV	37.9 pb^{-1}
	p+p	510 GeV	133 pb^{-1}
	U+U	200 GeV	368 μb^{-1}
	Cu+Au	200 GeV	13.5 nb^{-1}
13 (2013)	p+p	510 GeV	543 pb^{-1}
14 (2014)	Au+Au	200 GeV	23.1 nb^{-1}
14 (2014)	^{3}He+Au	200 GeV	72.3 nb^{-1}
15 (2015)	p+p	200 GeV	196.7 pb^{-1}
	p+Au	200 GeV	0.63 pb^{-1}
	p+Al	200 GeV	2.37 pb^{-1}

∗ Low energy runs are omitted in this table.

4.2 PHENIX experiment

The PHENIX experiment is the one of the large experiments being held at RHIC. In this section, the overview of PHENIX and relevant detectors used for this measurement are described.

4.2.1 Detector Overview

The PHENIX detector shown in Figure 4.2 was designed with precision charged particle reconstruction combined with excellent lepton identification [137].
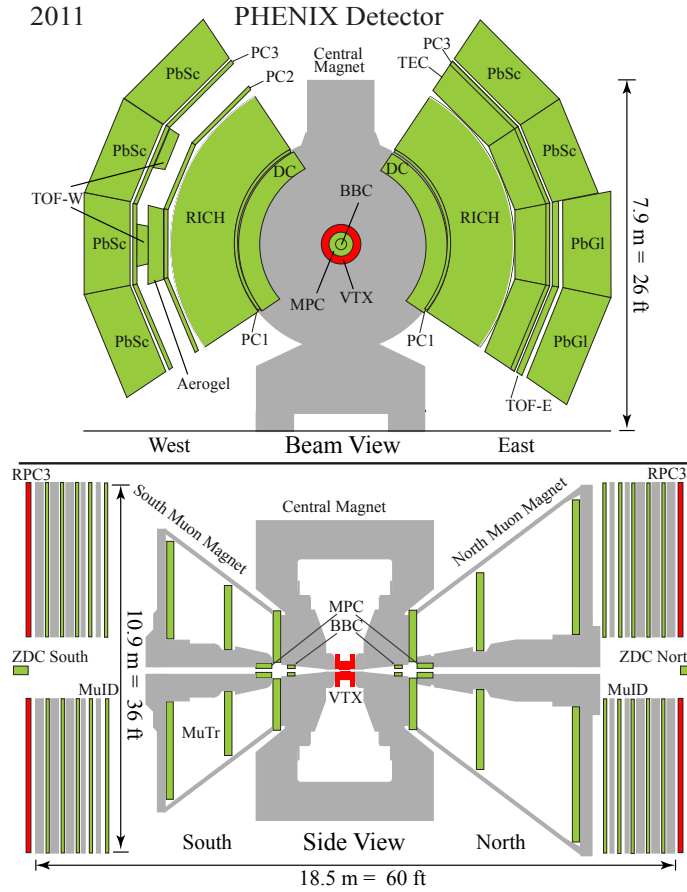
Figure 4.2: A schematic view of the PHENIX detector configuration for the 2011 run. Top figure is from beam stream at $z = 0$ and bottom figure is from the perpendicular to the beam stream.
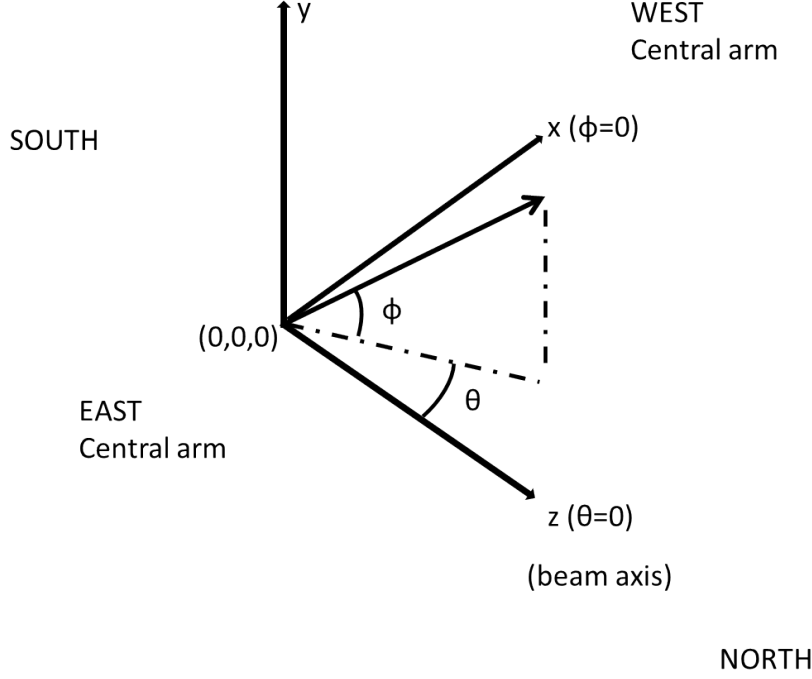
Figure 4.3: PHENIX global coordinate system.

Figure 4.3 shows the global coordinate system used in PHENIX. The z-axis is along with the beam direction, x-axis and y-axis are pointing to the center of west central arm and vertical top respectively. The rapidity, y, of a particle is defined as:

$$y = \frac{1}{2} \ln \frac{E + p_z}{E - p_z},$$

where E and p_z are energy and z component of momentum, respectively.

The pseudorapidity, η, of a particle is defined as:

$$\eta = \frac{1}{2} \ln \frac{1 + \cos \theta}{1 - \cos \theta},$$

where θ is the polar angle in Figure 4.3. If the mass of the particle can be ignored with respective to momentum of the particle, $\eta \approx y$. The pseudorapidity is often used instead of θ in high energy experiment.

The PHENIX detector comprises four spectrometers: two central arms at midrapidity ($-0.35 < \eta < 0.35$) and two muon arms at forward rapidity ($-2.2 < \eta < -1.2$ and $1.2 < \eta < 2.4$). The central arm consists of a number of subsystems and those detectors are optimized for detecting electrons,

hadrons and photons. A schematic view of the each subsystems is shown in Figure 4.2. In December 2010, the VTX was installed near the collision point as shown in Figure 4.2, which enables micro-vertexing capabilities.

4.2.2 Beam-Beam Counter and trigger

Figure 4.4: (Left) A picture of Beam-Beam counters module comprising 64 Čerenkov counters. (Right) A picture of quartz radiator and PMT.

The beam-beam counters (BBC) covering pseudorapidity $3.0 < |\eta| < 3.9$ and full azimuth are located at ± 1.44 meters along the beam axis and relative to the nominal beam-beam collision point. Each of the BBCs comprises 64 Čerenkov counters as shown in Figure 4.4.

Based on the coincidence of the BBCs, Au+Au collisions are selected via an online Minimum Bias (MB) trigger, which requires at least two counters on each side of the BBC to be fired.

The MB sample covers $96 \pm 3\%$ of the total inelastic Au+Au cross section with a $|z\text{-vertex}| < 10$ cm cut as determined by comparison with Monte Carlo Glauber models [5, 138] in 2011. The BBCs also provide a measure of the collision position along the beam axis (z-vertex) determined by the time-of-flight difference between hits in the two sets of BBC counters. The systematics shift of z-vertex position of BBC with respect to the central arm (~ 5 cm) was observed during the 2011 run and it was adjust by z-vertex provided from VTX. The z-vertex resolution of the BBC is approximately $\sigma_z = 0.6$ cm in central Au+Au collisions.

During 2011, the pre-scale factor which prevails events of $|z-\text{vertex}| < 12$ cm was set in the trigger algorithm to increase the number of events within the VTX acceptance. $\sim 85\%$ of all Au+Au collisions within that selection were recorded by the PHENIX high-bandwidth data acquisition system.

4.2.3 Central arms

Electrons (e^+ and e^-) are reconstructed using two central spectrometer arms as shown in Fig. 4.2, each of which covers the pseudorapidity range $|\eta| < 0.35$ and with azimuthal angle $\Delta\phi = \pi/2$. The detector configuration of the central arms is the same as in previous PHENIX Collaboration heavy flavor electron publications [11, 94], but there was no He bags in 2011.

The transverse momentum of each charged particle is determined by its bending radius in the magnetic field of central magnet system [139]. The magnet consists of an outer and inner coil inside a steel yolk, generating an symmetric axial magnetic field parallel to the beam axis. The field strength, B, is 0.9 Tesla around the beam pipe and gradually decrease along the radial position. The field integral $\int B \cdot dl$ is 1.15 (Tesla $\cdot$ m) at $\phi = 90°$.

The central arms are easily moveable to allow access to detector components for commissioning and maintenance.

Charged particle tracks are reconstructed outside of an axial magnetic field using layers of drift chamber (DCH) and multi-wire proportional pad chambers (PC). The momentum resolution is $\sigma_p/p \simeq 0.7\% \oplus 0.9\% \, p$ (GeV).

Electron identification is performed by hits in a ring imaging Čerenkov detector (RICH) and a confirming energy deposit in an electromagnetic calorimeter (EMCal).

4.2.4 Drift Chamber

The Drift Chambers (DCH) are main tracking detectors in central arms. DCHs are placed at the front of both the East and the West arms with a radius of 2.0 to 2.4 m far from the beam axis in a residual magnetic field with a maximum of 0.06 Tesla[10]. Each DCH has a cylindrical shape with $|z| \leq 90$ cm and $\pi/2$ azimuthal angle (ϕ) coverage as shown in Figure 4.5. There are 6 types of wire modules stacked radially in each sector. They are called X1, U1, V1, X2, U2 and V2. Each module contains 4 sense planes and 4 cathode planes forming wire cells with a 2 - 2.5 cm drift space in the ϕ direction. The X1 and X2 wire cells run in parallel to the beam axis to measure particle trajectories in r - ϕ. The U and V wires are tilted with about 6° rotation with respect to the X wires, and measure the z-coordinate of the track.

Each of the X- and U,V-stereo cells contain 12 and 4 anode (sense) wires, respectively. As a result, there are 40 drift cells in the DCH located at different radii. The layout of wires within one DCH sector is shown in Figure 4.6. The stereo wires start in a sector on one side and end in a neighboring sector on the other side of the DCH.
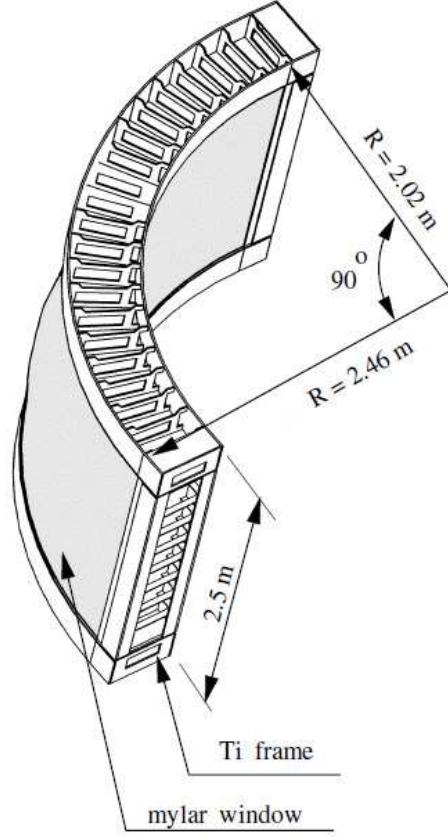
Figure 4.5:   A schematic view of Drift Chameber

To reduce the single wire occupancy, the wires are electrically isolated into two halves at the center of the DCH (z = 0) using kapton of 100 μm thickness. Therefore, the DCH system has 6400 sense wire (40/2 wires/cell * 80 cells/side * 2 sides/arm * 2 arms = 6400 wires). The DCH operates with a mixture of 50% Ar, 50% ethane gas and small fraction of alcohol.

4.2.5   Pad Chamber

The Pad Chambers (PC) provide the hit information in z-direction and this is used with DCH hit information to reduce track ambiguities in high multiplicity environment. The PCs consist of three individual layers of multi-wire proportional chambers [10].

As shown in Figure 4.2, the first inner layer of the PC (PC1) are placed between the DCH and the RICH in both the East and the West arms. The second layer (PC2) is located behind the RICH in the West arm only. The
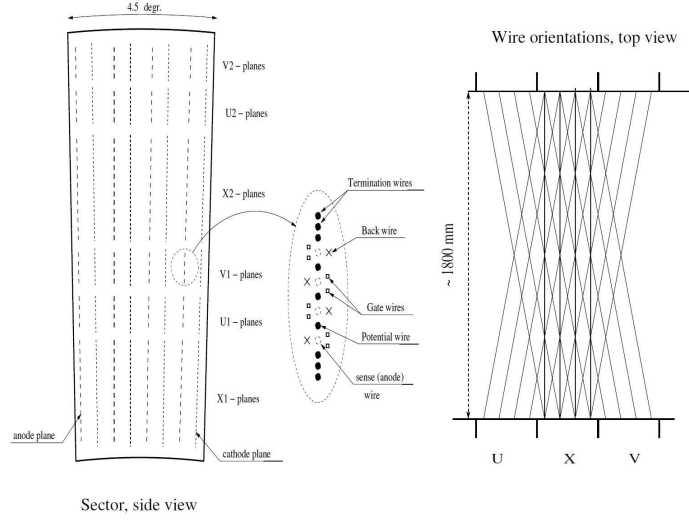
Figure 4.6: (Left) The layout of DCH wire position within one sector and inside the anode plane. (Right) Top view of the DCH stereo wire orientations.

third layer (PC3) is mounted in front of the EMCal The installed radii of these three PC layers correspond to 248, 419 and 490 cm from the beam pipe, respectively.

Each PC contains a single plane of wires inside a gas volume bounded by two cathode planes. One cathode is finely segmented into an array of pixels. The charge induced on a number of pixels when a charged particle starts an avalanche on an anode wire, is read out through specially designed readout electronics.

A special pad design was invented to archive a high pixel granularity and small readout channels. Figure 4.7 (left) shows the pixel configuration of a pad. The nine by nine interleaved pixels are grouped together to form single readout channel. Each cell recognizes a valid hit and contains three pixels which are connected to different but neighboring pads shown in Figure 4.7 (right). So, the hit information can be broken down to the cell level by identifying the triplets of the pads. The cell size is 8.4 mm for the PC1 and PC2 , and is twice for the PC3, since the PC3 is twice far from the beam pipe compared to the PC1. The spacial resolutions of the PC1 and PC3 in z direction is $\pm$ 1.7 mm and $\pm$3.6 mm, respectively.
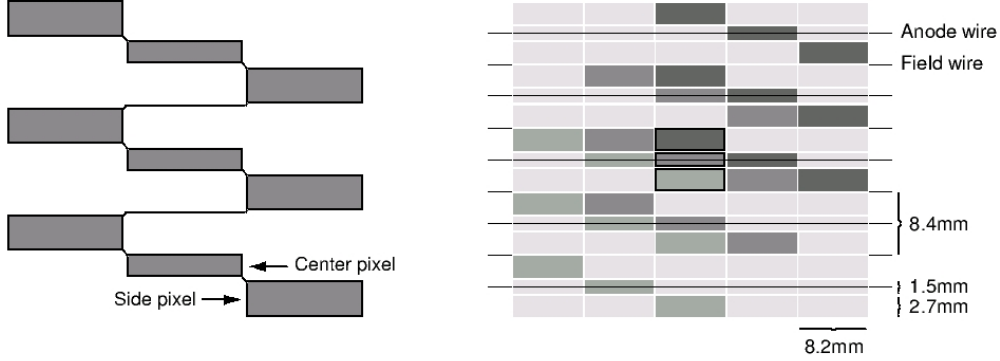
Figure 4.7: The pad and pixel geometry in the pad chamber. A cell defined by three pixels is at the center of the right picture.

4.2.6 Ring Imaging Čerenkov Detector

The Ring Imaging Čerenkov detector (RICH) [10, 140] is a gas Čerenkov detector and is a primary device for identifying electrons among the very large number of charged hadrons ($\mathcal{O}(1000)$ times larger than electrons). The RICH is placed behind the PC1 in both the East and the West arms. Figure 4.8 shows a cutaway view of the RICH. The RICH consists of a 40 m^3 gas vessel with an entrance and exit windows of the aluminized Kapton, 48 composite mirror panels, forming two intersecting spherical mirrors and two arrays of $80(\phi) \times 16(z)$ photo multiplier tubes (PMT). A PMT array is placed behind the central magnet so that particles from the collision do not directly hit the PMT array as shown in Figure 4.9. The PMTs are equipped with 2 inch diameter Winston cones and have magnetic shields that allow them to operate at up to 100 Gauss. The spherical mirror reflects the Čerenkov photons emitted from an electron and focuses on the PMT array forming a ring-shaped pattern. The diameter of the Čerenkov ring which corresponds the emission angle of the Čerenkov photon. The vessel is filled with CO_2 gas at 1 atm as Čerenkov radiator. This corresponds to Čerenkov threshold of 4.65 GeV/c for pion and produces an average of 12 photons per ring for a completely relativistic particle. The diameter of CO_2 gas is about 11.8 cm.
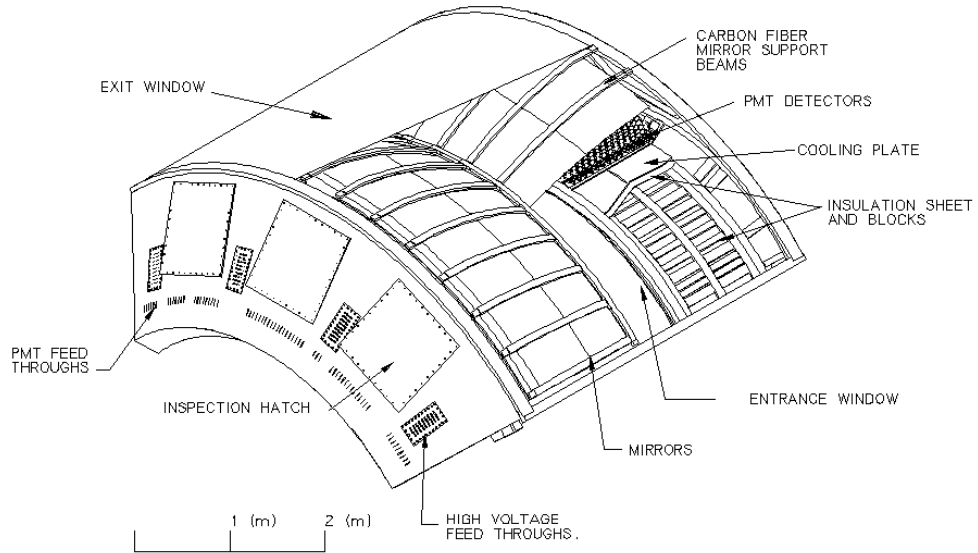
Figure 4.8: A cutaway view of one arm of the RICH detector [10].
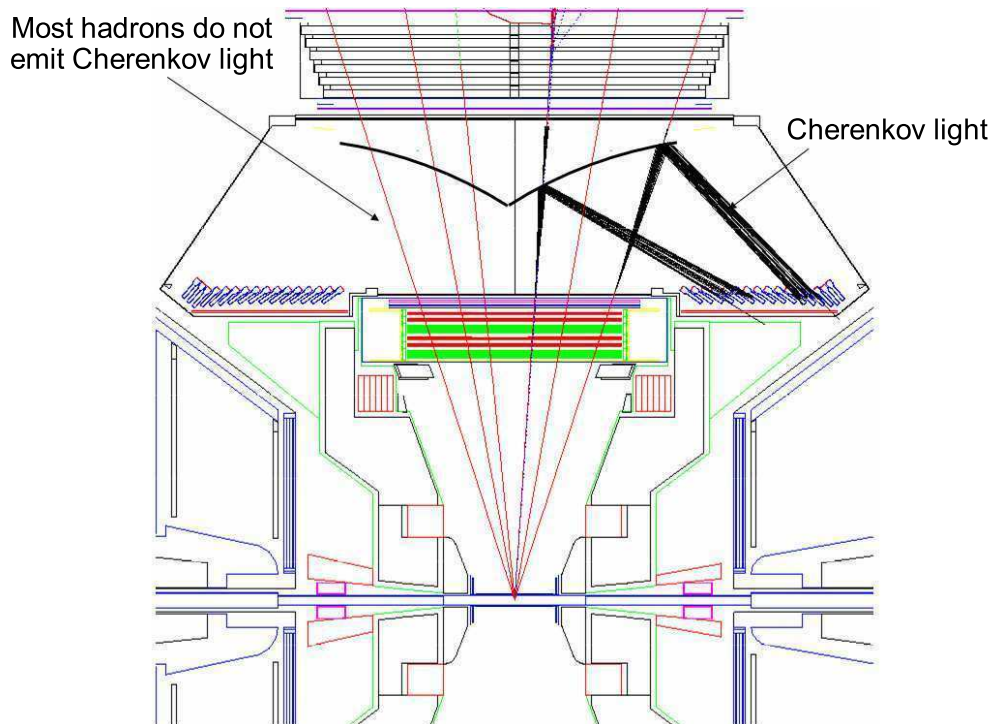
Figure 4.9: Top view of the RICH in the PHENIX east arm [11].

55

4.2.7 Electromagnetic Calorimeter
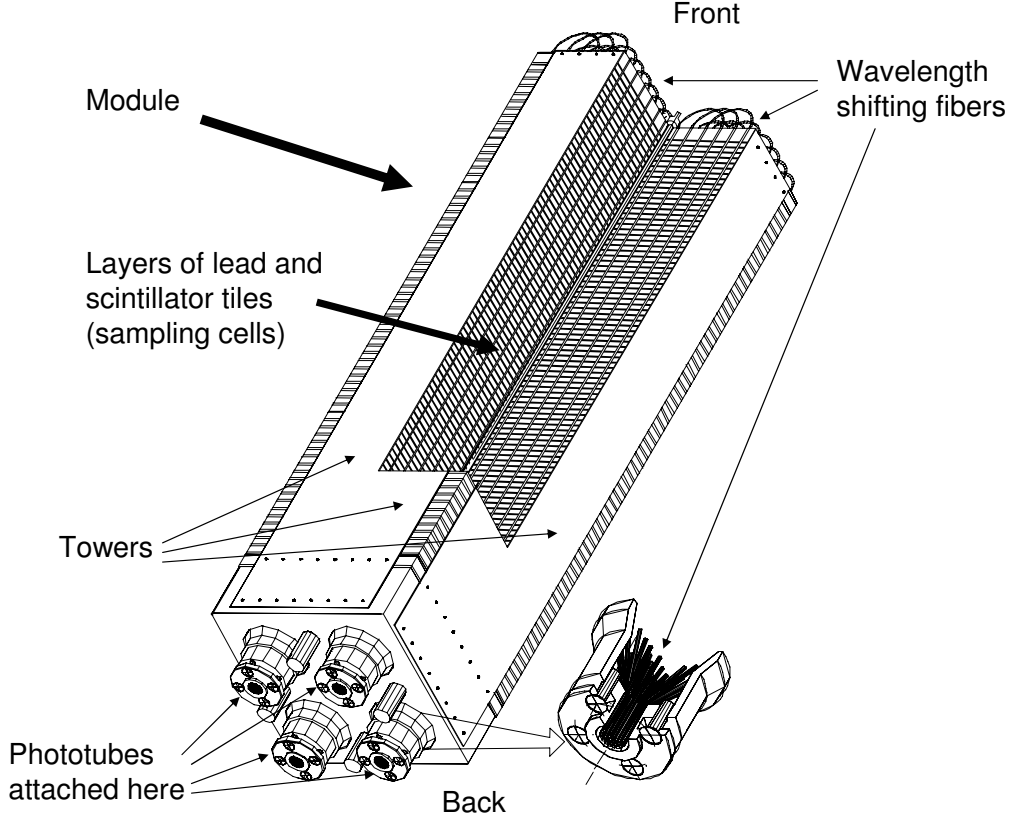
Figure 4.10: Schematic view of a Pb-scintillator (PbCc) module

The electromagnetic calorimeter (EMCal) [141] is used to measure the spatial position and energy of electrons and photons produced in heavy ion collisions. The EMCal is located at the most outside of the central arm. The EMCal consists of two different detector systems. One is a Pb-Scintillator calorimeter (PbSc, Figure 4.10) which provides 4 and 2 sectors for the West and East arms, and the other is Pb-Glass calorimeter (PbGl, Figure 4.11) which occupies 2 lower sectors of the East arm. The location of the PbSc and the PbGl calorimeters are shown in Figure 4.2.

The PbSc is a shashlik type sampling calorimeter made of alternating tiles of Pb and scintillator and consists 15552 individual towers. Each PbSc tower contains 66 sampling cells ($55 \times 55 \times 375$ mm^3) and has a thickness of 18 radiation length (X_0) and about 30 mm of Molie're radius. These cells are optically connected 36 longitudinally penetrating wavelength shifting fibers for light collection. Light is readout by 30 mm PMT (FEU115M) at the back
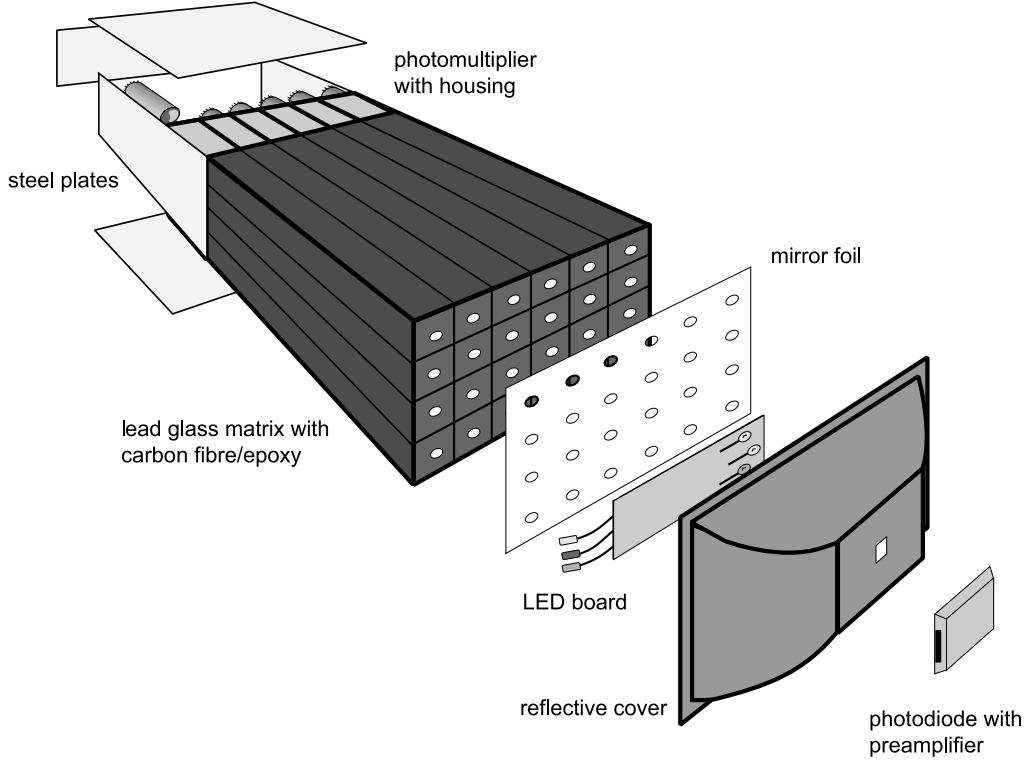
Figure 4.11:   Schematic view of a Pb-glass (PbGl) module

of the towers. A single basic structure is called as a module which consists of 4 towers. On the other hand, the PbGl is Cerenkov calorimeter which consists of 9216 lead glass modules with PMT readout (FEU84). Each PbGl module is $40 \times 40 \times 400$mm^3 and has 14.4 X_0 and 36 mm of Molie're radius. The PbGl has been used previously in CERN WA98 experiment [142]. Figure 4.10 shows an unit array of the PbGl modules. The EMCal has an important role in particle identification using the informations of measured energy, time and shower shape of electromagnetic cascade. The energy resolutions of the PbSc and the PbGl are obtained using electron and positron beam at a test experiment for the PbSc and the PbGl respectively:

$$\frac{\sigma_E}{E}_{Pbsc} = \frac{8.1\%}{\sqrt{E \text{ (GeV)}}} \oplus 2.1\%$$

$$\frac{\sigma_E}{E}_{PbGl} = \frac{5.9\%}{\sqrt{E \text{ (GeV)}}} \oplus 0.8\%$$

57

4.3 Data Acquisition
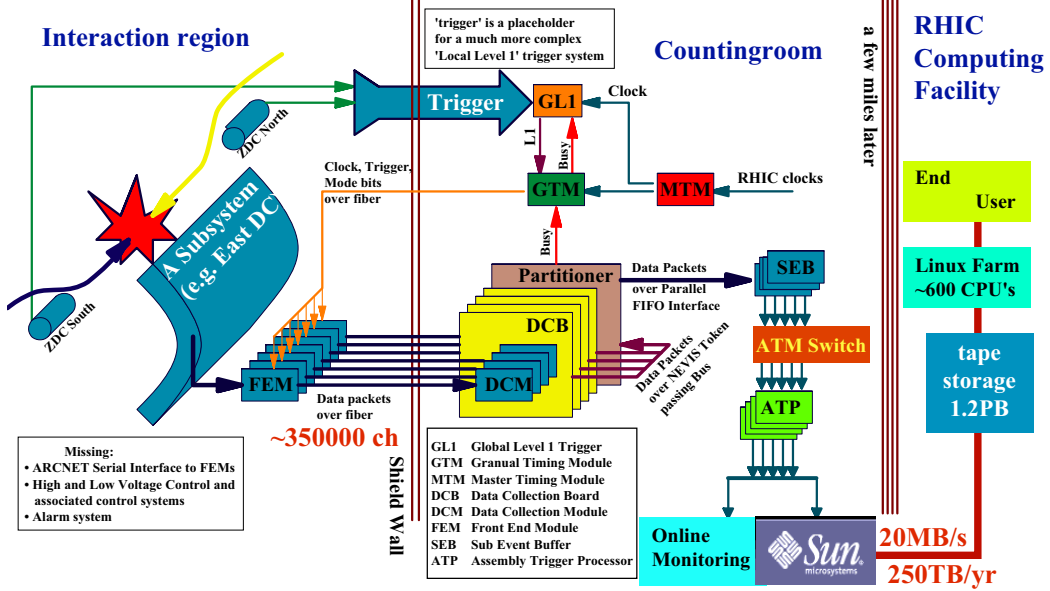
Figure 4.12: A schematic diagram of the PHENIX Data Acquisition system.

The number of tracks passed through the detector varies from only a few tracks in $p+p$ to several hundred tracks in central Au+Au collisions. The expected interaction rate also varies from a few kHz from central Au+Au to approximately 500 kHz for $p+p$ collisions. To handle a variety of event size and rate seamlessly, the PHENIX Data Acquisition system (DAQ) [143] consists of the detector front ends equipped with the pipelined and dead-timeless features and higher level trigger systems. Figure 4.12 shows a general schematic diagram of the PHENIX DAQ. The RHIC delivers the 9.4 MHz fundamental clock which corresponds to 106 ns of time interval between beam crossings. All of PHENIX Front End Electronics modules are synchronized to the RHIC clock. Signals produced in the various subsystems are processed by Front End Modules (FEMs) that converts the detector analog signals into digital data. The FEM for each subsystem is placed in the PHENIX Intersection Region (IR). A FEM module can buffer the data to wait for the Level-1 trigger LVL1 decisions and to wait for digitization and readout of triggered event. The RHIC clock is received by the Master Timing Module (module). The MTM distributes the master clock by fanning out the RHIC clock, where the internal phase locked loop is used to minimize the clock jitter. The master clock is transmitted to the FEM via the Granual

Timing Module (GTM). Thus, all the FEM's are processed in a single clock. The GTM is prepared for a unit of detector elements. In addition, the GTM send the control commands (mode bits) and trigger decisions. The purpose of the Level-1 trigger (LVL1) is to select interesting events and provide event rejection for the limited DAQ rate. The Global Level-1 (GL1) system generates the LVL1 decision based on logical combinations of the Local Level-1 (LL1) decisions. The LL1 is generated by individual trigger detector. The GL1 can treat totally 128 bits of the LL1 inputs to make the LVL1 decision. Once the LVL1 decision is generated, the decision signal is sent to the FEM via the GTM, then the data buffered in the FEM are transfered to the Data Collection Module (DCM) located at the PHENIX Counting House. The FEM, GTM and DCM are connected via a fiber optic cable to eliminate a large number of noise, cross-talk and grounding problems. At the maximum LVL1 trigger rate, the whole FEM's send over 100 Gbytes of data per second. The DCM is designed to receive this large amount of data. After receiving the data, the DCM performs the zero suppression, error checking and data formatting to generate data packets. The zero suppression is to compress the data by comparing the preset threshold. In addition, the DCM provides a busy signal which are returned to the GL1 to hold off further triggers. Many parallel streams of the data packets from the DCMs are sent to the event builder (EVB). The EVB performs the final stage of event assembly.In the EVB, the streams of the data packets from the DCMs are first received and buffered in a set of the Sub Event Buffers (SEB). These data are transfered on request to a set of Assembly/Trigger Processors (ATP) via Asynchronous Transfer Mode switch (ATM). The final events assembled in the ATPs are transmitted to the PHENIX Online Control System (ONCS) for logging and monitoring processes. The format of the final event is called "PHENIX Raw Data Format (PRDF)". The raw data are sent to High Performance Storage System (HPSS) at RHIC Computing Facility (RCF) and converted to physical quantities for analysis.

4.4 Silicon Vertex Tracker Upgrade

Silicon Vertex Tracker (Silicon Vertex Tracker (subsystem of PHENIX) (VTX)) is used for pricise collision vertex (primary vertex) in 3 dimensional space as well as displaced track measurement. The detail of VTX detector is described in this section.
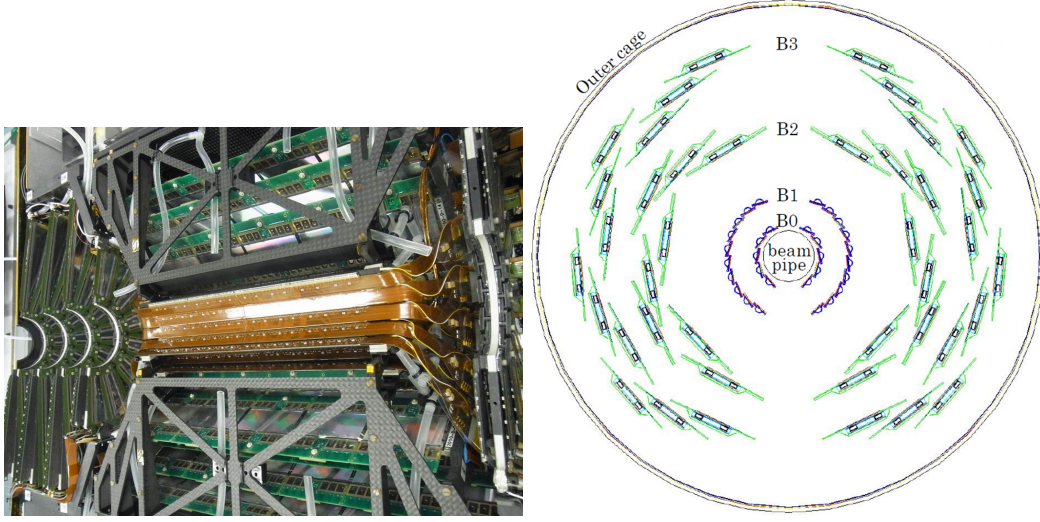
Figure 4.13: (Left) A picture of the one side of the VTX detector. (Right) A schematic view of the VTX detector from beam steam with the individual ladders shown.

The (VTX) (Figure 4.13 (left) was installed near the collision point as shown in Figure 4.2 in December 2010. In addition, a new beryllium beam pipe with 2.16 cm inner diameter and 760 μm nominal thickness (0.24 % radiation length (X_0)) was installed to reduce conversion electrons and multiple-scattering before the VTX detector.

The VTX detector [28, 144, 145] consists of four cylindrical layers of silicon detectors as shown in Figure 4.13 (right). The detector is separated into west and east arms, each with nominal acceptance $\Delta\phi \approx 0.8\pi$ centered on the acceptance of the outer PHENIX central arm spectrometers. The detector covers pseudorapidity $|\eta| < 1.2$ for collisions taking place at $z = 0$. The VTX can precisely measure the vertex position of a collision within $|z| < 10$ cm range of the center of the VTX. The main characteristics of the VTX detector are summarized in Table 4.3.

The two inner layers, referred to as B0 and B1, of the VTX detector comprise silicon pixel detectors [146]. B0 (B1) comprises 10 (20) pixel ladders (Figure 4.16) with a central radial position of 2.6 (5.1) cm. The silicon pixel

Table 4.3: A summary of the VTX detector. For each layer (B0 to B3), the detector type, read out chip, the central radius (r), ladder length (l), sensor thickness (t), sensor active area ($\Delta\phi \times \Delta z$), the number of sensors per ladder (N_S), the number of ladders (N_L), pixel/strip size in ϕ ($\Delta\phi$) and z (Δz), the number of read-out channels (N_{ch}), and the average radiation length including the support and on-board electronics (X_0) are given.

Layer		B0	B1	B2	B3
read out chip		ALICE1LHCb	ALICE1LHCb	SVX4	SVX4
	type	pixel	pixel	stripixel	stripixel
	r (cm)	2.6	5.1	11.8	16.7
sensor area	l (cm)	22.8	22.8	31.8	38.2
	t (μ m)	200	200	625	625
	$\Delta\phi$ (cm)	1.28	1.28	3.07	3.07
	Δz (cm)	5.56	5.56	6.00	6.00
	N_S	4	4	5	6
	N_L	10	20	16	24
pixel/strip size	$\Delta\phi$ (cm)	50	50	80	80
	Δz (cm)	425 (625)	425 (625)	3×10^4	3×10^4
	N_{ch}	1.3×10^6	2.6×10^6	1.2×10^5	2.2×10^5
	X_0 (%)	1.3	1.3	5.2	5.2

technology is based on the ALICE1LHCb sensor-readout chip [147], which was developed at CERN. Each ladder is electrically divided into two independent half-ladders. Each ladder comprises four sensor modules mounted on a mechanical support made from carbon-fiber composite.

As shown in Figure 4.14, each sensor module comprises a silicon pixel sensor with a pixel size of 50 μm(ϕ) $\times$ 425 μm(z). In the region between two chips, the pixel sensor cells are elongated in z (625 μm instead of 425 μm) to eliminate the dead area between chips. The silicon sensors are produced as p-in-n structures on 200 μm thick silicon. One pixel readout chip reads 256 (ϕ)$\times$ 32 (z)= 8192 pixels and covers approximately 1.3 cm ($\Delta\phi$)$\times$ 1.4 cm (Δz) of the active area of the sensor. The number of pixels in total is 8192 (pixels/chip) $\times$ 4 (chips/sensor) $\times$ 4 (sensors/ladder) $\times$ 30 (ladders) = 3932160. The position resolution is $\sigma_\phi = 14.4$ μm in the azimuthal direction and $\sigma_z = 123$ μm in the z direction. The typical operation bias voltage is 30 V.

Each pixel is interconnected with four pixel readout chips by bump-bonding technique, which connect electrical structures with small balls of solder. Figure 4.15 shows the schematic of the circuitry within one pixel

Pixel sensor Active Area
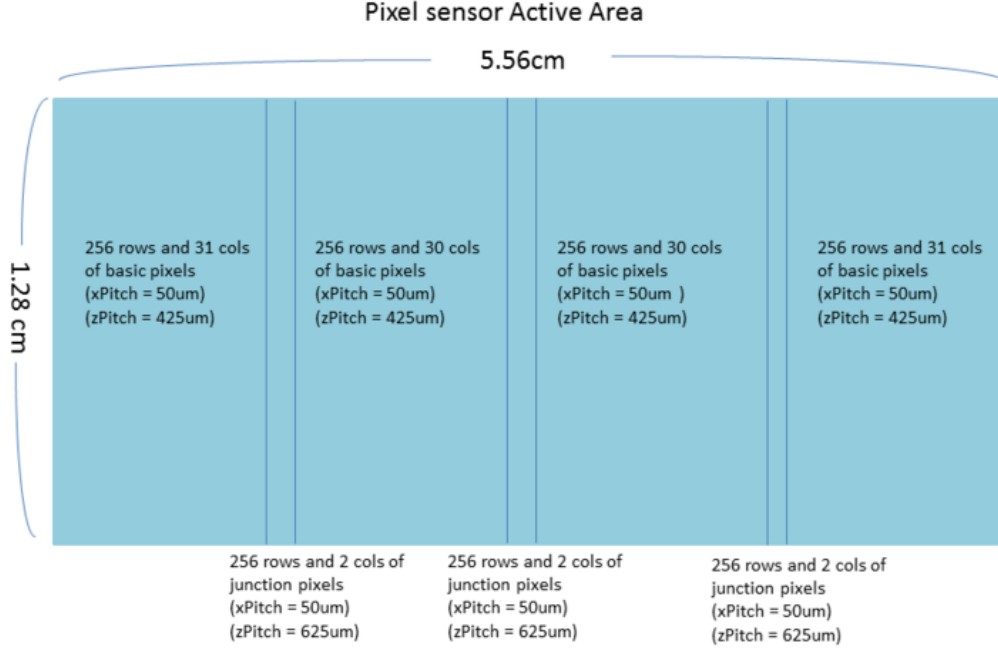
Figure 4.14: schematic view of a pixel sensor

cell in the ALICE1LHCb chip. Each readout chip has 32×256 amplifier-discriminators for individual channel and the binary output of the discriminator is delayed with a programmable delay and stored for readout by the downstream data acquisition system (DAQ). When the readout is issued, the data is transferred to Silicon Pixel Interface Read-Out (SPIRO) module through the readout bus mounted on the sensor module (Figure 4.16 (bottom)). The readout bus is manufactured using flexible printed circuit (FPC) board technology [148]. The bus consists of four 3μ m copper signal layers and two 50 μm aluminum power layers (power and ground). The structural material for the bus is Polyimide. SPIRO module provides all service voltages, timing and control signal, reads out the data from pixel ladder and transfer it to the front end module (FEM) via optical cable.
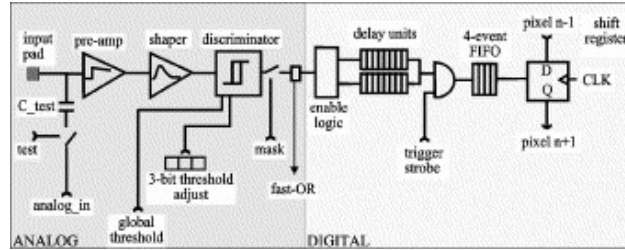
Figure 4.15: A schematic of the circuitry within one pixel cell in the AL-ICE1LHCb sensor-readout chip. Reprinted from [147] with permission from Elsevier.
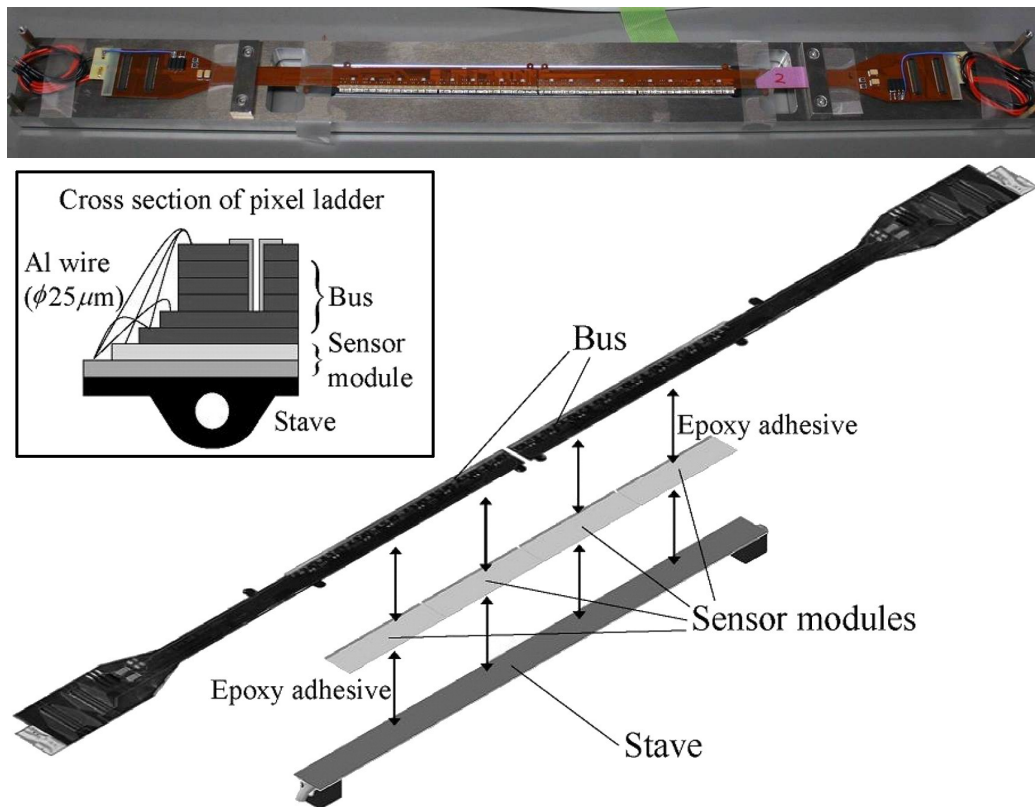
Figure 4.16: (Top) A picture of a pixel ladder. (Bottom) Schematic view of a pixel ladder.

63

The two outer layers of the VTX detector, referred to as B2 and B3, are constructed using silicon stripixel sensors, as detailed in Ref. [149, 150]. The B2 (B3) layer comprises 16 (24) silicon stripixel ladders at a central radial distance of 11.8 (16.7) cm. The stripixel sensor is a novel silicon sensor, and is a single-sided, N-type, DC-coupled, two-dimensional (2-D) sensitive detector. One sensor has an active area of approximately 30 mm × 60 mm, which is divided into two independent sectors of 30 mm × 30 mm. Each sector is divided into 384 × 30 pixels. Each pixel has an effective size of 80 μm (ϕ) × 1000 μm (z), leading to a position resolution of σ_ϕ=23 μm in azimuthal direction.
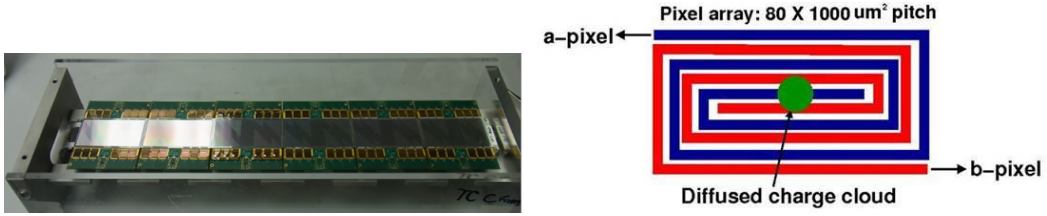
Figure 4.17: (Left) A picture of a stripixel detector. (Right) Schematic view of a stripixel with two independent interleaved a-pixel (blue) and b-pixel (red) [151].
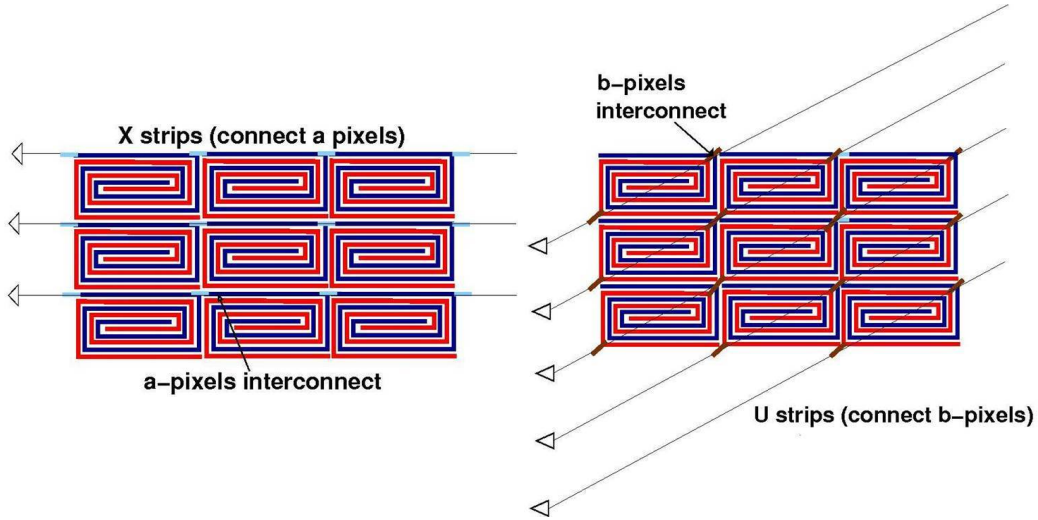
Figure 4.18: (Left) X strips formed by a-pixels. (Right) U strips formed by b-pixels. These figures are from [151].

As shown in Figure 4.17, a pixel comprises two spiral shape implants (a-pixel and b-pixel) interleaved such that the charge deposited by ionizing

particles are registered by both implants. There are 30 a-pixel implants along the beam direction, connected to form a 30 mm long X-strip, and 30 b-pixel implants are connected with a stereo angle of 80 mrad to form a U-strip. X-strip and U-strip are visualized in Figure 4.18. When a charged particle hits a pixel, both the X- and the U-strip sharing the pixel register a hit. Thus the hit pixel is determined as the intersection of the two strips. This design allows to simplify fabrication process for both the sensor and readout compared with that for the double-sided strip sensor.
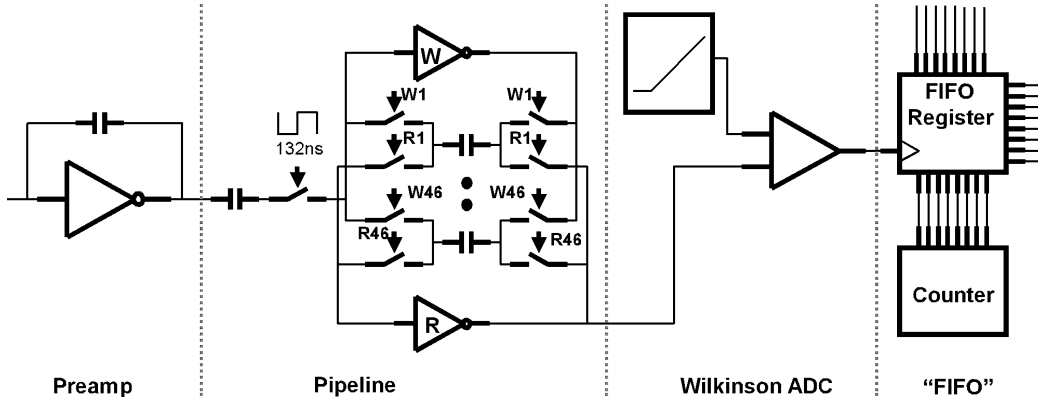
Figure 4.19: Conceptual schematic of a single SVX4 channel circuit [152]. ©2004 IEEE.

The stripixel sensor is read out with the SVX4 chip developed by a FNAL-LBNL Collaboration [153]. The stripixel sensor and each SVX4 channel are DC-coupled. It contains 128 parallel charge integration channels, a 128 × 46-cell analog latency pipeline capable of buffering up to 4 samples, and Wilkinson type 8 bit analog to digital converters (ADCs). ADCs information are used as weighting factor of hit information for clustering (subsection 5.4.2) as well as dE/dx measurement. Figure 4.19 shows the conceptual schematic of a single SVX4 channel circuit.

The total number of channels in stripixel layers is 128 (channels/chip) × 12 (chips/sensor) × (5 (sensors/ladder) × 16 (ladders/B2 layer) + 6 (sensors/ladder) × 24 (ladders/B3 layer) = 344064. The typical operation bias voltage is 200 V.

The detector occupancy for the central Au+Au at 200 GeV is studied by using GEANT3 [154] model of the VTX detector and the HIJING [155] event generator. The result of the simulation is summarized in the Table 4.4.

Table 4.4:   Occupancy of the each VTX layer for central Au+Au collisions at 200 GeV

Layer	Occupancy
B0	0.53%
B1	0.16%
B2	4.5% (X strip) 4.7% (U strip)
B3	2.5% (X strip) 2.7% (U strip)

Chapter 5

Analysis

5.1 Overview

The purpose of the analysis is to separate the electrons from charm hadron decays and those from bottom hadron decays. The life time of B mesons ($c\tau_{B^0}$ = 455 μm, $c\tau_{B^\pm}$ = 491 μm [3]) is substantially longer than that of D mesons ($c\tau_{D^0}$ = 123 μm, $c\tau_{D^\pm}$ = 312 μm) and the decay kinematics are different. This means that the distribution of values for the distance of closest approach (DCA) of the track to the collision vertex (primary vertex) for electrons from bottom decays will be broader than that of electrons from charm decays. Thus $c \rightarrow e$, $b \rightarrow e$ can be separated via precise measurement of the DCA distribution and p_T distribution. There are other sources of electrons, namely Dalitz decays of π^0 and η, direct virtual photon, photon conversions in the material, K_{e3} decays, and $J/\psi \rightarrow e^+e^-$ decays. With the exception of electrons from K_{e3} decays, these background components have DCA distributions narrower than those from charm decay electrons. These background components are subtracted before the charm/bottom separation.

In the first step of the analysis, good events where the collision vertex is within the acceptance of the VTX detector are selected, and its function is normal (section 5.5). Then electron tracks are reconstructed in the PHENIX central arms (section 5.4.4). They are then associated with hits in the VTX detector and their DCA is measured (section 5.6). At this point, the DCA distribution of inclusive electrons has contributions from heavy flavor electrons ($b \rightarrow e$ and $c \rightarrow e$) and several background components.

The next step is to determine the DCA shape and normalization of all background components (section 5.7). They include mis-identified hadrons, background electrons with large DCA caused by high-multiplicity effects, photonic electrons (Dalitz decay electrons, photon conversions), and elec-

trons from K_{e3} and quarkonia decays. The shapes of the DCA distributions of the various background electrons are determined via data driven methods or Monte Carlo simulation (DCA cocktail method). Then the normalization of those background electron components in the data is determined (section 5.8).

Because the amount of the VTX detector material is substantial (13% of one radiation length) the largest source of background electrons is photon conversion within the VTX. This background is suppressed by a conversion veto cut (section 5.7.4)

Once the shape and the normalization of all background components are determined and subtracted, the DCA distribution of heavy flavor decay electrons can be described as a sum of $b \to e$ and $c \to e$ DCA distributions. The heavy flavor DCA distribution is decomposed by an unfolding method (section 5.9).

5.2 Track reconstruction in Central arms

Charged particle tracks are reconstructed using the outer central arm detectors, DCH and PC [94]. The DCH has six types of wire modules stacked radially, named X1, U1, V1, X2, U2, and V2 (see subsection 4.2.4). The X wires run parallel to the beam axis in order to measure the ϕ-coordinate of the track and the U and V wires have stereo angles varying from 5.4 to 6.0 degrees. Tracks are required to have hits in both the X1 and X2 sections along with uniquely associated hits in the U or V stereo wires and at least one matching PC hit, to reduce mis-reconstructed tracks. The track momentum vector is determined assuming the particle originated at the Au+Au collision vertex as reconstructed by the BBC. The incident angle of the incoming track at a reference radius within the DCH, α, is a measure of the momentum vector and charge of the particle, as shown in Figure 5.1.

5.3 Electron identification

Electron candidates are selected by matching tracks with hits in the RICH and energy clusters in the EMCal. The details on the electron selection cuts are given in Ref. [11]. In this analysis we select electron candidates within $1.0 < p_T < 5.0$ GeV/c , and we briefly describe the cuts in the RICH and EMCal below.

Čerenkov photons from an electron track produce a ring-shaped cluster in the RICH. At least three associated PMT hits are required in the RICH and
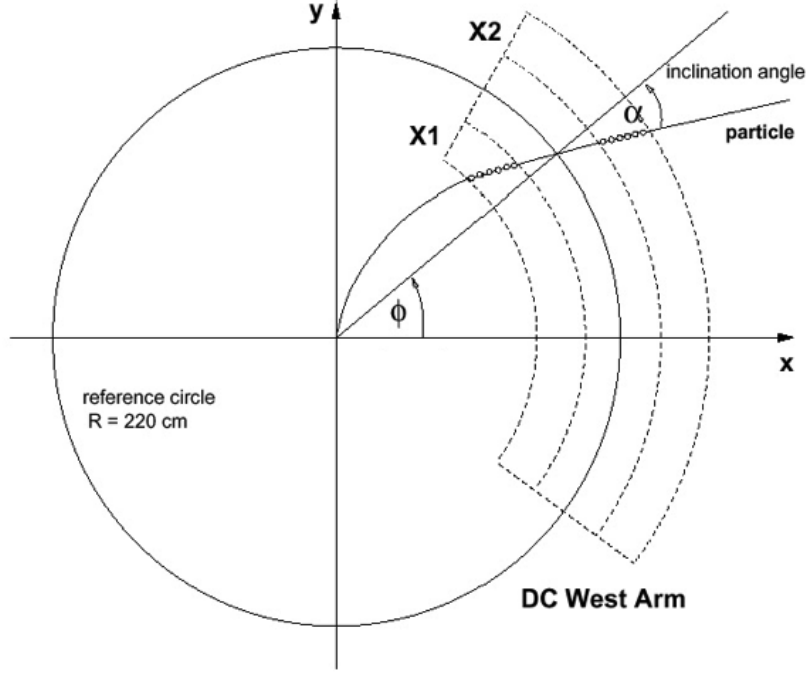
Figure 5.1: Charged particle momentum vector reconstruction using DCH hit information [12].

a ring-shape cut is applied. The center of the ring is required to be within 5 cm of the track projection. The probability that the associated cluster in the EMCal comes from an electromagnetic shower is calculated based on the shower shape. Based on that probability, tracks are selected in a way that maintains high efficiency for electrons while rejecting hadrons. Further, the energy (E) in the EMCal is required to match the track determined momentum (p). This match is calculated as $dep = (E/p - \mu_{E/p})/\sigma_{E/p}$, where $\mu_{E/p}$ and $\sigma_{E/p}$ are the mean and standard deviation respectively of a Gaussian fit to the E/p distribution, determined as a function of momentum as shown in Figure 5.2. A cut of $dep > -2$ is used to further reject hadrons that have an E/p ratio < 1, because they do not deposit their full energy in the EMCal.

In high-multiplicity Au+Au events there is a significant probability for a random association between the track and hits in the RICH and EMCal. This mis-identified hadron probability is estimated as follows. The $z < 0$ and $z > 0$ sides of the RICH have their hits swapped in software, and the tracks are re-associated with RICH hits. Because the two longitudinal sides of the RICH are identical, this gives a good estimate of the random hadron background in the electron sample.

69

The distribution of electron candidates at $p_T = 1.0 - 5.0$ GeV/c for the normalized EMCal energy to track momentum ratio, dep defined above, is shown in Figure 5.2. There is a large peak near zero from true electrons as expected and a clear low-side tail from mis-identified hadron. Also shown is the result of the above swap method. The difference between the data (black) and the "swap" distribution (red) is explained as contributions from off-vertex electrons caused by conversions from the outer layer of the VTX and weak decay of kaon. In the final accounting for all contributions to the identified-electron DCA distribution, we utilize this swap method to statistically estimate the contribution of mis-identified hadron in each p_T selection as detailed in Section 5.7.2.
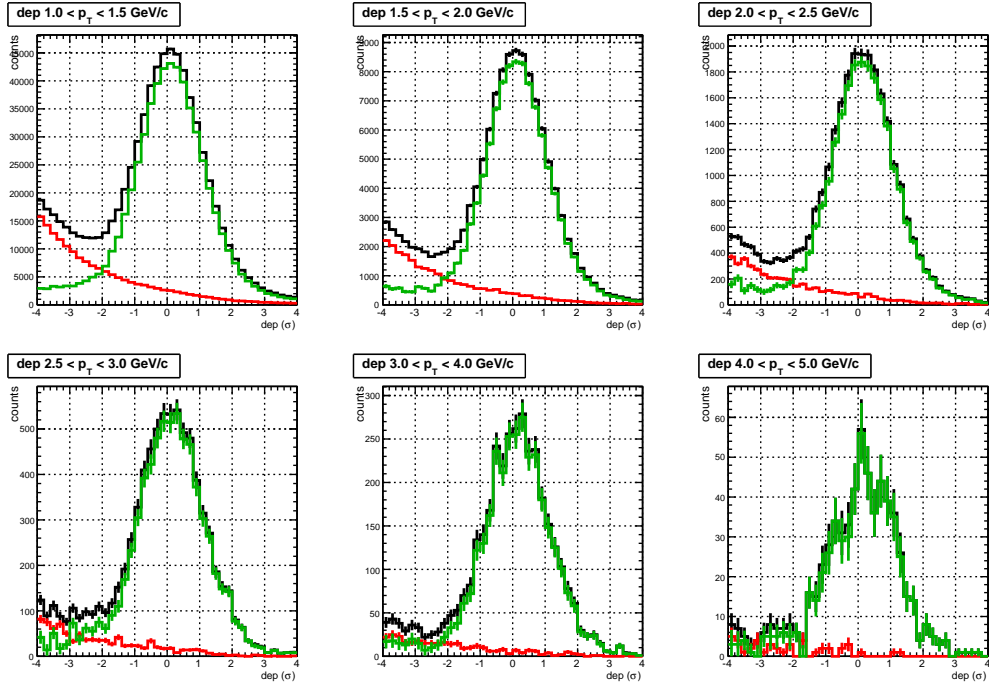
Figure 5.2: Matching variable between the reconstructed track momentum (p) and the energy measured in the EMCal (E): $dep = (E/p - \mu_{E/p})/\sigma_{E/p}$ in 5 p_T bins. The black distribution is for identified electrons , the red distribution is the estimated contribution from mis-identified electrons via the RICH swap-method, and the green distribution is for electrons after the subtraction of mis-identified electrons.

5.4 Event reconstruction in VTX

5.4.1 VTX alignment

In order to achieve good DCA resolution to separate $b \to e$ and $c \to e$, alignment of the detector ladders to high precision is required. The detector alignment is accomplished via an iterative procedure of matching outer central arm tracks from the DCH and PC to the VTX hits. (See appendix B for more detail.) The procedure is convergent for the position of each ladder. The alignment was repeated each time the detector was repositioned following a service access. The final alignment contribution to the DCA resolution in both ϕ and z is a few tens of microns.

5.4.2 VTX hit reconstruction

For layers B0 and B1, clusters of hit pixels are formed by connecting contiguous hit pixels by a recursive clustering algorithm. An average cluster size is 2.6 (6.7) pixels for the pixel (stripixel). The center of the cluster in the local 2-D coordinate system of the sensor is calculated as the hit position.

For B2 and B3 layers, 2D hit points on the sensor are reconstructed from the X-view and the U-view. Hit lines in the X-view (U-view) are formed by clustering contiguous hit X-strips (U-strips) weighted by deposited charges, and then 2D hit points are formed as the intersections of all hit lines in X- and U- views. When one hit line in U-view crosses more than two hit lines in X-view, ghost hits can be formed, because which crossing point is the true hit is ambiguous. These ghost hits increase the number of reconstructed 2D hits approximately by 50% (30%) in B2 (B3) in central Au+Au collisions. The ghost hit rate was studied using a full GEANT simulation with the HIJING [155] generator as input. However, because the occupancy of the detector at the reconstructed 2D hit point level is low, less than 0.1%, these ghost hits do not cause any significant issue in the analysis.

The positions of all 2-D hits in the VTX are then transferred into the global PHENIX 3-D coordinate system. Correction of the sensor position and orientation, determined by the alignment procedure described in the previous section, is applied in the coordinate transformation. The resulting 3-D hit positions in the global coordinate system are then used in the subsequent analysis.

5.4.3 The primary vertex reconstruction

With the VTX hit information alone, charged particle tracks can be reconstructed only with modest momentum resolution $\delta p/p \approx 10\%$ due to the limited magnetic field integrated over the VTX volume and the multiple scattering within the VTX. These tracks can be utilized to determine the collision vertex in three-dimensions (z_0 along the beam axis, and x_0,y_0 in the transverse plane) for each Au+Au event under the safe assumption that the majority of particles originate at the collision vertex. This vertex position is called the primary vertex position.

The position resolution of the primary vertex for each direction depends on the sensor pixel and strip sizes, the precision of the detector alignment, and the number of particles used for the primary vertex calculation and their momentum in each event. The primary vertex resolution is evaluated from the difference in the primary vertex calculated from by the EAST and WEST VTX barrels. The distributions for the EAST - WEST difference in x, y and z-axis is shown in Figure 5.3. The width of the distributions of the East - West difference is larger than the resolution of the primary vertex calculated using the full VTX by roughly a factor of 2. A factor of $1/\sqrt{2}$ comes from the assumption the multiplicity of East/West VTX is half of full VTX, another factor of $1/\sqrt{2}$ comes from the error propagation of East-West. Namely,

$$\sigma(\text{East}) = \sigma(\text{West}) = \frac{1}{\sqrt{2}}\sigma(\text{full VTX}),$$

$$\sigma(\text{East - West}) = \sqrt{\sigma(\text{East})^2 + \sigma(\text{West})^2} = 2 \times \sigma(\text{full VTX})$$

For Minimum Bias (MB) Au+Au collisions, the resolution values are $\sigma_x = 96~\mu$m, $\sigma_y = 43~\mu$m, and $\sigma_z = 75~\mu$m. The worse resolution in x compared to y is due to the orientation of the two VTX arms. For comparison, the beam profile in the transverse plane is $\sigma_x^{\text{lumi}} \approx \sigma_y^{\text{lumi}} \approx 90~\mu$m in the 2011 Au+Au run.

5.4.4 Association of a central arm track with VTX

Each central arm track is projected from the DCH through the magnetic field to the VTX detector. Hits in VTX are then associated with the track using a recursive windowing algorithm as follows.

The association starts from layer B3. VTX hits in that layer that are within a certain $(\Delta\phi \times \Delta z)$ window around the track projection are searched. If hits are found in this window, the track is connected to each of the found hits, and then projected inward to the next layer. In this case the search
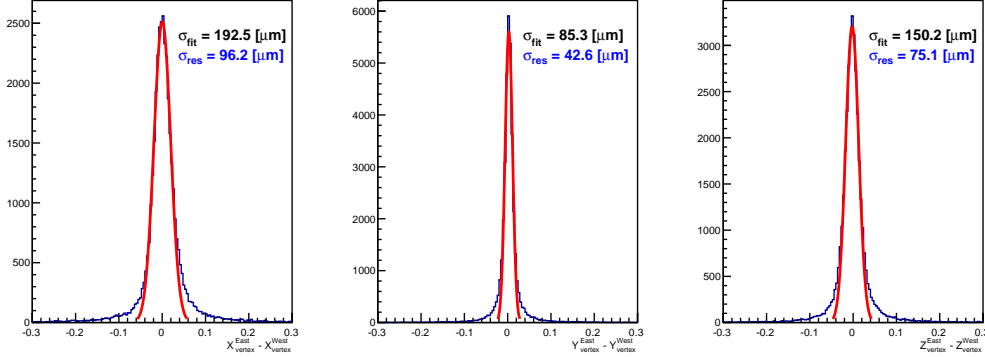
Figure 5.3: The distributions for the difference in the primary vertex calculated from by the East and West VTX barrels (East - West) in x, y and z-axis

window in the next layer is decreased, because there is much less uncertainty in projection to the next layer. If no hit is found, the layer is skipped, and the track is projected inward to the next layer, keeping the size of the projection window. This process continues until the track reaches layer B0, and a chain of VTX hits that can be associated with the track is formed. The window sizes are momentum dependent and determined from a full GEANT3 [154] simulation of the detector so that the inefficiency of track reconstruction due to the window size is negligible.

After all possible chains of VTX hits that can be associated with a given central arm track are found by the recursive algorithm, a track model fit (multi-helices) is performed for each of these possible chains as shown in Figure 5.4 and Figure 5.5 and the χ^2 of the fit, χ^2_{vtx}, is calculated. The effect of multiple scattering in each VTX layer is taken into account in calculation of χ^2_{vtx} This best chain and its track model are called a VTX-associated track. Note that at most one VTX-associated track is formed from each central arm track.

The detail of the calculation of χ^2_{vtx} is as follows:

$$\chi^2_{\text{vtx}} = \sum_{i=0}^{n-1} \left(\frac{\Delta\phi_i^2}{\sigma_{\phi,i}^2} + \frac{\Delta z_i^2}{\sigma_{z,i}^2} \right)$$
$$+ \sum_{i=1}^{n-2} \left(\frac{\Delta\theta_{xy,i}^2}{\sigma_{\theta_{xy},i}^2} + \frac{\Delta\theta_{rz,i}^2}{\sigma_{\theta_{rz},i}^2} \right) + \frac{\Delta\theta_{xy,n-1}^2}{\sigma_{\theta_{xy},n-1}^2 + \sigma_{\text{phi0}}^2} + \frac{\Delta\theta_{rz,n-1}^2}{\sigma_{\theta_{rz},n-1}^2 + \sigma_{\text{the0}}^2}$$

where

73

- $\Delta\phi_i$ (Δz_i): the difference of the hit position and the projected position of hit in azimuthal (z) direction.

- $\Delta\theta_{xy,i}$ ($\Delta\theta_{rz,i}$): the angle difference of the incoming and the outgoing helices in x-y (r-z) plane.

All the indices, i, correspond to indices of the associated hits. The counting begins from the innermost hit, i.e. 1st (($n-1$)-th) hit is the innermost (outermost) hit. $\sigma_{\phi,i}$ and $\sigma_{z,i}$ are resolution of each pixel: $\sigma_{\phi,0}(\sigma_{\phi,1}) = 14\ \mu$m and $\sigma_{z,0}(\sigma_{z,1}) = 123\ \mu$m, $\sigma_{\phi,2}(\sigma_{\phi,3}) = 23\ \mu$m and $\sigma_{z,2}(\sigma_{z,3}) = 289\ \mu$m. $\sigma_{\theta_{xy,i}}$ and $\sigma_{\theta_{rz,i}}$ is the root mean square of the Gaussian approximation of the multiple scattering angle divided by $\sqrt{2}$. The radiation length of each layer is averaged and corrected by a path length in modules of each track. σ_{phi0} and σ_{the0} correspond to the resolution of the azimuthal and polar angles of a track outside of the VTX, respectively. σ_{phi0} is calculated to be 1 mrad from the position resolutions of X1 and X2 of the DCH and the distance between X1 and X2 plane. σ_{the0} is calculated to be 7 mrad from the resolution of z coordinate measured by the PC1 and BBC [156]. The primary vertex position is not used for the χ^2_{vtx} calculation to avoid any bias on the long lived particle.

In this analysis we require that VTX-associated tracks have associated hits in at least the first three layers, i.e. B0, B1, and B2. An additional track requirement is $\chi^2_{\mathrm{vtx}}/\mathrm{NDF} < 2$ for $p_T < 2$ GeV/c and $\chi^2_{\mathrm{vtx}}/\mathrm{NDF} < 3$ for $p_T > 2$ GeV/c, where NDF is the number of degrees of freedom in the track fit, namely

$$NDF = 2 \cdot N_{hit} - 2,$$

where N_{hit} is the number of associated hits on the VTX.
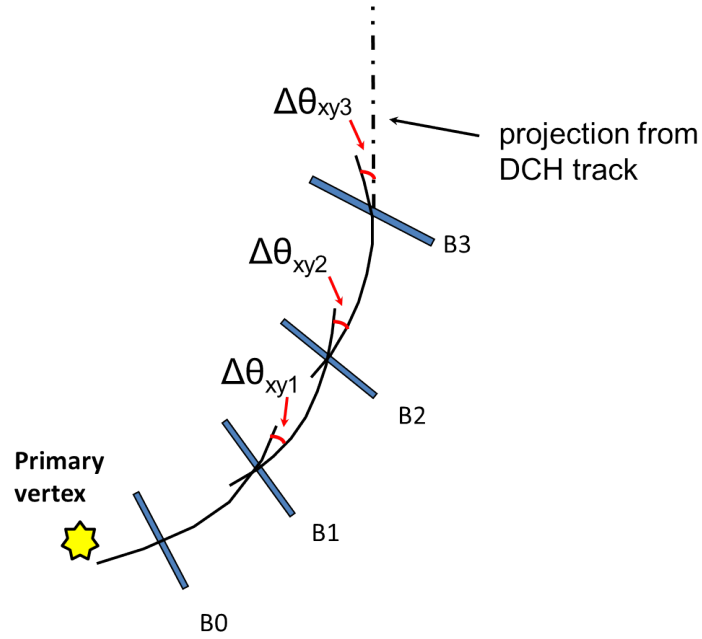
Figure 5.4: An illustration of a tracking with the VTX in x-y plane.
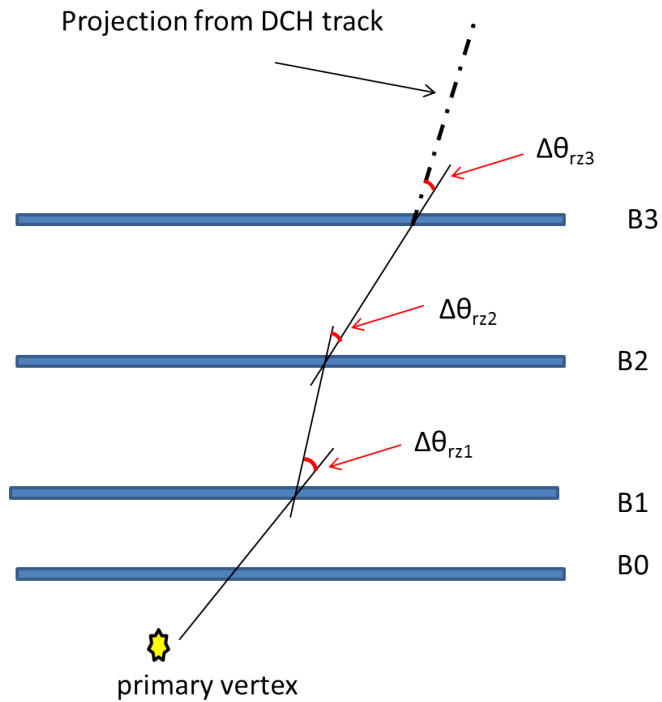
Figure 5.5: An illustration of a tracking with the VTX in r-z plane.

5.5 Event selection

The data set presented in this analysis is from Au+Au collisions at $\sqrt{s_{NN}} = 200$ GeV recorded in 2011 after the commissioning of the VTX detector. As detailed earlier, the MB Au+Au data sample was recorded using the BBC trigger sampling $96 \pm 3\%$ of the inelastic Au+Au cross section. A number of offline cuts were applied for optimizing the detector acceptance uniformity and data quality as described below. After all cuts, a data sample of 2.4×10^9 Au+Au events was analyzed.

5.5.1 z-vertex selection

The acceptance of the PHENIX central arm spectrometers covers collisions with z-vertex within $\pm$ 30 cm of the nominal interaction point. The VTX detector is more restricted in $|z|$ acceptance, as the B0 and B1 layers cover only $|z| < 11.4$ cm. Thus the BBC trigger selected only events within the narrower vertex range of $|z_{\mathrm{BBC}}| < 12$ cm. In the offline reconstruction, the tracks reconstructed from VTX information alone are used to reconstruct the Au+Au collision vertex with resolution $\sigma_z = 75$ μm. All Au+Au events in the analysis are required to have a z-vertex within ± 10 cm as reconstructed by the VTX.

5.5.2 Data quality assurance

Due to a number of detector commissioning issues in this first data taking period for the VTX, the data quality varies substantially. Therefore we divide the entire 2011 Au+Au data taking period into four periods. The acceptance of the detector changes significantly between these periods.

In addition, several cuts are applied to ensure the quality and the stability of the data. Applying electron identification cuts described in section 5.3, the electron to hadron ratios were checked for each run, a continuous data taking period typically lasting of order one hour, and three runs out of 547 with ratios outside of 5σ from the mean were discarded. The B2 and B3 stripixel layers had an issue in stability of read-out electronics where some of the sensor modules would drop out, resulting in a reduced acceptance within a given run. Additional instabilities also existed in the B0 and B1 pixel layers. Detailed channel by channel maps characterizing dead, hot, and unstable channels were generated for all layers within a given run. These maps were used to mask dead, hot, and unstable channels from the analysis, as well as to define the fiducial area of the VTX in simulations.

During this first year of data taking, the instability of the read-out electronics discussed above caused significant run-to-run variations in the acceptance and efficiency of the detector. It is therefore not possible to reliably calculate the absolute acceptance and efficiency correction while maintaining a large fraction of the total data set statistics. Instead, we report on the relative yields of charm and bottom to total heavy flavor. The DCA distributions have been checked consistent between running periods and are not impacted by the changing acceptance. Thus we can measure the shape of the DCA distribution using the entire data set. In the following, we use the shape of the measured DCA distribution only to separate $b \to e$ and $c \to e$ components.

5.6 DCA measurement with the VTX

Charged particle tracks reconstructed in the central arms must be associated with VTX hits in order to calculate their DCA. Three-dimensional (3-D) hit positions in the 4 layers of VTX are reconstructed. For each collision, the primary vertex is reconstructed by the VTX. Then central arm tracks are associated with hits in the VTX, and VTX-associated tracks are formed. Finally, the DCA between the primary vertex and the VTX-associated tracks are measured.

5.6.1 DCA_T and DCA_L

Using the primary vertex position determined above, the DCA of a track is calculated separately in the transverse plane (DCA_T) and along the beam axis (DCA_L). Because by design the DCA_T has a better resolution than DCA_L, we first find DCA_T with a track model of a circle trajectory assuming the uniform magnetic field over the VTX. We define DCA_T as

$$DCA_T \equiv L - R, \tag{5.1}$$

where L is the distance from the collision vertex to the center of the circle defining the particle trajectory, and R is the radius of the circle as shown in Figure 5.6. DCA_L is the distance between the z-coordinate of the point DCA_T found and z-coordinate of the primary vertex. As explained in the subsection 5.4.4, we always require a hit in layer B0. The projection is always started from the hit position in B0.

It is notable that DCA_T has a sign in this definition. The distinction between positive and negative values of DCA_T—whether the trajectory is bending towards or away from the primary vertex—is useful since certain background contributions have asymmetric distributions in positive and negative DCA_T, as discussed in section 5.7. For electrons, the positive side of DCA_T distribution has less background contribution. There is no such positive/negative asymmetry in DCA_L.

5.6.2 DCA distribution of hadron tracks

For each VTX-associated track, the DCA is calculated separately in the radial and longitudinal direction (DCA_T and DCA_L) from the track model and the primary vertex position. Shown in Figure 5.7 is the resulting DCA_T and DCA_L distributions for all VTX-associated tracks with $p_T = 1.0 - 5.0 \, \text{GeV}/c$. Since the vast majority of charged tracks are hadrons originating at the primary vertex, we observe a large peak around DCA_T, $DCA_L = 0$
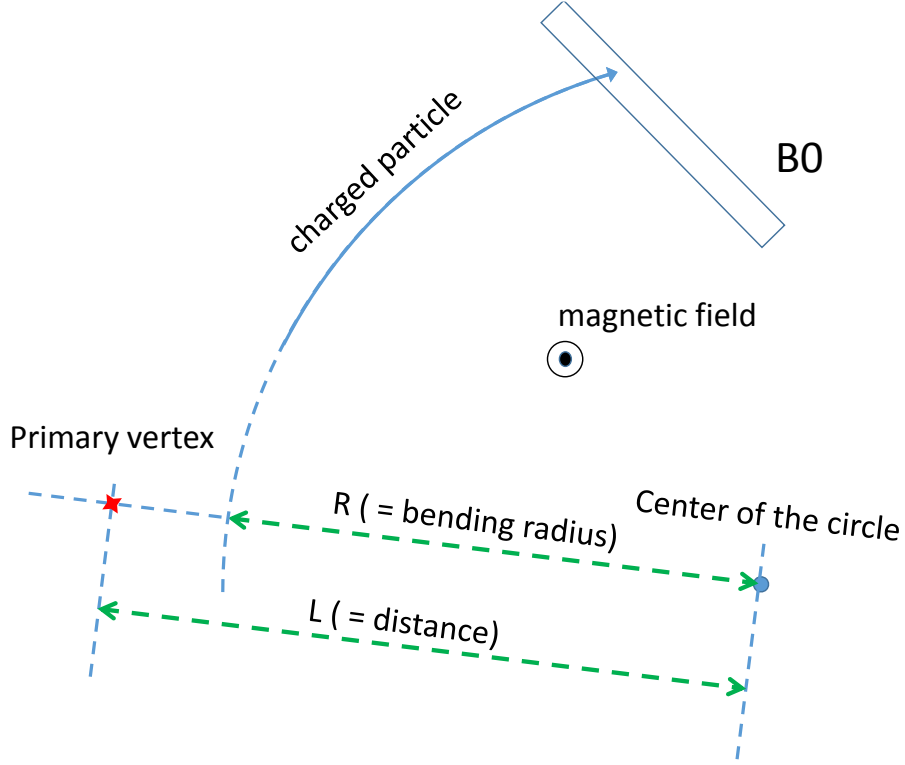
Figure 5.6: Illustration of the definition of $\mathrm{DCA}_T \equiv L$ - R in the transverse plane.

that is well fit to a Gaussian distribution where the σ represents the DCA_T, DCA_L resolution. A selection of $|\mathrm{DCA}_L| < 0.1$ cm is applied to reduce background. These DCA distributions are in integer-value counts and are not corrected for acceptance and efficiency. There are broad tails for $|\mathrm{DCA}_T| > 0.03$ cm. Monte Carlo simulation shows that the main source of the broad tails is the decay of long lived light hadrons such as Λ and K_S^0.

The DCA_T resolution as a function of the track p_T is extracted using a Gaussian fit to the peak and is shown in Figure 5.8. The DCA_T resolution is approximately 75 μm for the $1.0 - 1.5$ GeV/c bin and decreases with increasing p_T as the effect of multiple scattering becomes smaller for higher p_T. The DCA_T resolution becomes less than 60 μm for $p_T > 4$ GeV/c, where it is limited by the position resolution of the primary vertex.
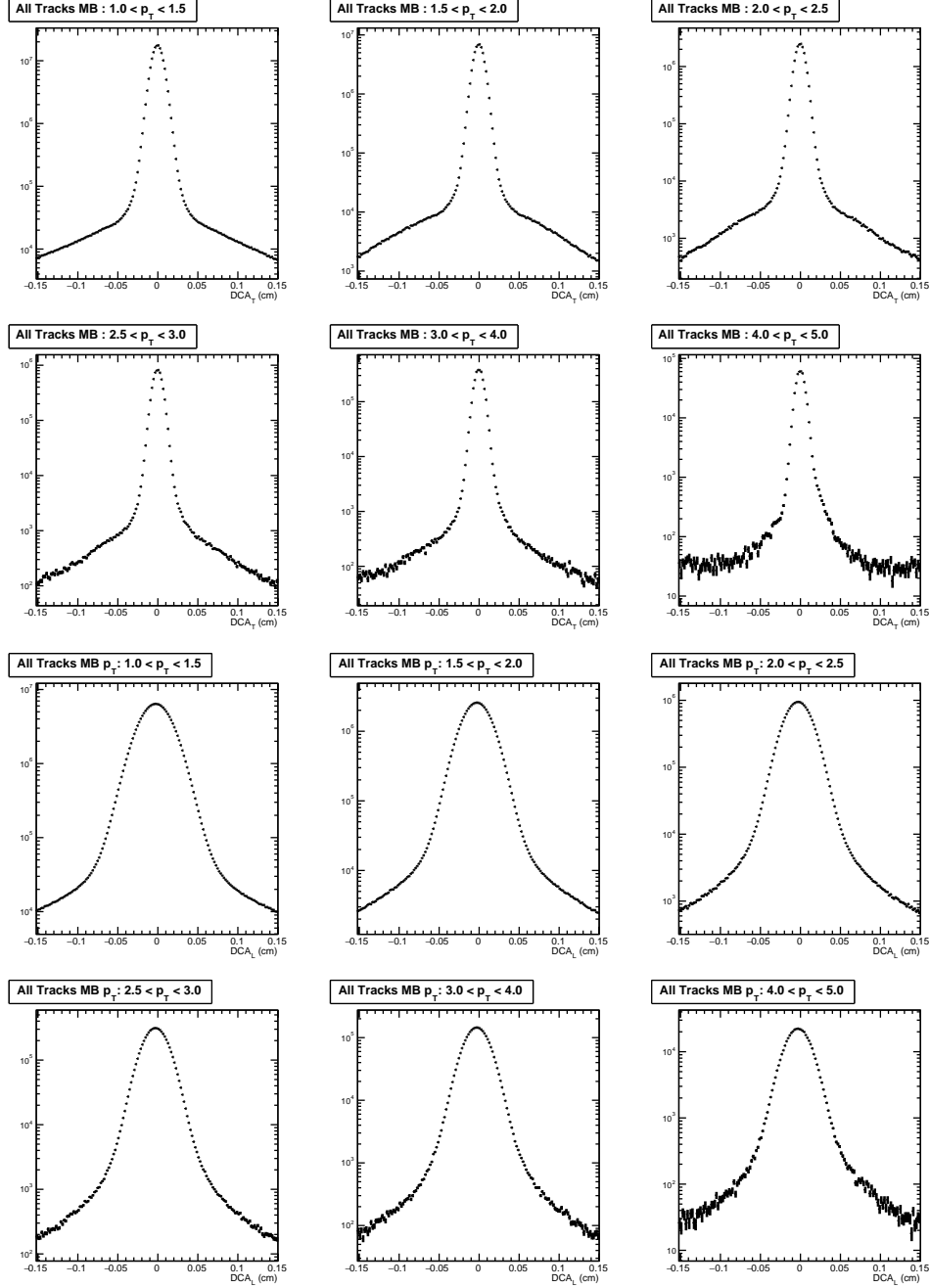
Figure 5.7: (Top 6 figures) Distance of closest approach distributions for transverse plane (DCA_T) and (Bottom 6 figures) along the beam axis (DCA_L) for all VTX-associated tracks in minimum bias Au+Au at $\sqrt{s_{NN}} = 200$ GeV in the range $1.0 < p_T < 5.0 \mathrm{GeV}/c$.
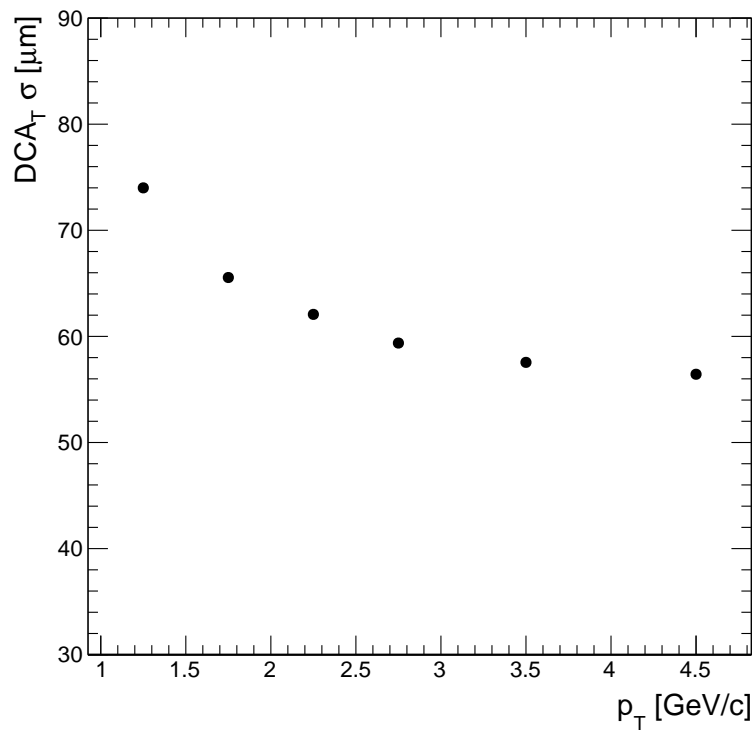
Figure 5.8:   The DCA$_T$ resolution as a function of p_T for all tracks in MB events

5.7 Electron DCA distribution and Background Components

5.7.1 Overview

The sample of candidate electron tracks that pass all the analysis cuts described above contains contributions from a number of sources other than the desired electrons from semi-leptonic decays of charm and bottom hadrons. In order to extract the heavy flavor contributions, all background components must be fully accounted for and their DCA_T shapes as a function of p_T incorporated. These background components are listed in the order presented below.

1. Misidentified hadrons

2. High-multiplicity background

3. Photonic electrons

4. Kaon decay electrons

5. Heavy-quarkonia decay electrons

As described in this and the following subsection, all background components are constrained by PHENIX measurements in Au+Au and are fully simulated through a GEANT3 description of the detector. This method is similar to the cocktail method of background subtraction used in the previous analysis of inclusive heavy flavor electrons [11].

Next, we describe these background sources and their DCA distributions. The first two components are caused by detector and multiplicity effects. DCA distributions and normalization of these two components are determined by data driven methods, as detailed in this section. The last three components are background electrons that are not the result of semi-leptonic decays of heavy flavor hadrons. Their DCA distributions are determined by Monte Carlo simulation, and their normalization is determined by a bootstrap method described in section 5.8. Of those background electrons, photonic electrons are the dominant contribution. We developed a conversion veto cut to suppress this background (5.7.4).

5.7.2 Mis-identified hadron

As detailed in the discussion on electron identification, there is a nonzero contribution from mis-identified electrons. This contribution is modeled via

82

the RICH swap-method described in Section 5.3. From this swap method, we obtain the probability that a charged hadron is mis-identified as an electron as a function of p_T. This probability is then applied to the DCA distribution of charged hadrons to obtain the DCA distribution of mis-identified hadrons.

The resulting DCA_T distribution is shown in each panel of Figure 5.13. Note that this component is properly normalized automatically. For each p_T bin, the DCA distribution of mis-identified prompt hadrons has a narrow Gaussian peak at $DCA_T = 0$. The broad tails for large $|DCA_T|$ are mainly caused by decays of Λ and K_S^0. In all p_T bins the magnitude of this background is no more than 10% of the data for all DCA_T

5.7.3   High-multiplicity background

Due to the high multiplicity in Au+Au collisions, an electron candidate track in the central arms can be associated with random VTX hits. Such random associations can cause a background that has a very broad DCA_T distribution. Although the total yield of this background is only $\simeq 0.1\%$ of the data, its contribution is significant at large DCA_T where we separate $b \rightarrow e$ and $c \rightarrow e$.

To evaluate the effect of event multiplicity on the reconstruction performance, we embed simulated single electrons—*i.e.* the response of the PHENIX detector to single electrons that is obtained from a GEANT3 simulation—into data events containing VTX detector hits from real Au+Au collisions. The events are then processed through the standard reconstruction software to evaluate the reconstruction performance in MB Au+Au collisions.

The reconstructed DCA_T and DCA_L for embedded primary electrons in MB Au+Au collisions is shown in Fig. 5.9. Here the histograms, labeled as "Single Electrons", show the reconstructed DCA_T and DCA_L distributions of primary electrons before embedding. The DCA_T distribution comprises a narrow Gaussian with no large DCA_T tail and the DCA_L distribution comprises a similar, but slightly broader, Gaussian with no large tail. The blue filled triangles show the DCA_T and DCA_L distributions after embedding. The DCA_T and DCA_L distributions comprise a Gaussian peaked at $DCA_T(DCA_L) \sim 0$ which is consistent with the distribution before embedding. This demonstrates that the DCA resolution of the VTX is not affected by the high multiplicity environment. However, the embedded distributions have broad tails at large $|DCA_T|$ and $|DCA_L|$.

As shown in Figure 5.9(b), tracks with $|DCA_L| > 0.13$ cm are dominated by random associations, as they are not present in the "Single Electron" sample. We therefore use the DCA_T distribution for tracks with large $|DCA_L|$ as an estimate of this random high-multiplicity background. We choose the

region $0.13 < |\text{DCA}_L|$ cm < 0.18 to represent this background, and restrict our signal to $|\text{DCA}_L| < 0.1$ cm. The DCA_T distribution of tracks with $0.13 < |\text{DCA}_L|$ cm < 0.18 must be normalized in order to be used as an estimate of the high-multiplicity background for tracks within $|\text{DCA}_L| < 0.1$ cm. This normalization is determined by matching the integrated yield of embedded primary electrons in each $|\text{DCA}_L|$ region for $0.08 < \text{DCA}_T$ cm < 0.2, as shown in the inlay of Figure 5.9(b). The region $0.08 < \text{DCA}_T$ cm < 0.2 is dominated by random associations, as shown in Fig. 5.9(a), and is therefore safe to use for determining the normalization. The normalization of the high-multiplicity background is determined to be 2.89 ± 0.29. The red filled circles in Fig. 5.9(a) show the embedded DCA_T distribution with large DCA_L ($0.13 < |\text{DCA}_L|$ cm < 0.18). This distribution agrees with the embedded DCA_T distribution (blue filled triangles in Fig. 5.9) for large DCA_T. This demonstrates that the tails for large DCA_T are well normalized by the distribution of electrons with large DCA_L. However, there is a small excess in the region $0.05 < |\text{DCA}_T|$ cm < 0.10 that is not accounted for by the distribution with large DCA_L. We address this excess in the systematic uncertainties, as described in section. 5.10, where it is found to have only a small effect on the extraction of $b \to e$ and $c \to e$.

In each panel of Figure 5.13 the high-multiplicity background is shown as a red line. It is determined from the DCA_T distribution of the data within $0.13 < |\text{DCA}_L|$ cm < 0.18, as described above. The number of electron tracks in the large DCA_L region is small. We therefore fit the resulting DCA_T data in each p_T bin with a smooth function to obtain the shape of the red curves shown in Figure 5.13. A second order polynomial is used in the lowest p_T bin, where there are enough statistics to constrain it. The higher p_T bins are fit with a constant value. All curves are multiplied by the same normalization factor, determined from embedded simulations as described above.
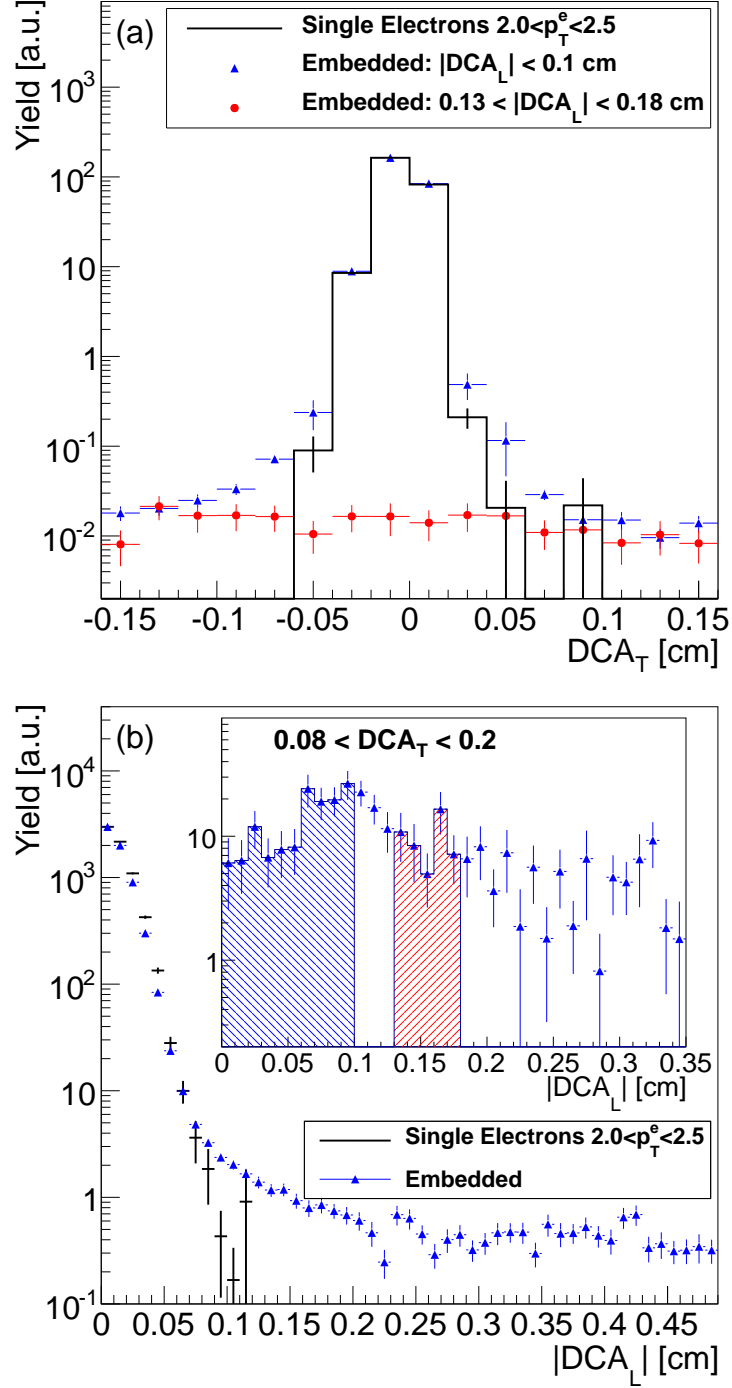
Figure 5.9: Simulated primary electron (a) DCA_T and (b) DCA_L distribution before and after embedding in real Au+Au data.

5.7.4 Photonic electrons and conversion veto cut

Photon conversions and Dalitz decays of light neutral mesons (π^0 and η) are the largest electron background. We refer to this background as photonic electron background as it is produced by external or internal conversion of photons.

The PHENIX Collaboration has previously published the yields of π^0 and η mesons in Au+Au collisions at $\sqrt{s_{NN}} = 200$ GeV [157, 158]. In addition to the electrons from Dalitz decays of these mesons, the decay photons may convert to an e^+e^- pair in the detector material in the beam pipe or each layer of the VTX. The PHENIX Collaboration has also published the yields of direct photons in Au+Au collisions at $\sqrt{s_{NN}} = 200$ GeV [20, 69], that can also be a source for conversions.

In principle with these measured yields, combined with simple decay kinematics and a detailed GEANT3 description of the detector material and reconstruction algorithm, one could fully account for these photonic electron contributions as a function of DCA_T and p_T. However, systematic uncertainties on the measured yields for the π^0, η, and direct photons would then dominate the uncertainty of the heavy flavor electron extraction. Therefore, we utilize the VTX detector itself to help reject these contributions in a controlled manner.

We require that at least the first three layers of the VTX have hits associated with the electron track. Conversions in B1 and subsequent layers are rejected by the requirement of a B0 hit, leaving only conversions in B0 and the beam pipe. The requirement of B1 and B2 hits enables us to impose a conversion veto cut, described below, that suppresses conversions from the beam pipe and B0.

The conversion veto cut rejects tracks with another VTX hit within a certain window in $\Delta\phi$ and Δz around hits associated with a VTX-associated track. Photons that convert to an e^+e^- pair in the beam pipe will leave two nearby hits in the first layer (B0) and/or subsequent layers of the VTX, and thus be rejected by the conversion veto cut. Similarly, conversions in B0 will result in two nearby hits in the second layer (B1) and/or subsequent outer layers. The same is true for e^+e^- from a Dalitz decay, though with a larger separation due to a larger opening angle of the pair.

Figure 5.10 shows distribution of $charge \times \Delta\phi$ of hits in each layer relative to the electron track, where $charge$ is the sign of charge of the track. The red histogram shows the data in MB Au+Au collisions. If the track at the origin is not an electron, we have a flat distribution due to random hits in the detector. These random hits have been subtracted in Figure 5.10 by using the distribution for hadron tracks. The transverse momentum of the electron

track is in the interval $1 < p_T < 2$ GeV/c .

As mentioned above, these correlated hits around electron tracks are caused by the partner e^+ or e^- of Dalitz decays or photon conversions. The left-right asymmetry of the distribution is caused by the fact that the partner $e^{\pm}$ track is separated from the electron track by the magnetic field and the direction of the separation is determined by the charge of the electron track. In the distribution of $charge \times \Delta\phi$, the partner track is bent towards the positive direction.

The black histogram in Figure 5.10 shows the distribution from Monte Carlo simulations. In the simulation, the response of the PHENIX detector to single π^0s is modeled by GEANT3, and the resulting hits in the VTX and the central arms are then reconstructed by the same reconstruction code as the data. The correlated hits in the simulation are caused by the Dalitz decay of π^0 and photon conversion in the material of the beam pipe and the VTX itself. The simulation reproduces the data well for $charge \times \Delta\phi > 0$. There is a difference between the data and the simulation for $charge \times \Delta\phi < 0$. This is caused by a subtle interplay between the conversions and high multiplicity effects. The difference disappears for peripheral collisions. Similar correlated hits are observed in B1 to B3 layers in the data and they are also well explained by the simulation.

We define a "window" of the conversion veto cut around an electron track in each layer B0 to B3 and require that there is no hit other than the hit associated with the electron track in the window. Since a photonic electron (Dalitz and conversion) tends to have a correlated hit in the window, as one can see in Figure 5.10, this conversion veto cut rejects photonic background. A larger window size can reject photonic background more effectively, but this can also reduce the efficiency for the heavy flavor electron signal due to random hits in the window. The window for the conversion veto cut is a compromise in terms of the rejection factor on photonic backgrounds and efficiency for heavy flavor electrons. We optimized the size of the window of the conversion veto cut based on a GEANT3 simulation.

The pink hatched area shown in Figure 5.11 shows the window of the conversion veto cut in each layer. The window size is asymmetric since correlated hits are mainly in the positive side of $charge \times \Delta\phi$. The window size is reduced for higher electron p_T since the distribution of correlated hits becomes narrower for higher p_T.
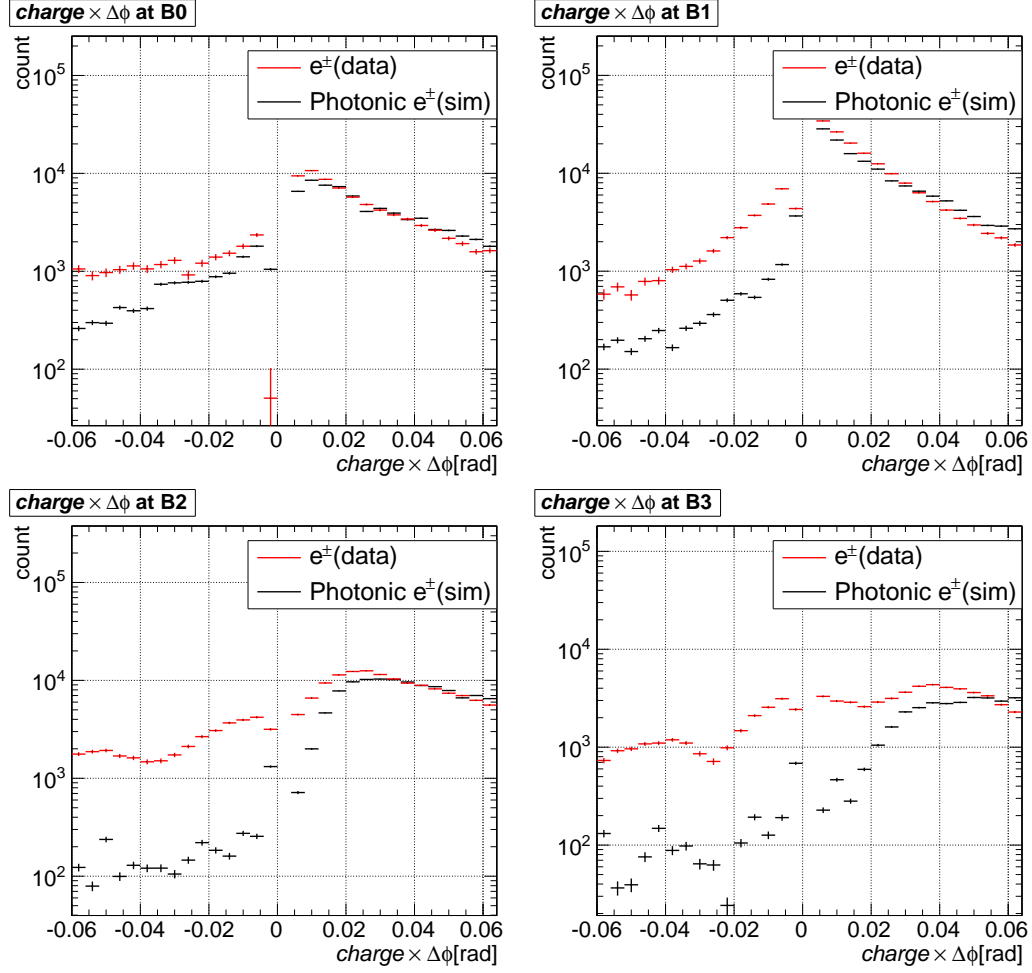
Figure 5.10:   Distribution of correlated hits near electron tracks for $1 < p_T < 2$ GeV.
Distribution of correlated hits in B0 (top-left), B1 (top-right), B2 (bottom-left), B3(bottom-right) near electron tracks for $1 < p_T < 2$ GeV. The red points are from Au+Au data and the black points are from Monte Carlo simulation.
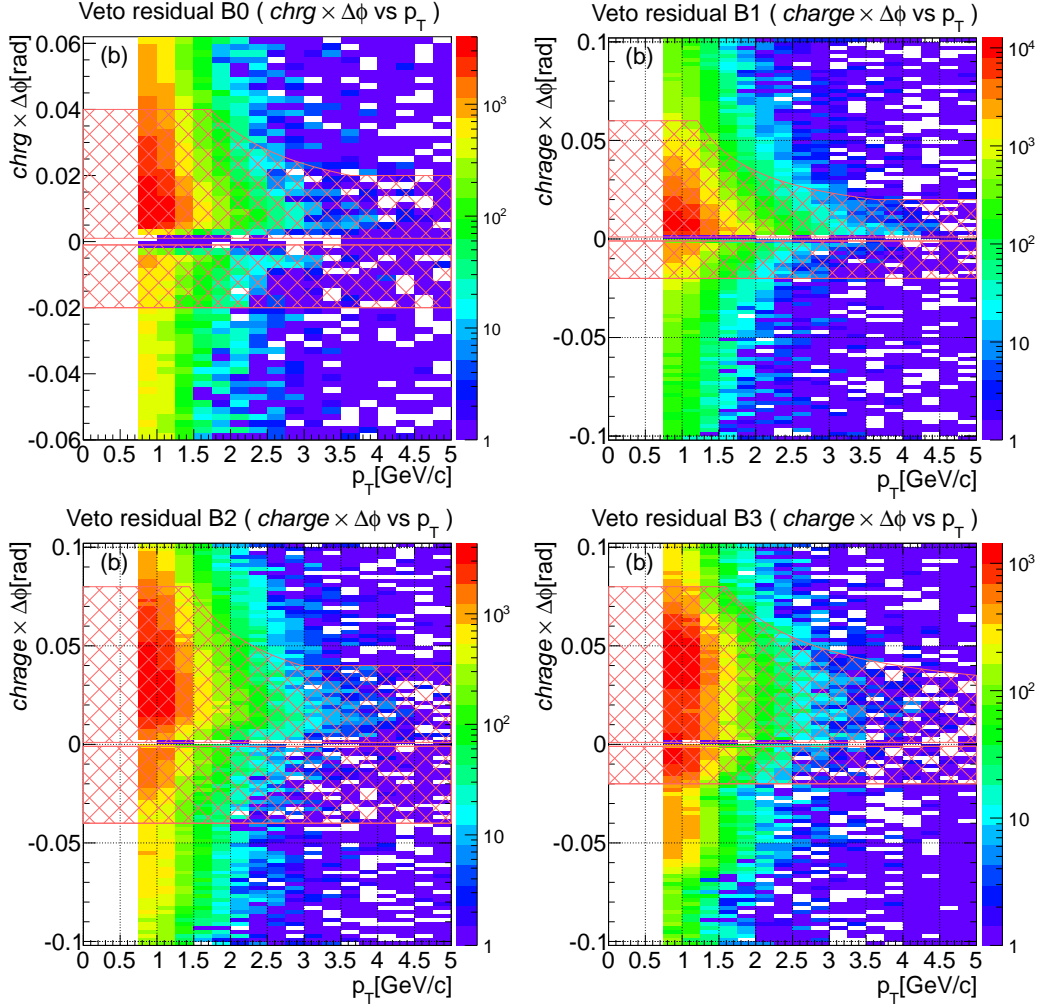
Figure 5.11: $charge \times \Delta\phi$ vs p_T for B0(top-left), B1(top-right), B2(bottom-left), B3(bottom-right). The conversion veto window is the pink hatched area.

Figure 5.12 shows the survival fraction of the conversion veto cut for electrons from photon conversions and Dalitz decays as a function of electron p_T from a GEANT3 simulation of the detector with hits run through the reconstruction software. The survival probability for conversions is less than 30% at $p_T = 1$ GeV and decreases further at higher p_T. The survival probability for Dalitz decays is higher since a Dalitz decay partner is more likely to fall outside of the window of the conversion veto cut due to the larger opening angle. Also shown in Figure 5.12 is the survival fraction of electrons from heavy flavor decays which pass the conversion veto cut (S_{HF}). As expected, their efficiency for passing the conversion veto cut is quite high and p_T independent.

The efficiencies shown in Figure 5.12 are calculated without the Au+Au high-multiplicity that may randomly provide a hit satisfying the conversion veto cut. Since these are random coincidences, they are a common reduction for all sources including the desired signal — heavy flavor electrons. This common reduction factor, δ_{random}, is measured from the reduction of the hadron track yield by the conversion veto cut to be $\simeq 35\%$ at $p_T = 1$ GeV to $\simeq$ 25% at $p_T = 5$ GeV for MB Au+Au collisions. Note that when we determine the DCA$_T$ distribution of the various background components using a full GEANT3 simulation we apply the same conversion veto cuts.

The DCA$_T$ distributions from photonic background processes that survive the conversion veto cut are shown in Figure 5.13. The means of the DCA$_T$ distributions from Dalitz decays and conversions are shifted to negative DCA$_T$ values due to the mis-reconstruction of the momentum caused by the assumption that the tracks originate at the primary vertex, as explained in the next paragraph. The shift is largest at the lowest p_T bin and decreases with increasing p_T.

For Dalitz electrons, the shift is due to the energy loss via induced radiation (bremsstrahlung). The total radiation length of the VTX is approximately 13% as shown in Table 4.3. Thus a Dalitz electron coming from the primary vertex loses approximately $1 - e^{-0.13} \approx 12\%$ of its energy on average when it passes through the VTX. The momentum measured by the DC is close to the one after the energy loss due to the reconstruction algorithm. Since the momentum determined by the DC is used when projecting inward from the hit in B0 to the primary vertex and in calculation of DCA$_T$, this results in a slight shift in the DCA$_T$ distribution. This effect is fully accounted for in the DCA$_T$ template of Dalitz electrons since it is generated through the full GEANT3 and reconstruction simulation.

In the case of conversions, the effect is even larger, as one can clearly see in Figure 5.13. While a photon goes straight from the primary vertex to the beam pipe or B0 layer where it converts, DCA$_T$ is calculated assuming that

the electron track is bent by the magnetic field. Thus the DCA_T distribution is shifted by the difference of the actual straight line trajectory and the calculated bent trajectory. Again, this is fully accounted for with the full GEANT3 simulation. The effect is verified by selecting conversion electrons with a reversed conversion veto cut.
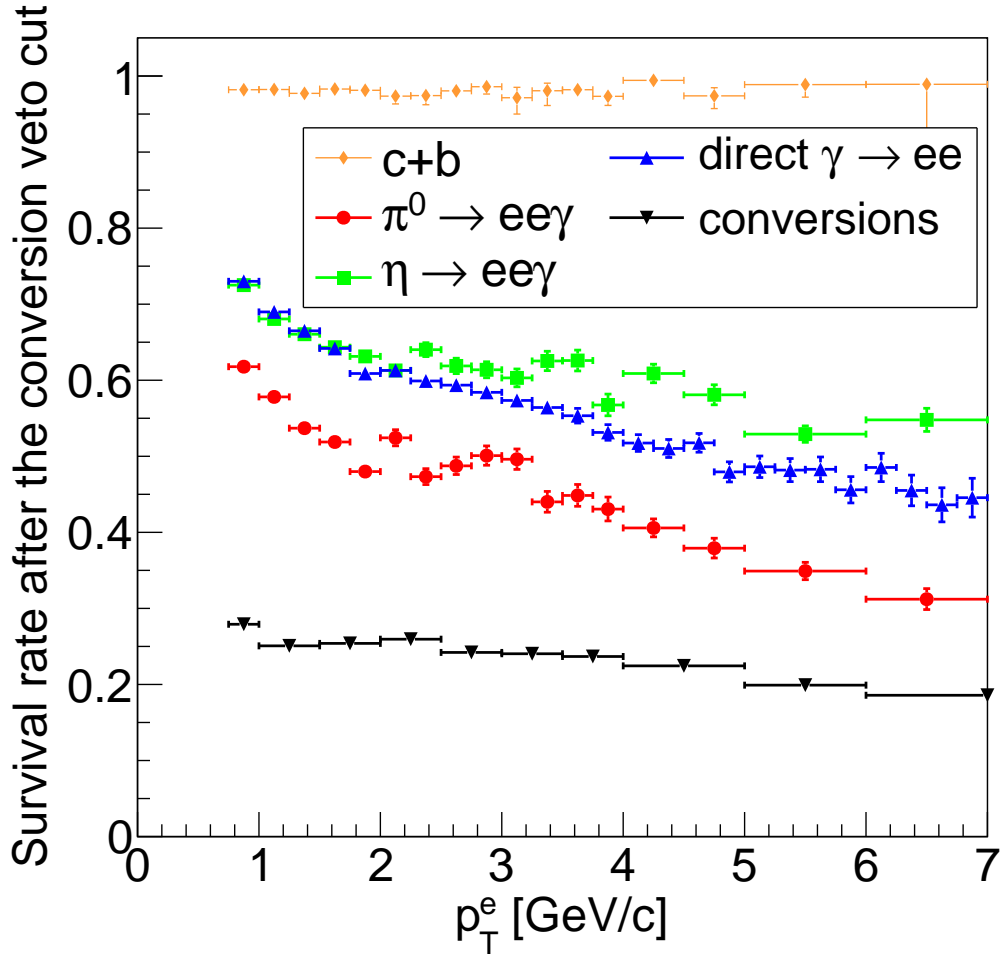
Figure 5.12:   The survival rate as a function of electron p_T (p_T^e) for electrons from photon conversion (black), Dalitz decay of π^0 (red), η (green), electrons from direct photon (blue) and heavy flavor decay electrons (dark orange).

5.7.5 K_{e3}

The background from K_{e3} decays (K_S^0, $K^\pm \to e\nu\pi$) contributes electrons over a broad range of DCA_T due to the long lifetime of the kaons. Both contributions are determined using PYTHIA and a full GEANT3 simulation, taking into account the exact track reconstruction, electron identification cuts, and conversion veto cut. The resulting DCA_T distribution for these kaon decays is shown in Figure 5.13. As expected, though the overall yield is small, this contributes at large DCA_T in the lower p_T bins and is negligible at higher p_T.

5.7.6 Quarkonia

Quarkonia (J/ψ and Υ) decay into electron pairs. Due to the short lifetime, these decays contribute to electrons emanating from the primary vertex. The J/ψ yields in Au+Au collisions at $\sqrt{s_{NN}} = 200$ GeV have been measured by the PHENIX Collaboration [159]. The detailed modeling of these contributions out to high p_T is detailed in Ref. [11]. While these measurements include a small fraction of $B \to J/\psi$ decays, all J/ψ's are considered prompt when modeling the DCA_T distribution. The J/ψ contribution is shown in Figure 5.13, and is quite small and peaked about $\text{DCA}_T = 0$ as expected. Thus, the systematic uncertainty from the quarkonium yields in Au+Au collisions is negligible in all electron DCA_T p_T bins.

5.8   Normalization of electron background components

If the detector performance were stable, we could convert the DCA_T distributions from counts into absolutely normalized yields. Then one could straightforwardly subtract the similarly absolutely normalized background contributions described above—with the normalization constrained by the previously published PHENIX yields for π^0 [157], η [160], etc. However, due to detector instability during the 2011 run, such absolute normalization of background contributions can have a large systematic uncertainty. Thus we bootstrap the relative normalization of these background contributions utilizing our published Au+Au results [11] from data taken in 2004.

The idea of the method is the following. PHENIX measured the invariant yield of open heavy flavor decay electrons from the 2004 dataset. In this 2004 analysis we first measured inclusive electrons (*i.e.* the sum of background electrons and heavy flavor electrons). We then determined and subtracted the background electron components from the inclusive electron yields to obtain the heavy flavor contribution. Thus the ratio of the background components to the heavy flavor contribution were determined and published in [11]. We use these ratios to determine the normalization of background components in the 2011 data, as described in the next paragraph. Some backgrounds have the same ratio to signal regardless of the year the data was collected, while others will differ due to the additional detector material added by the VTX.

The invariant yield in Au+Au collisions at $\sqrt{s_{NN}} = 200$ GeV of heavy flavor electrons and background electrons from Dalitz decays is a physical observable independent of the year the data was taken. Thus we can use the ratio of heavy flavor/Dalitz that is determined in the 2004 analysis in the 2011 data. On the other hand, the invariant yield of conversion electrons depends on the detector material present and is thus different in the 2011 data taking period with the VTX installed compared with the 2004 data. We account for this difference by calculating the fraction of nonphotonic electrons in the 2011 data. A detailed description of the normalization procedure is given in Appendix A.

With this bootstrapped normalization completed, the correctly normalized background components are shown for all five p_T bins vs DCA_T in Figure 5.13. Note that the normalization of mis-identified hadron and random background is determined from the data as explained in sections 5.7.2 and 5.7.3, respectively. The electron yield beyond the sum of these background components is from the combination of charm and bottom heavy flavor electrons.

While the DCA_T distributions in Figure 5.13 are plotted within $|DCA_T| <$ 0.15 cm, only a $|DCA_T| < 0.1$ cm is used in the analysis to extract the charm and bottom yield described later. At large DCA_T, the distribution is dominated by high-multiplicity background (subsection 5.7.3) and therefore provides little constraint in the extraction of the charm and bottom contributions.
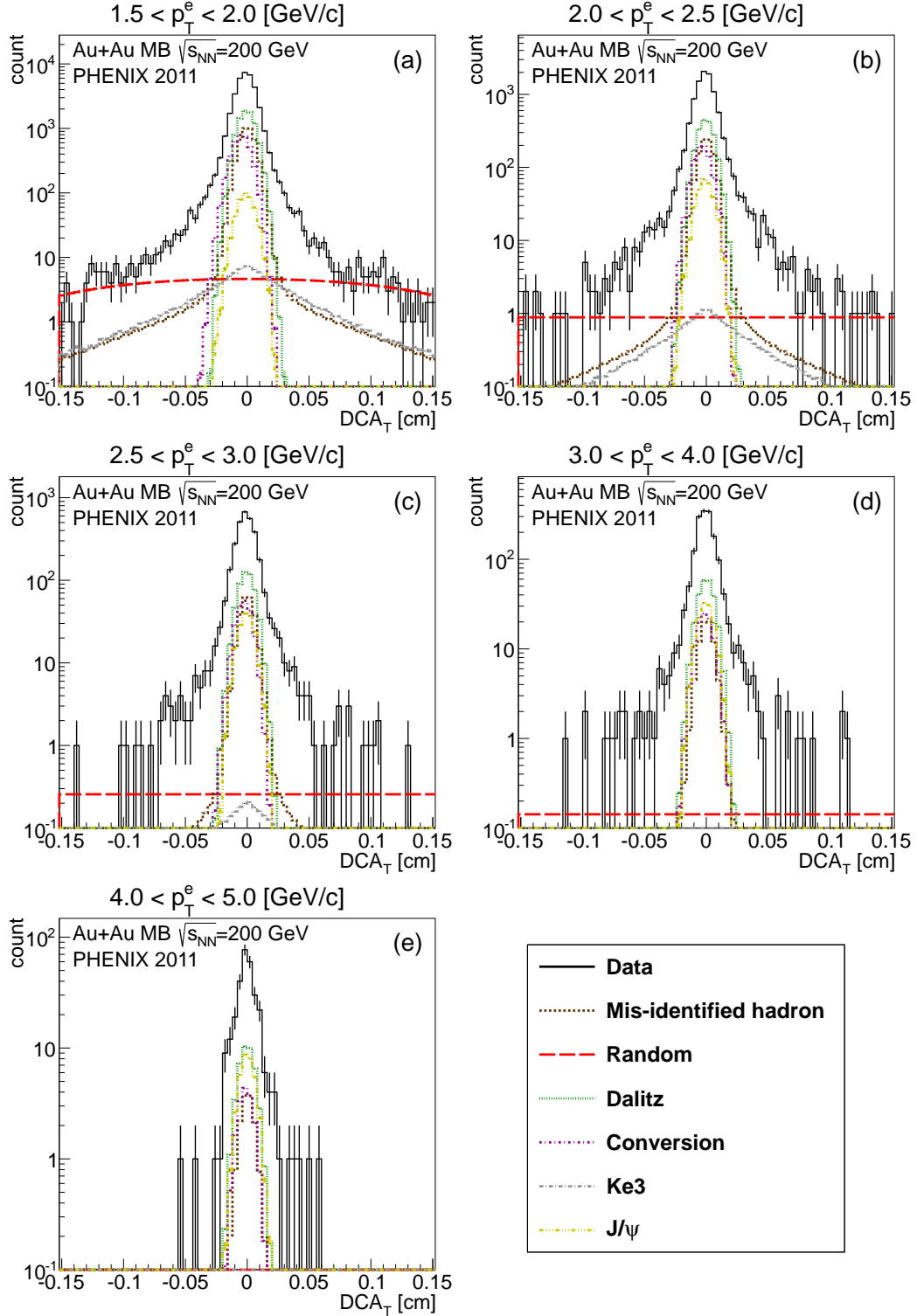
Figure 5.13: DCA_T distributions for electrons in MB Au+Au at $\sqrt{s_{NN}} = 200$ GeV that pass the reconstruction and conversion veto cut in the indicated five electron-p_T selections. Also shown are the normalized contributions for the various background components detailed in Section 5.7.

5.9 Unfolding

5.9.1 Overwiew

After we obtain the DCA_T distributions as a function of electron p_T and the various background components, we proceed to extract the remaining charm and bottom components. If one knew the shape of the parent charm and bottom hadron p_T and rapidity distributions, one could calculate in advance the DCA_T shape for electrons from each heavy flavor via a model of the decay kinematics. Since the decay lengths of charm and bottom hadrons are significantly different, they will yield different DCA_T distributions. In this case, one could simultaneously fit the DCA_T distribution for each p_T bin with all background components fixed across p_T bins, and extract the one free parameter: the ratio of charm to bottom contributions. However, the p_T distribution of charm hadrons is known to be significantly modified in Au+Au collisions — see for example Ref. [15]. For bottom hadrons this is also likely to be the case. Therefore one does not know *a priori* the heavy flavor DCA_T distribution since it depends on the parent p_T distribution. For example, a B meson with momentum $= 0$ has a daughter electron with DCA $= 0$ no matter what the electron momentum happens to be.

Since the DCA_T distributions for all electron p_T result from the same parent charm and bottom hadron p_T spectrum, one can perform a simultaneous fit to all the electron p_T and DCA_T data in order to find the most likely heavy flavor parent hadron p_T distributions. The estimation of a set of most likely model parameters using a simultaneous fit to data is often referred to as unfolding. Statistical inference techniques are often employed to solve such problems; see for example the extraction of reconstructed jet cross sections [161].

The DCA_T distributions are in counts and have not been corrected for the p_T-dependent reconstruction efficiency in Au+Au collisions, and therefore hold no yield information. To further constrain the extraction of the charm and bottom components, we include the total heavy flavor electron invariant yield as measured by PHENIX [11] in Au+Au collisions at $\sqrt{s_{NN}} = 200$ GeV with 2004 data set. This measurement is more accurate than currently available with the 2011 data set, where the VTX acceptance changes with time.

The unfolding procedure, using a particular sampling method (described in Section 5.9.2), chooses a set of trial charm and bottom parent hadron yields. The trial set of yields is multiplied by a decay matrix (described in Section 5.9.4), which encodes the probability for a hadron in a given p_T interval to decay to an electron at mid-rapidity as a function of electron p_T and DCA_T. The resulting distributions of electron p_T and DCA_T are

compared with the measured data using a likelihood function (described in Section 5.9.3). In order to dampen discontinuities and oscillatory behavior, a penalty upon the likelihood (described in Section 5.9.5) is added to enforce smoothness in the resulting hadron p_T distributions (regularization).

5.9.2 Unfolding method

Here we apply Bayesian inference techniques to the unfolding problem. A detailed introduction to these techniques is given in Ref. [162]. Bayesian unfolding techniques provides a joint probability density over the full set of model parameters. In this analysis, the vector of model parameters, $\boldsymbol{\theta}$, is the vector of parent charm and bottom hadron yields binned in p_T.

Given a vector of measured data, $\mathbf{x}$, and our vector of model parameters, $\boldsymbol{\theta}$, we use Bayes' theorem

$$p(\boldsymbol{\theta}|\mathbf{x}) = \frac{P(\mathbf{x}|\boldsymbol{\theta})\pi(\boldsymbol{\theta})}{P(\mathbf{x})}, \tag{5.2}$$

to compute the posterior probability density $p(\boldsymbol{\theta}|\mathbf{x})$ from the likelihood $P(\mathbf{x}|\boldsymbol{\theta})$ and prior information $\pi(\boldsymbol{\theta})$. The function $P(\mathbf{x}|\boldsymbol{\theta})$, quantifies the likelihood of observing the data given a vector of model parameters. In frequentist statistics, the $P(\mathbf{x}|\boldsymbol{\theta})$ is often used alone to determine the best set of model parameters. Bayesian inference, on the other hand, allows for the inclusion of the analyzer's *a priori* knowledge about the model parameters, as encoded in $\pi(\boldsymbol{\theta})$. The implementation of $\pi(\boldsymbol{\theta})$ used in this analysis is discussed in Section 5.9.5. The denominator $P(\mathbf{x})$ serves as an overall normalization of the combined likelihood $P(\mathbf{x}|\boldsymbol{\theta})\pi(\boldsymbol{\theta})$ such that $p(\boldsymbol{\theta}|\mathbf{x})$ can be interpreted as a probability density. In this analysis, $p(\boldsymbol{\theta}|\mathbf{x})$ gives the probability for a set of charm and bottom hadron yields,

$$\boldsymbol{\theta} = (\boldsymbol{\theta}_c; \boldsymbol{\theta}_b), \tag{5.3}$$

given the values of the measured electron data points $\mathbf{x}$. Since we are only interested in the parameters which maximize $p(\boldsymbol{\theta}|\mathbf{x})$, we can dispense with the calculation of $P(\mathbf{x})$, as it serves only as an overall normalization.

Here $\boldsymbol{\theta}$ comprises 17 bins of both charm and bottom hadron p_T, yielding a 34-dimensional space which must be sampled from in order to evaluate $p(\boldsymbol{\theta}|\mathbf{x})$. To accomplish this we employ a Markov Chain Monte Carlo (MCMC) algorithm to draw samples of $\boldsymbol{\theta}$ in proportion to $p(\boldsymbol{\theta}|\mathbf{x})$. This makes accurate sampling of multidimensional distributions far more efficient than uniform sampling. In implementation, it is in fact the right hand side of Eq. 5.2 that is sampled. The MCMC variant used here is an affine-invariant ensemble

sampler described in Ref. [163] and implemented as described in Ref. [164]. It is well suited to distributions that are highly anisotropic such as spectra which often vary over many orders of magnitude.

5.9.3 Modeling the likelihood function

This analysis is based on 21 data points of total heavy flavor electron invariant yield, $\mathbf{Y}^{\text{data}}$, in the range $1.0 - 9.0$ GeV/c from the 2004 data set [11], and five electron DCA_T distributions $\mathbf{D}_j^{\text{data}}$, where j indexes each electron p_T interval within the range $1.5 - 5.0$ GeV/c from the 2011 data set. Therefore,

$$\mathbf{x} = (\mathbf{Y}^{\text{data}}, \mathbf{D}_0^{\text{data}}, \mathbf{D}_1^{\text{data}}, \mathbf{D}_2^{\text{data}}, \mathbf{D}_3^{\text{data}}, \mathbf{D}_4^{\text{data}}) \tag{5.4}$$

in Eq. 5.2.

Our ultimate goal is to accurately approximate the posterior distribution over the parent hadron invariant yields $\boldsymbol{\theta}$ by sampling from it. For each trial set of hadron yields, the prediction in electron p_T, $\mathbf{Y}(\boldsymbol{\theta})$, and DCA_T, $\mathbf{D}_j(\boldsymbol{\theta})$, is calculated by

$$\begin{aligned} \mathbf{Y}(\boldsymbol{\theta}) &= \mathbf{M}^{(\mathbf{Y})}\boldsymbol{\theta}_c + \mathbf{M}^{(\mathbf{Y})}\boldsymbol{\theta}_b \tag{5.5} \\ \mathbf{D}_j(\boldsymbol{\theta}) &= \mathbf{M}_j^{(\mathbf{D})}\boldsymbol{\theta}_c + \mathbf{M}_j^{(\mathbf{D})}\boldsymbol{\theta}_b, \tag{5.6} \end{aligned}$$

where $\mathbf{M}^{(\mathbf{Y})}$ and $\mathbf{M}_j^{(\mathbf{D})}$ are decay matrices discussed in Section 5.9.4. We then evaluate the likelihood between the prediction and each measurement in the data sets $\mathbf{Y}^{\text{data}}$ and $\{\mathbf{D}_j^{\text{data}}\}_{j=0}^4$. As is customary, the logarithm of the likelihood function is used in practice. The combined log likelihood for the data is explicitly

$$\ln P(\mathbf{x}|\boldsymbol{\theta}) = \ln P(\mathbf{Y}^{\text{data}}|\mathbf{Y}(\boldsymbol{\theta})) + \sum_{j=1}^{5} \ln P(\mathbf{D}_j^{\text{data}}|\mathbf{D}_j(\boldsymbol{\theta})). \tag{5.7}$$

The $\mathbf{Y}^{\text{data}}$ dataset is assigned statistical uncertainties that are assumed to be normally distributed and uncorrelated. Thus, the likelihood $\ln P(\mathbf{Y}^{\text{data}}|\mathbf{Y}(\boldsymbol{\theta}))$ is modeled as a multivariate Gaussian with diagonal covariance. The systematic uncertainties on the $\mathbf{Y}^{\text{data}}$ dataset and their effect on the unfolding result are discussed in Sec. 5.10.

The DCA_T data sets, in contrast, each comprise a histogrammed distribution of integer-valued entries, and the likelihood $\ln P(\mathbf{D}_j^{\text{data}}|\mathbf{D}_j(\boldsymbol{\theta}))$ is thus more appropriately described by a multivariate Poisson distribution. However, the likelihood calculation for the DCA_T data sets requires three

additional considerations. First, there are significant background contributions from a variety of sources, as discussed in section 5.7. Secondly, detector acceptance and efficiency effects are not explicitly accounted for in the DCA_T distributions. This implies that the total measured yield of signal electrons in each DCA_T histogram is below what was actually produced, and consequently the measured $\mathbf{D}_j^{\text{data}}$ distributions do not match the predictions in normalization. Lastly, because of the high number of counts in the region near $\text{DCA}_T = 0$, this region will dominate the likelihood and be very sensitive to systematic uncertainties in the DCA_T shape there, even though the main source of discrimination between charm and bottom electrons is at larger DCA_T.

To deal with the first issue, the relatively normalized background described in Sec. 5.7 is added to each prediction of the DCA_T distribution for summed electrons from charm and bottom hadrons so that the shape and relative normalization of the background component of the measurement is accounted for.

To handle the second, each prediction plus the background is scaled to exactly match the normalization of $\mathbf{D}_j^{\text{data}}$. In this way, only the shape of the prediction is a constraining factor.

To deal with the third, a 5% uncertainty is added in quadrature to the statistical uncertainty when the number of counts in a given DCA_T bin is greater than a reasonable threshold (which we set at 100 counts). This accounts for the systematic uncertainty in the detailed DCA_T shape by effectively deweighting the importance of the region $\text{DCA}_T \approx 0$ while maintaining the overall electron yield normalization (as opposed to removing the data entirely). This additional uncertainty also necessitates changing the modeling of $\ln P(\mathbf{D}_j^{\text{data}}|\mathbf{D}_j(\boldsymbol{\theta}))$ from a Poisson to a Gaussian distribution. We have checked that varying both the additional uncertainty and the threshold at which it is added has little effect on the results.

5.9.4   Decay model and matrix normalization

The PYTHIA-6 [106] generator with heavy flavor production process included, via the parameter MSEL=4(5), is used to generate parent charm (bottom) hadrons and their decays to electrons. Electrons within $|\eta| < 0.35$ decayed from the ground state charm hadrons ($D^{\pm}$, D^0, D_s, and Λ_c) or bottom hadrons ($B^{\pm}$, B^0, B_s, and Λ_b) are used to create a decay matrix between hadron p_T (p_T^h, representing charm hadron p_T, p_T^c, or bottom hadron p_T, p_T^b) and electron p_T (p_T^e) and DCA_T. Here we treat the feed down decay $B \to D \to e$ as a bottom hadron decay and exclude it from charm hadron decays.

The probability for a charm or bottom hadron at a given p_T^h to decay to an electron at a given p_T^e and DCA_T is encoded in the multidimensional matrices $\mathbf{M}^{(\mathbf{Y})}$ and $\mathbf{M}_j^{(\mathbf{D})}$. An example decay matrix for charmed hadrons is shown in Figure 5.14. Note that the marginal probabilities do not integrate to unity in these matrices. This is because the decay probabilities are normalized to the number of hadrons that are generated at all momenta, in all directions, and over all decay channels. The probability distribution for a hadron integrated over all rapidities and decay channels within a given p_T^h range to decay to an electron at $|y| < 0.35$ with a given p_T^e (integrated over DCA_T) is shown in Fig. 5.15 for an example set of p_T^h bins.

In principle, this decay matrix introduces a model dependence to the result. In the creation of the decay matrix we are integrating over all hadron rapidities as well as combining a number of hadron species and their decay kinematics to electrons. This involves two assumptions. The first is that the rapidity distributions of the hadrons are unmodified. BRAHMS found that the pion and proton R_{AA} did not depend strongly on rapidity up to $y \approx 3$ [165], justifying the assumption. This assumption will further lead us to quote charm and bottom hadron yields as a function of p_T integrated over all rapidity. The second assumption is that all ground state charm hadrons experience the same modification as a function of p_T^c. While different than the charm suppression, all bottom hadrons are assumed to experience the same modification.

An enhancement in the baryon to meson production ratios in both non-strange and strange hadrons has been measured at RHIC [166], which may carry over into the heavy quark sector, invalidating the second assumption. While there are some models [167] that attempt to incorporate this anomalous enhancement into the charm hadrons to help explain the measured heavy flavor electron R_{AA}, there are few measurements to help constrain this proposed enhancement. Following Ref. [168], we have tested the effect of this assumption by applying the observed baryon/meson enhancement to both the Λ_c/D and Λ_b/B ratios. As in Ref. [168], we assume that the modification asymptotically approaches 1 for hadron $p_T > 8$ GeV/c. We find that including the enhancement gives a lower charm hadron yield at high-p_T and a larger bottom hadron yield at high-p_T, but the modifications are within the systematic uncertainties discussed in Section 5.10 and shown in Figure 6.1. We also find a larger bottom electron fraction, which is again within the systematic uncertainties shown in Figure 6.2. While we have not used other particle generators to create alternate decay matrices, we find that the D^0 and $D^\pm$ meson p_T and rapidity distributions from PYTHIA are similar to those given by Fixed Order + Next-to-Leading Log (FONLL) calculations [8]. We

have not included any systematic uncertainty due to this model dependence in the final result.
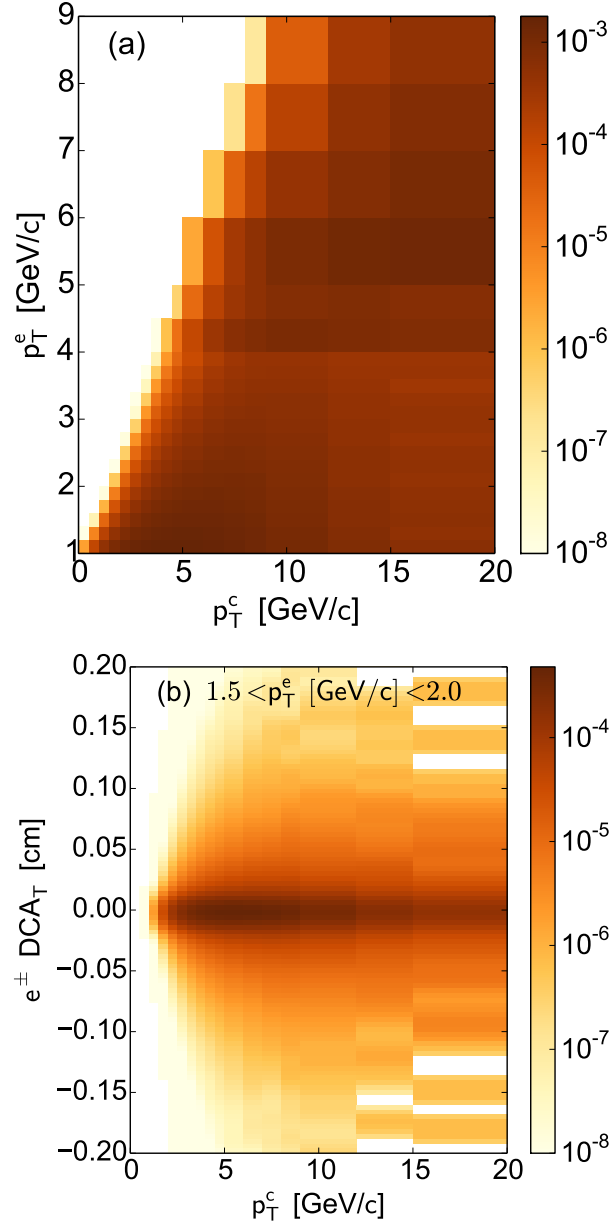
Figure 5.14:   (a) The decay matrix, $\mathbf{M}^{(\mathbf{Y})}$, encoding the probability for charmed hadrons decaying to electrons within $|\eta| < 0.35$ as a function of both electron p_T (p_T^e) and charm hadron p_T (p_T^c). (b) An example decay matrix, $\mathbf{M}_j^{(\mathbf{D})}$, encoding the probability for charmed hadrons decaying to electrons within $|\eta| < 0.35$ and $1.5 < p_T^e$ [GeV/c] < 2.0 as a function of both electron DCA_T and charm hadron p_T (p_T^c). In both cases the color intensity represents the probability of decay in the given bin.
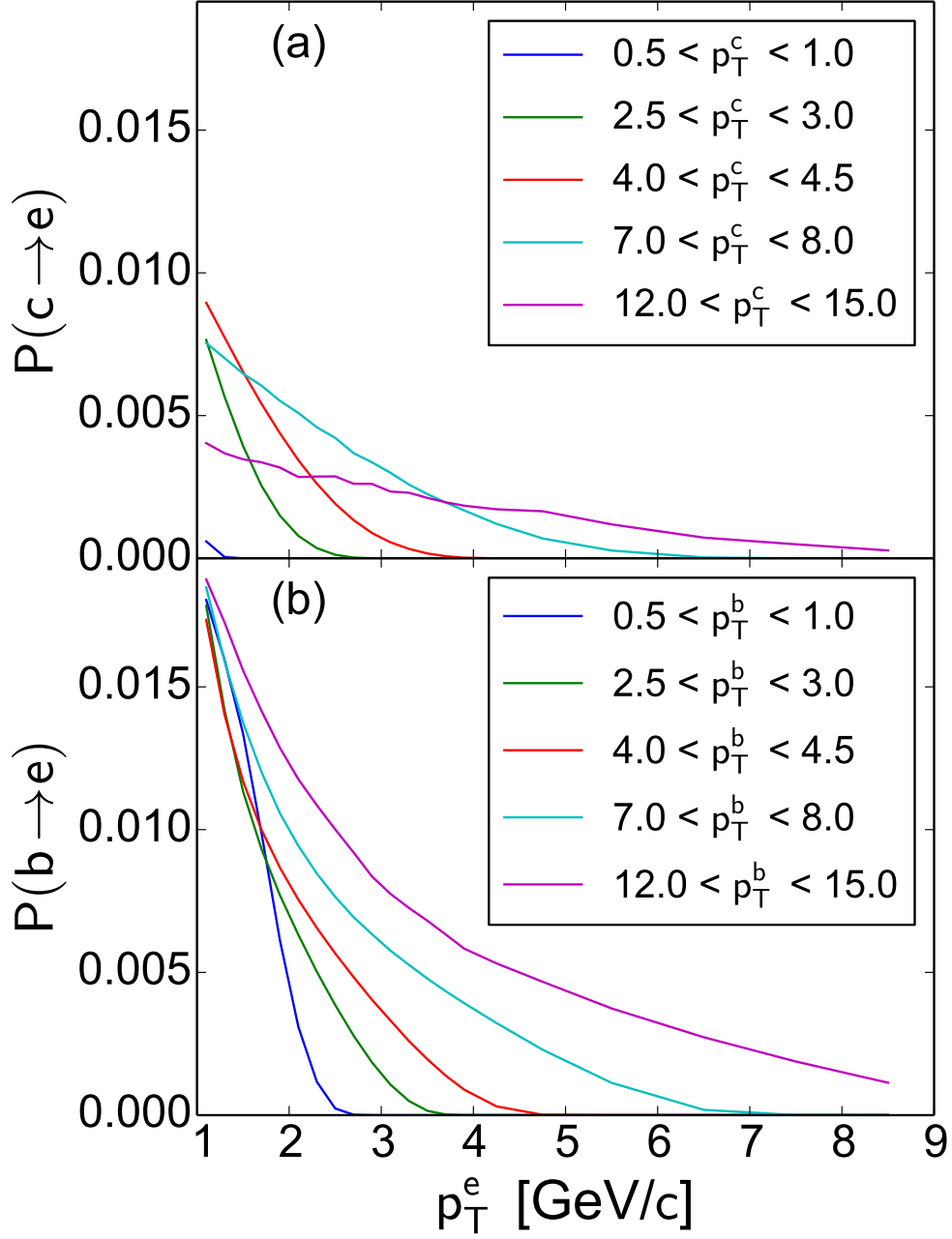
Figure 5.15:   The probability for (a) charm and (b) bottom hadrons in a given range of hadron p_T (p_T^c and p_T^b for charm and bottom hadrons respectively) to decay to electrons at mid-rapidity as a function of electron p_T (p_T^e).

5.9.5 Regularization/prior

To penalize discontinuities in the unfolded distributions of charm and bottom hadrons, we include a regularization term to the right hand side of equation 5.7. In this analysis we included a squared-exponential function

$$\ln \pi(\boldsymbol{\theta}) = -\alpha^2 \left(|\mathbf{LR}_c|^2 + |\mathbf{LR}_b|^2 \right) \tag{5.8}$$

where $\mathbf{R}_c$ and $\mathbf{R}_b$ are ratios of the charm and bottom components of the parent hadron p_T vector to the corresponding 17 components of the prior, $\boldsymbol{\theta}_{\text{prior}}$, and $\mathbf{L}$ is a 17-by-17 second-order finite-difference matrix of the form

$$\mathbf{L} = \frac{17}{2} \begin{pmatrix} -1 & 1 & & & & & & \\ 1 & -2 & 1 & & & & & \\ & 1 & -2 & 1 & & & & \\ & & & \ddots & \ddots & \ddots & & \\ & & & & \ddots & \ddots & \ddots & \\ & & & & 1 & -2 & 1 & \\ & & & & & 1 & -2 & 1 \\ & & & & & & 1 & -1 \end{pmatrix}. \tag{5.9}$$

Thus the addition of this term encodes the assumption that departures from $\boldsymbol{\theta}_{\text{prior}}$ should be smooth by penalizing total curvature as measured by the second derivative.

Here, α is a regularization parameter set to $\alpha = 1.0$ in this analysis. We determine α by repeating the unfolding procedure, scanning over α and choosing the value of α which maximizes the resulting sum of Eq. 5.7 and $-\left(|\mathbf{LR}_c|^2 + |\mathbf{LR}_b|^2\right)$ (Eq. 5.8 dropping α^2). In this way we can directly compare log likelihood values for unfolding results with different α values. We include variations on α in the systematic uncertainty as described in section 5.10.

We set $\boldsymbol{\theta}_{\text{prior}}$ to PYTHIA charm and bottom hadron p_T distributions scaled by a modified blast wave calculation [123] which asymptotically approaches R_{AA} values of $0.2(0.3)$ for $D(B)$ mesons at high-p_T. We have tested the sensitivity of the result to $\boldsymbol{\theta}_{\text{prior}}$ by alternatively using unmodified PYTHIA charm and bottom hadron p_T distributions. We find that the result is sensitive to the choice of $\boldsymbol{\theta}_{\text{prior}}$ dominantly in the lowest charm hadron p_T bins, where there is minimal constraint from the data. We have included this sensitivity in the systematic uncertainty as discussed in section 5.10.

5.9.6   Parent charm and bottom hadron yield and their statistical uncertainty

The outcome of the sampling process is a distribution of $\boldsymbol{\theta}$ vectors, which is 34-dimensional in this case. In principle, the distribution of $\boldsymbol{\theta}$ vectors contains the full probability, including correlations between the different parameters. The 2-D correlations are shown in Figure 5.16. While it is difficult to distinguish fine details in the 34×34-dimensional grid of correlation plots, we can see a few gross features. A circular contour in the 2-D panels represents no correlation between the corresponding hadron p_T bins. An oval shape with a positive slope indicates a positive correlation between corresponding bins, and an oval shape with a negative slope represents an anti-correlation between corresponding bins. A large positive correlation is seen for adjacent bins for high-p_T charm hadrons and low-p_T bottom hadrons. This is a consequence of the regularization, which requires a smooth p_T distribution, and is stronger at the higher and lower p_T regions where there is less constraint from the data. We also see that, while there is little correlation between the majority of nonadjacent p_T bins, there does seem to be a region of negative correlation between the mid to high p_T charm hadrons and the low to mid p_T bottom hadrons. Charm and bottom hadrons in these regions contribute decay electrons in the same p_T region, and appear to compensate for each other to some extent. An example of this is shown between $3.5 < p_T^c$ GeV < 4.0 and $2.5 < p_T^b$ GeV < 3.0 in Figure 5.16(b)-(d).

To summarize $p(\boldsymbol{\theta}|\mathbf{x})$, we take the mean of the marginalized posterior distributions (the diagonal plots in Figure 5.16) for each hadron p_T bin as the most likely values, and the 16$^{\text{th}}$ and 84$^{\text{th}}$ quantiles to represent the $\pm 1\sigma$ uncertainty in those values due to the statistical uncertainty in the data modified by the regularization constraint.
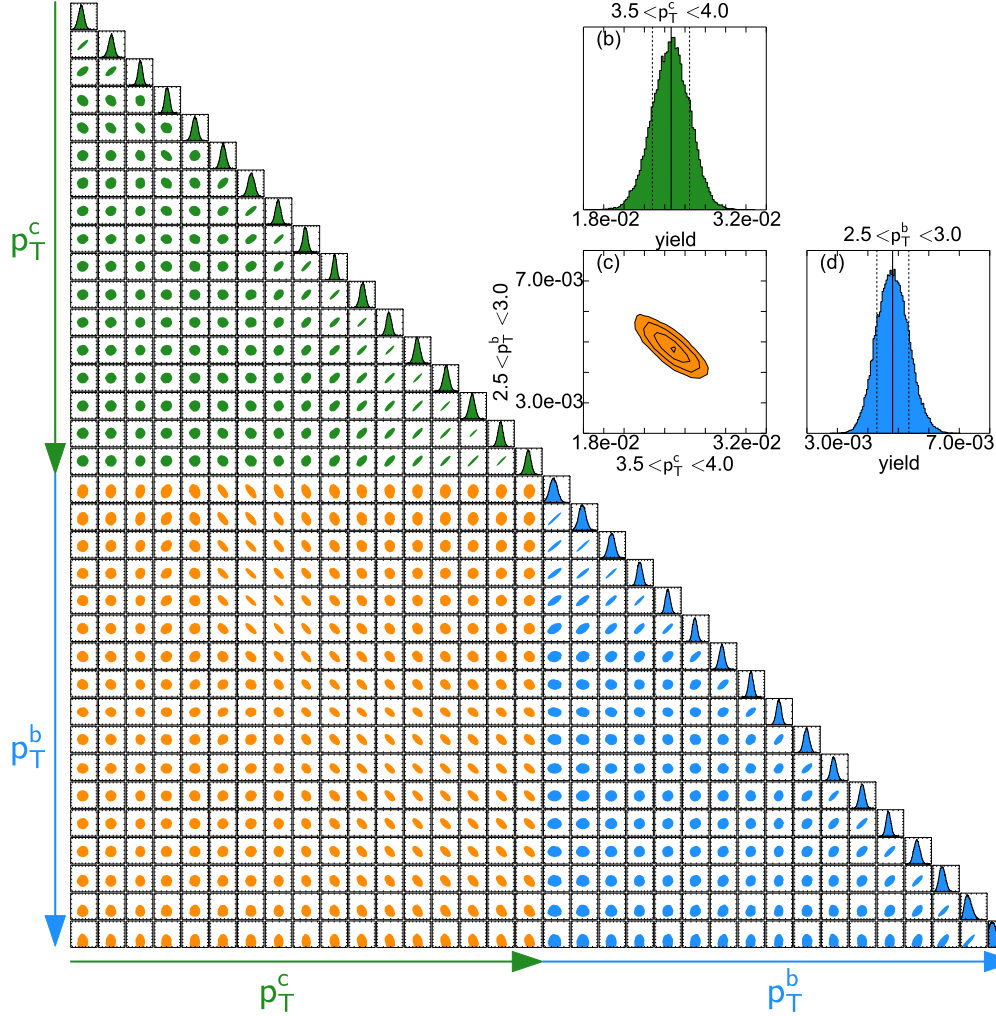
Figure 5.16:   The joint probability distributions for the vector of hadron yields, $\boldsymbol{\theta}$, showing the 2-D correlations between parameters. The diagonal plots show the marginalized probability distributions for each hadron p_T bin (i.e. the 1-dimensional projection over all other parameters). Along the Y-axis the plots are organized from top to bottom as the 17 charm hadron p_T (p_T^c) bins from low to high p_T^c followed by the 17 bottom hadron p_T (p_T^b) bins from low to high p_T^b. The X-axis is organized similarly from left to right. The p_T^c and p_T^b binning follows that shown in Figure 6.1. The region of green plots shows the charm hadron yields and the correlations between charm hadron yields. The region of blue plots shows the bottom hadron yields and correlations between bottom hadron yields. The region of orange plots shows the correlations between charm and bottom hadron yields. Sub-panels (b)-(d) show a set of example distributions. (b) The 1-D probability distribution of charm hadron yield in $3.5 < p_T^c$ GeV < 4.0. (d) The 1-D probability distribution of bottom hadron yield in $2.5 < p_T^b$ GeV < 3.0. (c) The correlation between (b) and (d).107

5.10   Systematic uncertainties

When performing the unfolding procedure, only the statistical uncertainties on the electron DCA_T and p_T spectra are included. In this section we describe how we consider the systematic uncertainties on both the measured data and the unfolding procedure. We take the following uncertainties into account as uncorrelated uncertainties:

1. Systematic uncertainty in the heavy flavor electron p_T invariant yield

2. Uncertainty in the high-multiplicity background

3. Uncertainty in the fraction of nonphotonic electrons (F_{NP})

4. Uncertainty in K_{e3} normalization

5. Regularization parameter α

6. Uncertainty in the form of $\boldsymbol{\theta}_{\mathrm{prior}}$

The uncertainty in F_{NP} (See section A.2), and K_{e3} are propagated to the unfolded hadron yields by varying each independently by $\pm 1\sigma$, and performing the unfolding procedure with the modified background template. The difference between the resulting hadron yields and the central values is taken as the systematic uncertainty. The same procedure is used to determine the uncertainty in the result due to the regularization parameter, which is varied by $^{+0.60}_{-0.25}$ based on where the summed likelihood from both the data and regularization drops by 1 from the maximum value.

The uncertainty in the high-multiplicity background includes two components. The first is the uncertainty on the normalization of the high-multiplicity background DCA_T distribution, as determined in section 5.7.3 and shown in Figure 5.13. This is propagated to the unfolded hadron yields by varying the normalization by $\pm 1\sigma$ and performing the unfolding procedure with the modified background template, as with the F_{NP} and K_{e3} uncertainties. The second component addresses the small excess in the embedded primary electron distribution observed in Figure 5.9 and not accounted for by using the DCA_T distribution for large DCA_L. We parametrize the excess, which is more than two orders of magnitude below the peak, and apply it to the background components, re-performing the unfolding procedure to find its effect on the hadron yield. Both effects combined are small relative to the dominant uncertainties.

Incorporating the p_T correlated systematic uncertainty on the heavy flavor electron invariant yield is more difficult. Ideally one would include a full

covariance matrix encoding the p_T correlations into the unfolding procedure. In practice, the methodology employed in [11] does not provide a convenient description of the p_T correlations needed to shape the covariance matrix. Instead we take a conservative approach by considering the cases which we believe represent the maximum p_T correlations. We modify the heavy flavor electron invariant yield by either tilting or kinking the spectrum about a given point. Tilting simply pivots the spectra about the given point so that, for instance, the first point goes up by a fraction of the systematic uncertainty while the last point goes down by the same fraction of its systematic uncertainty, with a linear interpolation in between. Kinking simply folds the spectra about the given point so that that the spectrum is deformed in the form of a **V**. We implement the following modifications and re-perform the unfolding procedure:

1. Tilt the spectra about $p_T = 1.8$ GeV by $\pm 1\sigma$ of the systematic uncertainty.

2. Tilt the spectra about $p_T = 5$ GeV by $\pm 1\sigma$ of the systematic uncertainty.

3. Kink the spectra about $p_T = 1.8$ GeV by $\pm 1\sigma$ of the systematic uncertainty.

4. Kink the spectra about $p_T = 5$ GeV by $\pm 1\sigma$ of the systematic uncertainty.

The p_T points about which the spectra were modified were motivated by the points in p_T at which analysis methods and details changed, as discussed in [11]. We then take the RMS of the resulting deviations on the hadron yield from the central value as the propagated systematic uncertainty due to the systematic uncertainty on the heavy flavor electron invariant yield.

The effect of our choice of $\boldsymbol{\theta}_{\mathrm{prior}}$ on the charm and bottom hadron yields is taken into account by varying $\boldsymbol{\theta}_{\mathrm{prior}}$, as discussed in Section 5.9.5. The differences between each case and the central value are added in quadrature to account for the bias introduced by $\boldsymbol{\theta}_{\mathrm{prior}}$.

The uncertainties on the unfolded hadron yields due to the six components described above and the uncertainty determined from the posterior probability distributions are added in quadrature to give the uncertainty shown in Figure 6.1.

Due to the correlations between charm and bottom yields, the relative contributions from the different uncertainties depend on the variable being
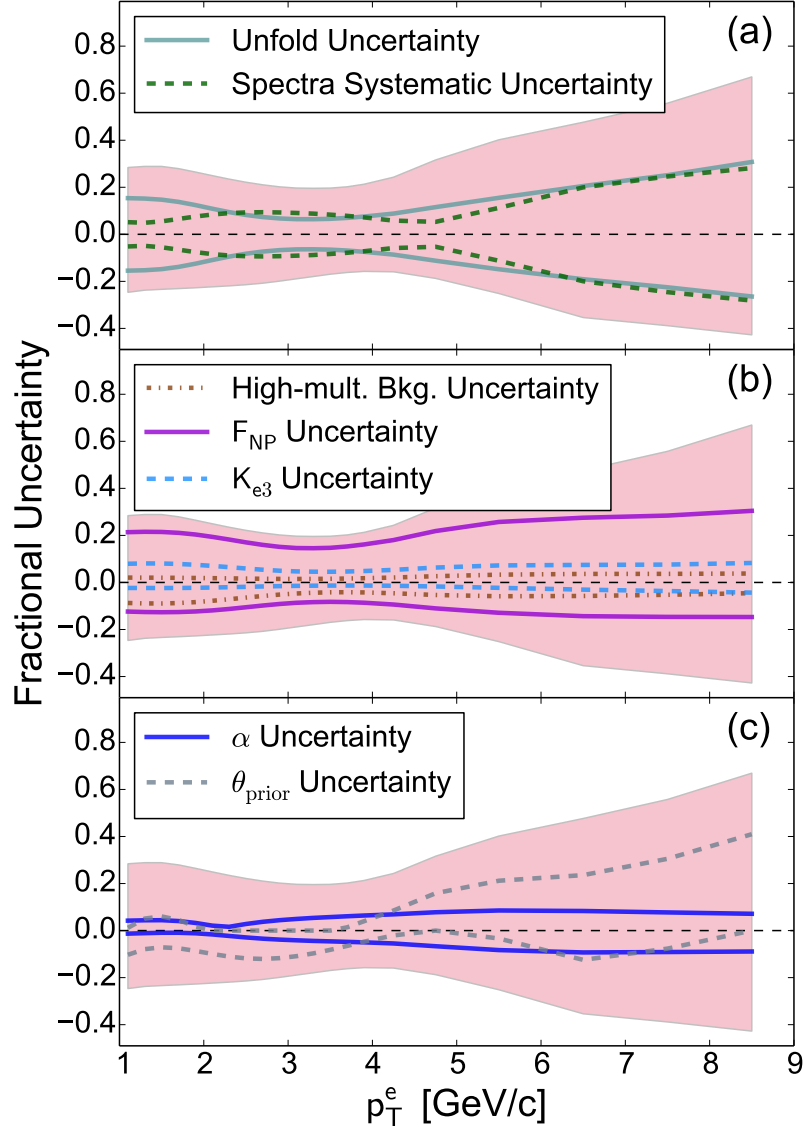
Figure 5.17:   The relative contributions from the different components to the uncertainty on the fraction of electrons from bottom hadron decays as a function of p_T.

The relative contributions from the different components to the uncertainty on the fraction of electrons from bottom hadron decays as a function of p_T. The shaded red band in each panel is the total uncertainty.

plotted. To give some intuition for this, we have plotted the relative contributions from the different uncertainties to the fraction of electrons from bottom

hadron decays as a function of p_T (discussed in Section 6.1) in Figure 5.17. One can see that the dominant uncertainties come from the statistical uncertainty on the DCA_T and heavy flavor electron invariant yield, the systematic uncertainty on the heavy flavor electron invariant yield, and F_{NP}.

Chapter 6

Results

6.1 Invariant yield of charm and bottom hadron

The final result of the invariant yields of charm and bottom hadrons $\frac{1}{2\pi p_T}\frac{dN}{dp_T}$ is obtained. The unfolded results for MB (0%–96%) Au+Au collisions at $\sqrt{s_{_{NN}}} = 200$ GeV are shown in Figure 6.1. The unfolding procedure applied simultaneously to the heavy flavor electron invariant yield as a function of p_T (shown in Figure 7.1) and the five electron DCA$_T$ distributions (shown in Figure 7.2). It is integrated over all rapidity, as a function of p_T. As a reminder, the integration over all rapidity was carried out by assuming the rapidity distribution within PYTHIA is accurate and that it is unmodified in Au+Au, as detailed in section 5.9.4. The central point represents the most likely value and the shaded band represents the 1σ limits on the combination of the uncertainty in the unfolding procedure and the systematic uncertainties on the data, as described in section 5.10. The uncertainty band represents point-to-point correlated uncertainties.

The uncertainties on the hadron invariant yields shown in Figure 6.1 grow rapidly for charm and bottom hadrons with $p_T > 6$ GeV/c . This is due to the lack of DCA$_T$ information for $p_T^e > 5$ GeV/c . Above $p_T^e > 5$ GeV/c , the unfolding is constrained by the heavy flavor electron invariant yield only. This provides an important constraint on the shape of the hadron p_T distributions, but the DCA$_T$ distributions provide the dominant source of discriminating power between the charm and bottom. However, due to the decay kinematics, even high p_T (> 6GeV/c) hadrons contribute electrons in the range $1.5 < p_T^e < 5.0$ GeV/c . We find that charm(bottom) hadrons in the range $7 < p_T^h < 20$ GeV/c contribute 18.2% (0.3%) of the total electron yield in the region $1.5 < p_T^e < 5.0$ GeV/c . This explains the larger uncertainties in the bottom hadron yield compared to the charm hadron yield

112

at high p_T^h.
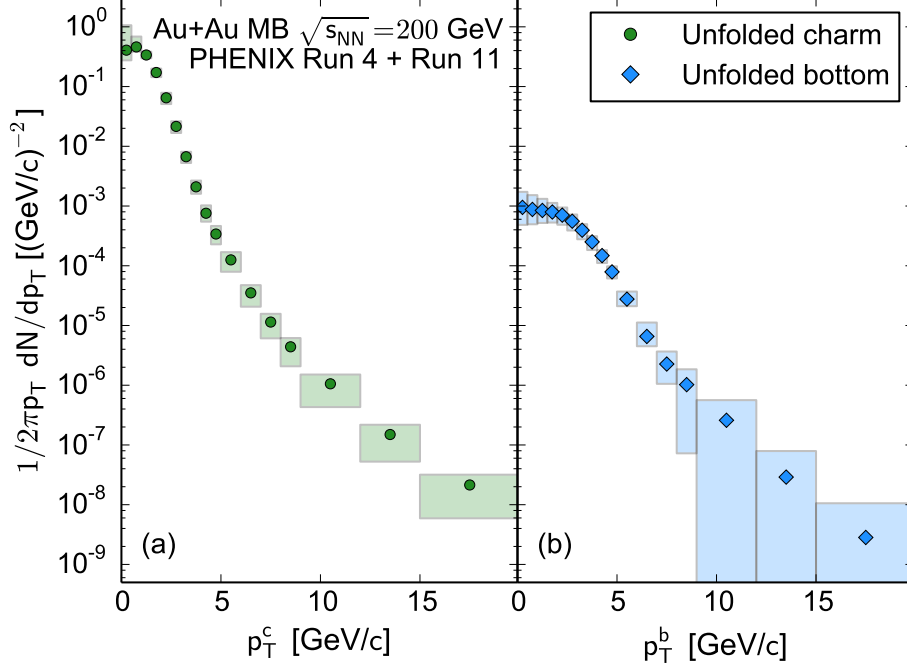
Figure 6.1:   Unfolded (a) charm and (b) bottom hadron invariant yield as a function of p_T, integrated over all rapidities, as constrained by electron yield vs DCA_T in 5 p_T bins and previously published heavy flavor electron invariant yield vs p_T [11].

6.2   Bottom electron fraction

The fraction of bottom electrons from heavy flavor hadrons decay:

$$F_{\mathrm{AuAu}} = \frac{N(b \to e)}{N(b \to e) + N(c \to e)}$$

is computed by the obtained charm and bottom hadron yields shown in Figure 6.1 to get the invariant yield of electrons from charm and bottom decays at midrapidity ($|y| < 0.35$). Here the electrons from bottom hadron decays include the cascade decay $b \to c \to e$. The resulting bottom electron fraction is shown as a function of p_T in Figure 6.2. The central values integrated over the p_T range of each DCA_T distribution are also quoted in Figure 7.2. As in the hadron yields, the band represents the 1σ limits of the point-to-point correlated uncertainties.
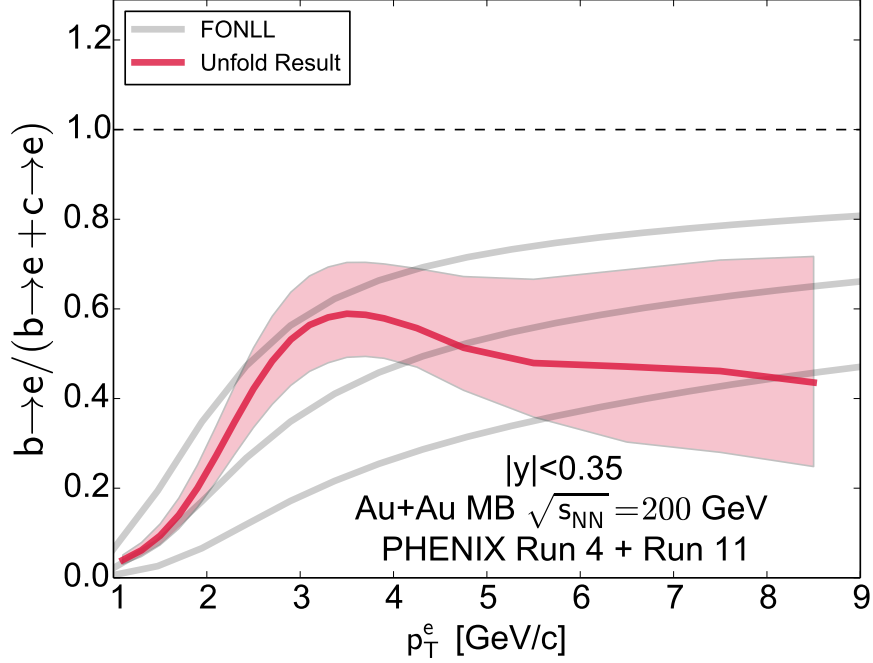
Figure 6.2:   The fraction of heavy flavor electrons from bottom hadron decays as a function of p_T from this work and from FONLL $p+p$ calculations [8].

Also shown in Figure 6.2 is the bottom electron fraction predictions from FONLL [8] (pQCD calculation of expected charm and bottom yields in $p+p$ collisions) at $\sqrt{s_{NN}} = 200$ GeV. We find that the bottom electron fraction is encompassed by the FONLL calculation uncertainties. The shape of the resulting bottom electron fraction shows a steeper rise in the region $2.0 < p_T < 4.0$ GeV/c with a possible peak in the distribution compared to the central value of FONLL calculation.

6.3 R_{AA} of charm electrons and bottom electrons

The fraction of electrons from bottom hadron decays has been previously measured in $p+p$ collisions at $\sqrt{s_{NN}} = 200$ GeV by both PHENIX [13] and STAR [14]. These measurements were made through electron-hadron or electron-D meson correlation methods as reviewed in subsection 3.3.3. These are very different analyses than the one presented here, and have their own model dependencies. In Figure 6.3 we compare the bottom electron frac-
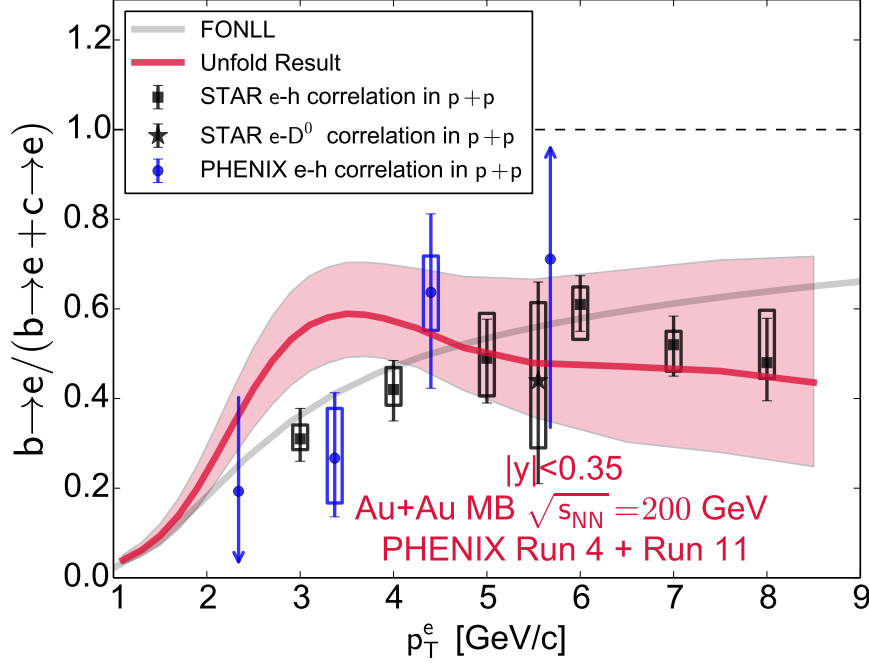
Figure 6.3: bottom electron fraction as a function of p_T compared to measurements in $p+p$ collisions at $\sqrt{s} = 200$ GeV from PHENIX [13] and STAR [14]. Also shown are the central values for FONLL [8] for $p+p$ collisions at $\sqrt{s_{NN}} = 200$ GeV.

tion between our Au+Au result and the electron-hadron correlation measurements in $p+p$. For $p_T > 4$ GeV/c, we find agreement between Au+Au and $p+p$ within the large uncertainties of both measurements. This implies that electrons from bottom hadron decays are similarly suppressed to those from charm, because the total heavy flavor electron are known to be strongly suppressed in Au+Au collisions from the previous PHENIX measurement [11]. For reference, included in Figure 6.3 is the central value of FONLL calculation which, within the large uncertainties, is consistent with the $p+p$ measurements.

With the additional constraints on the bottom electron fraction in $p+p$ from the correlation measurements and the measured nuclear modification of heavy flavor electrons, we can calculate the nuclear modification of electrons from charm and bottom hadron decays separately. The nuclear modifications, $R_{AA}^{c \rightarrow e}$ and $R_{AA}^{b \rightarrow e}$, for charm and bottom hadron decays respectively are calculated using

$$R_{AA}^{c \to e} = \frac{(1 - F_{\text{AuAu}})}{(1 - F_{pp})} R_{AA}^{\text{HF}} \tag{6.1}$$

$$R_{AA}^{b \to e} = \frac{F_{\text{AuAu}}}{F_{pp}} R_{AA}^{\text{HF}}, \tag{6.2}$$

where F_{AuAu} and F_{pp} are the fractions of heavy flavor electrons from bottom hadron decays in Au+Au and $p+p$ respectively and R_{AA}^{HF} is the nuclear modification of heavy flavor electrons (combined charm and bottom). Rather than combining all measurements for the bottom electron fraction in $p+p$, which introduces a further extraction uncertainty, we have chosen to calculate $R_{AA}^{c \to e}$ and $R_{AA}^{b \to e}$ using only the six STAR electron-hadron F_{pp} values. When performing the calculation we determine the full probability distributions assuming Gaussian uncertainties on F_{AuAu}, F_{pp} and R_{AA}^{HF}. As when determining the charm and bottom hadron yields, we take the median of the distribution as the central value, and the 16% and 84% of the distribution as the lower and upper 1σ uncertainties. The resulting values are shown in Figure 6.4(a). We find that the electrons from bottom hadron decays are less suppressed than electrons from charm hadron decays for $3 < p_T < 4$ GeV/c . To further clarify this statement, we calculate the ratio of $R_{AA}^{b \to e}/R_{AA}^{c \to e}$, shown in Figure 6.4(b). In this ratio, the uncertainty on R_{AA}^{HF} cancels. Here again we calculate the full probability distributions and use the same procedure as above to determine the central values and uncertainties. We find that the probability distributions for $R_{AA}^{b \to e}/R_{AA}^{c \to e}$ are highly nonGaussian, which leads to the large asymmetric uncertainty band shown in Figure 6.4(b). It is clear from the ratio that $b \to e$ is less suppressed than $c \to e$ at the 1σ level up to $p_T \sim 4$ GeV.
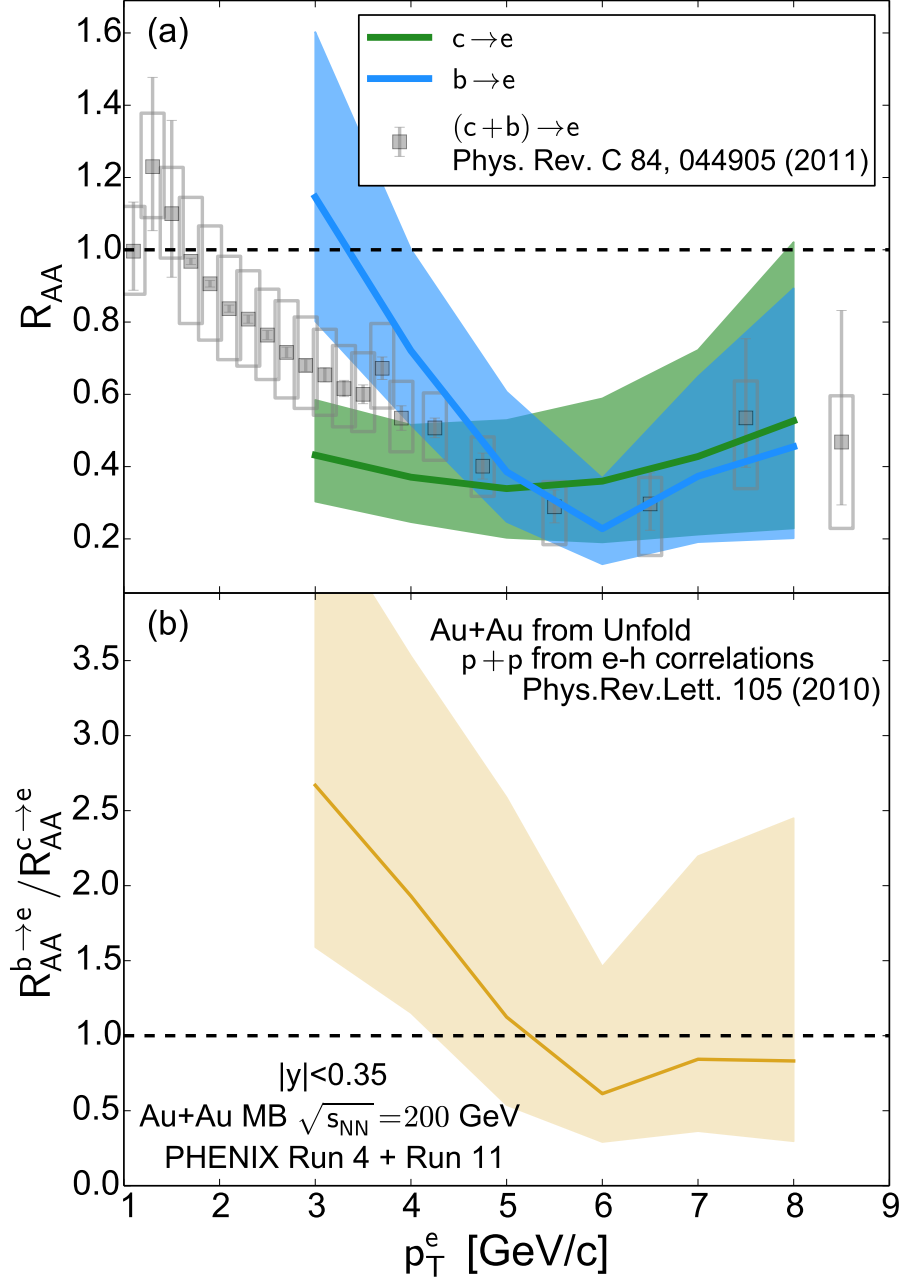
Figure 6.4: (a) The R_{AA} for $c \to e$, $b \to e$ and combined heavy flavor [11] as a function of p_T^e. The $c \to e$ and $b \to e$ R_{AA} is calculated using Eq. 6.1-6.2 where F_{AuAu} uses the unfolded result determined in this work and F_{pp} determined from STAR $e - h$ correlations [14]. (b) The ratio $R_{AA}^{b \to e}/R_{AA}^{c \to e}$ as a function of p_T^e.

117

Chapter 7

Discussion

7.1 Re-folded comparisons to data

The vector of most likely hadron yields obtained the unfolding procedure in section 5.9, with uncertainties can be multiplied by the decay matrix to check the consistency of the result with the measured data (here referred to as re-folding). Figure 7.1 shows the measured heavy flavor electron invariant yield in Au+Au collisions [11] compared with the re-folded electron spectra from charm and bottom hadrons. We find good agreement between the measured data and the electron spectrum from the re-folded charm and bottom hadron yields. Figure 7.2 shows the comparison in electron DCA_T space for each bin in electron p_T. Shown in each panel is the measured DCA_T distribution for electrons, the sum of the background contributions discussed in section 5.7, the DCA_T distribution of electrons from charm hadron decays, and the DCA_T distribution of electrons from bottom hadron decays. Note that the sum of the background contributions is fixed in the unfolding procedure, and only the relative contribution of charm and bottom electrons within $|DCA_T| < 0.1$ cm, as well as their DCA_T shape, vary. For convenience, the region of the DCA_T distribution considered in the unfolding procedure is also shown, as discussed in Section 5.6.2. The sum of the background contributions, charm, and bottom electrons is shown for a direct comparison with the data.

The summed log likelihood values for each of the DCA_T distributions and the electron invariant yield are given in Table 7.1. To aid in the interpretation of the likelihood values, we use a Monte-Carlo method to calculate the expected likelihood from statistical fluctuations around the re-folded result. We draw samples from the re-folded result based on the data statistics and calculate the distribution of resulting likelihood values. The number

Table 7.1:   The log likelihood values (LL) summed over each DCA$_T$ distribution and for the comparison to the heavy flavor electron invariant yield. Also quoted is the number of data points (N_p) and the deviation from the log likelihood value expected from statistical fluctuations (ΔLL), as discussed in the text, for each comparison.

Data set	N_p	LL	ΔLL [σ]
e DCA$_T$ $1.5 < p_T^e < 2.0$	50	-195.5	-3.8
e DCA$_T$ $2.0 < p_T^e < 2.5$	50	-156.5	-2.9
e DCA$_T$ $2.5 < p_T^e < 3.0$	50	-115.8	-0.6
e DCA$_T$ $3.0 < p_T^e < 4.0$	50	-104.1	-1.8
e DCA$_T$ $4.0 < p_T^e < 5.0$	50	-53.2	0.0
e Inv. Yield. $1.0 < p_T^e < 9.0$	21	-45.9	-3.5
Total Sum	271	-673.8	

of standard deviations from the expected value is also shown in Table 7.1. We find that the log likelihood values are large compared to expectations in the heavy flavor electron invariant yield as well as the lowest two DCA$_T$ p_T bins. We note that the likelihood values do not incorporate the systematic uncertainties on the data, which are handled separately as described in Section 5.10. In particular the statistical uncertainties on the heavy flavor electron invariant yield are much smaller than the systematics at low-p_T, making the likelihood value not surprising. We find reasonable agreement within uncertainties between the remaining DCA$_T$ p_T bins.
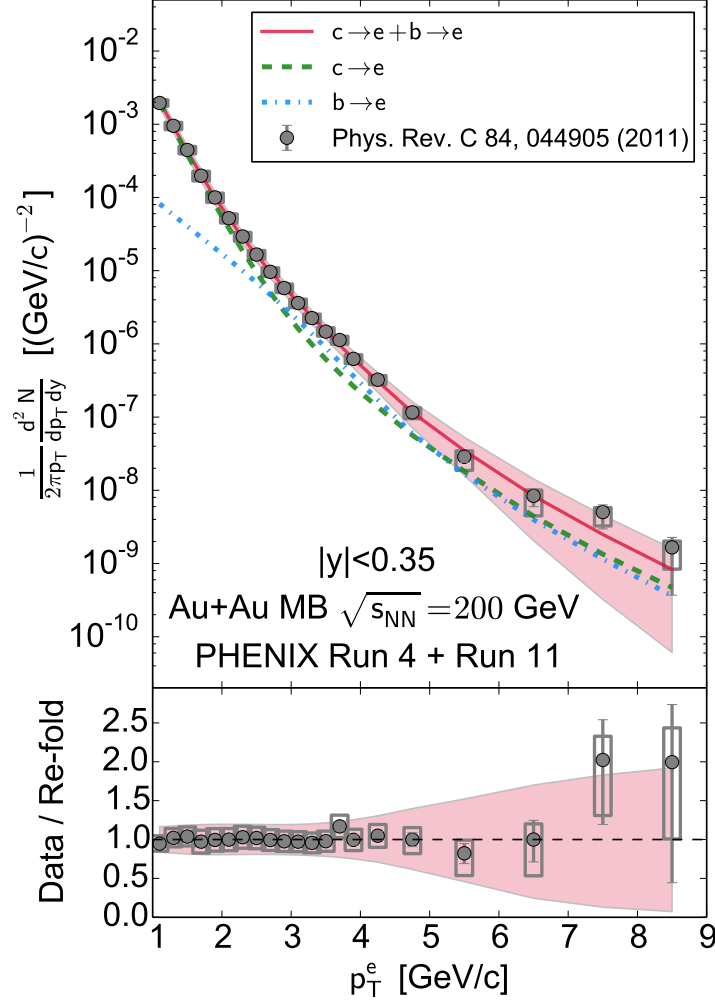
Figure 7.1:   The heavy flavor electron invariant yield as a function of p_T from measured data [11] compared to electrons from the re-folded charm and bottom hadron yields. The boxes represent the point-to-point correlated uncertainties on the measured heavy flavor electron invariant yield, while the error bars on the points represent the point-to-point uncorrelated uncertainties. The label "PHENIX Run 4 + Run 11" on this and all subsequent plots indicates that the unfolding result uses the heavy flavor electron invariant yield as a function of p_T from data taken in 2004 (Run 4) combined with DCA_T measurements from data taken in 2011 (Run 11).
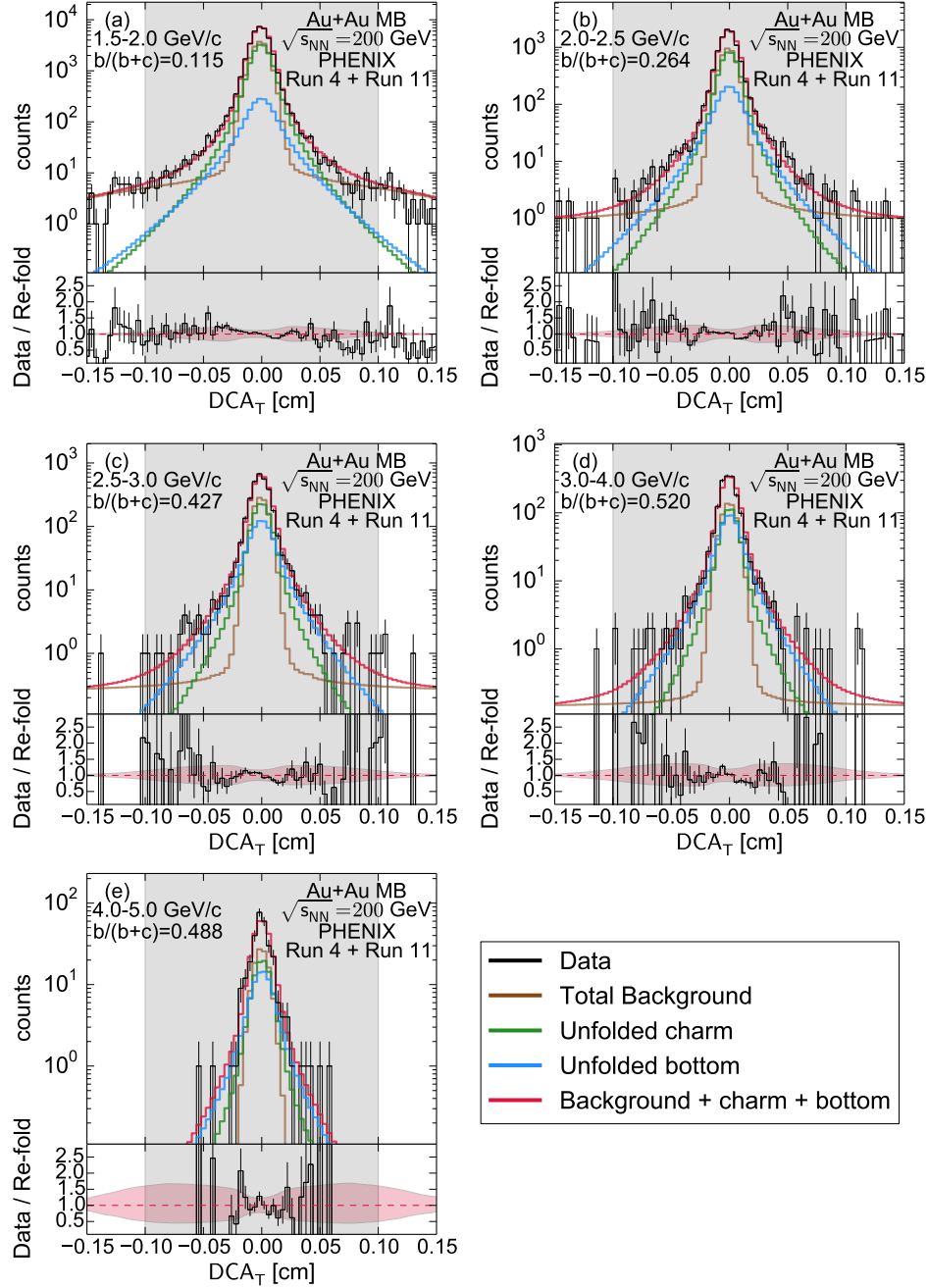
Figure 7.2: The DCA_T distribution for measured electrons compared to the decomposed DCA_T distributions for background components, electrons from charm decays, and electrons from bottom decays. The sum of the background components, electrons from charm and bottom decays is shown as the red curve for direct comparison to the data. The gray band indicates the region in DCA_T considered in the unfolding procedure. Also quoted in the figure is the bottom electron fraction for $|DCA_T| < 0.1$ cm integrated over the given p_T range.

7.2 Comparison with STAR D_0 yield measurement

The yield of D^0 mesons over $|y| < 1$ as a function of p_T has been previously published in Au+Au collisions at $\sqrt{s_{NN}}$ =200 GeV by STAR [15]. In order to compare our unfolded charm hadron results over all rapidity to the STAR measurement, we used PYTHIA to calculate the fraction of D^0 mesons within $|y| < 1$ compared to charm hadrons over all rapidity. Since the measurement by STAR is over a narrower centrality region (0%–80% vs 0%-96%), we scale the STAR result by the ratio of the N_{coll} values. This comparison is shown in Figure 7.3. For added clarity, we have fit the STAR measurement with a Levy function modified by a blast wave calculation given by

$$
\begin{aligned}
f(p_T) \quad = \quad & p_0 \left(1 - \frac{(1 - p_1)p_T}{p_2} \right)^{1/(1-p_1)} \\
\times \quad & \left(1.3\sqrt{2\pi p_4^2} G(p_T, p_3, p_4) + \frac{p_5}{1 + e^{-p_T + 3}} \right),
\end{aligned}
\tag{7.1}
$$

where $G(p_T, p_3, p_4)$ is a standard Gaussian function, and p_i are the parameters of the fit. The ratio of the data to the fit is shown in the bottom panel of Figure 7.3. We find that, within uncertainties, the D^0 yield derived from our data agrees with that measured by STAR over the complementary p_T range. The our D_0 yield hints at a different trend than the STAR data for $p_T > 5$ GeV/c .
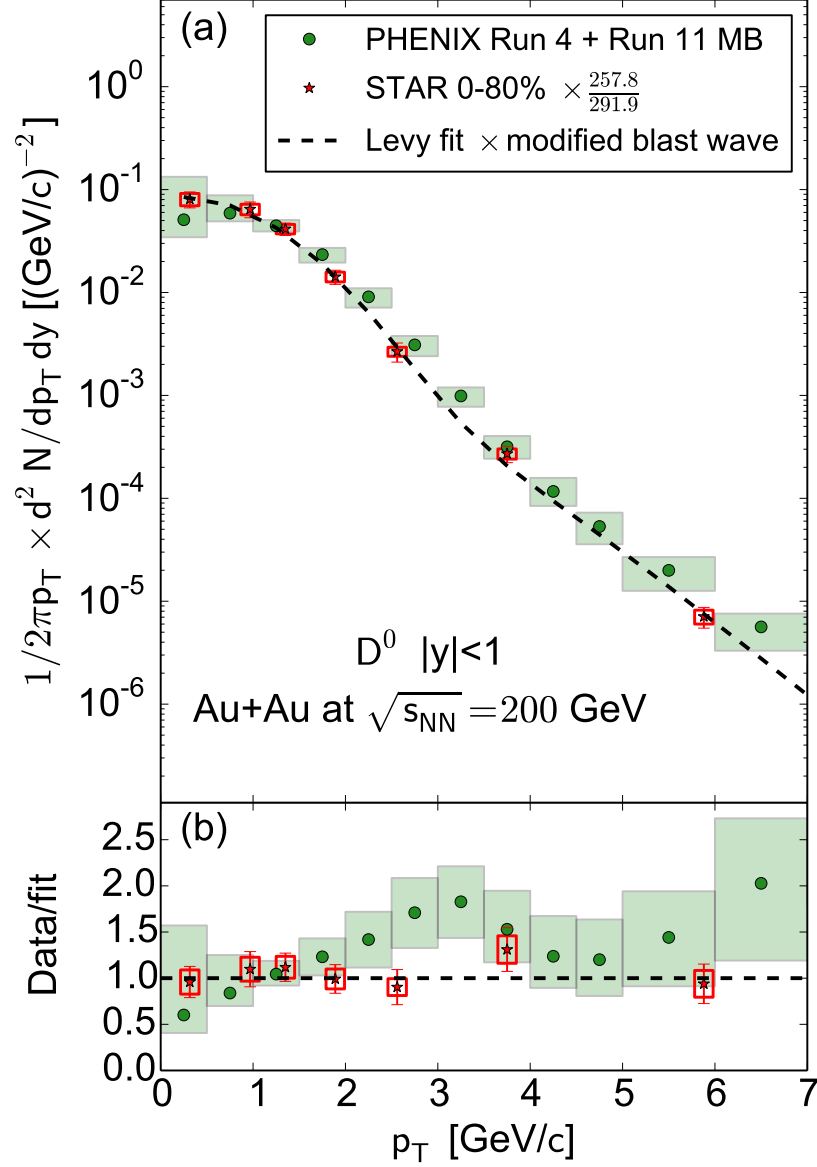
Figure 7.3:   The invariant yield of D^0 mesons as a function of p_T for $|y| < 1$ inferred from the unfolded yield of charm hadrons integrated over all rapidity compared to measurements from STAR [15]. See the text for details on the calculation of the D^0 yield inferred from the unfolded result. To match the centrality intervals, the STAR result has been scaled by the ratio of N_{coll} values. The bottom panel shows the ratio of the data to a fit of the STAR D^0 yield.

7.3   Comparison with theoretical models

There are a number of theoretical calculations in the literature for the interaction of charm and bottom quarks with the QGP. Many of these models predicted the nuclear modification factor R_{AA} for electrons from charm decays and, R_{AA} for electrons from bottom decays, separately, based on different energy loss models to explain the R_{AA}. Models plotted in Figure 7.4(a) calculate radiative energy loss, while other models plotted in Figure 7.4(b),(c),(d) take into account only collisional energy loss.

For consistency, we have assumed the FONLL [8] yields for electrons from charm (bottom) decays calculated for $p+p$ at $\sqrt{s_{NN}}$ =200 GeV and then scaled them by the heavy-ion model results for the R_{AA} of electrons from charm (bottom).

Figure 7.4:   Bottom electron fraction as a function of p_T compared to a series of model predictions detailed in the text.

Figure 7.4(a) compares the bottom electron fraction from one class of

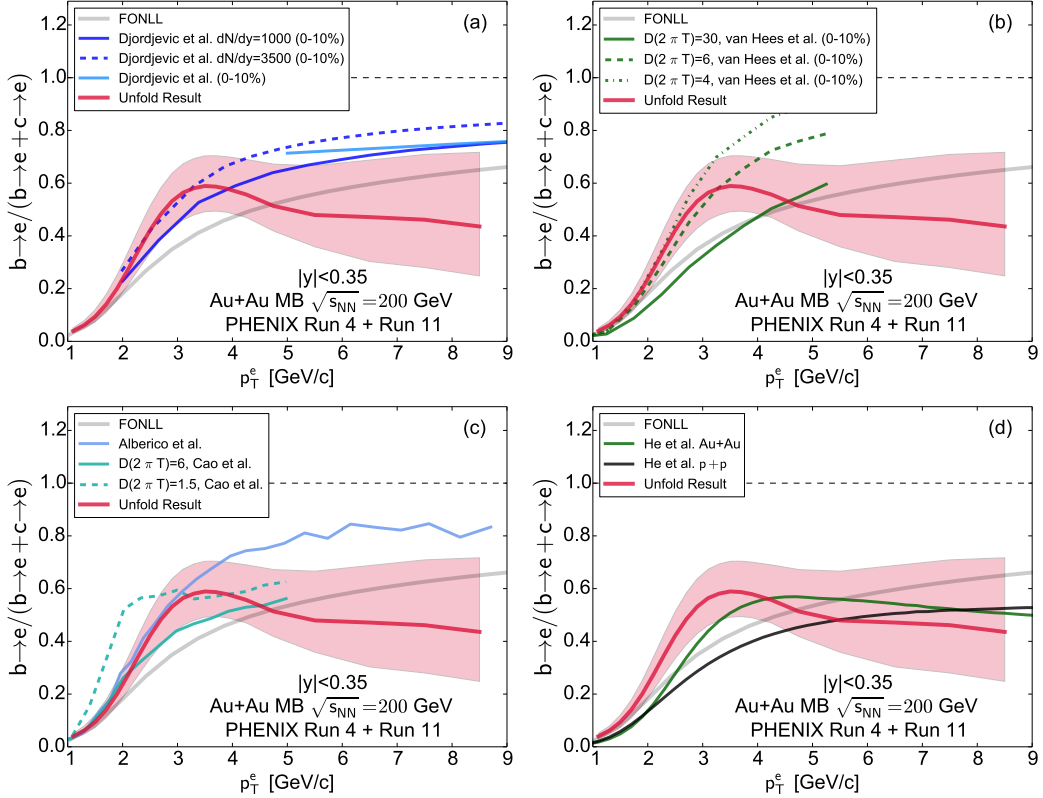calculations modeling only energy loss of these heavy quarks in medium. In an early pQCD calculation by Djordjevic, Gyulassy, Vogt, and Wicks [133], the authors assume an effectively static medium and apply the DGLV theory of radiative energy loss. They find that even for extreme opacities with gluon rapidity densities dN_g/dy up to 3500, the bottom quark decay electrons dominate at high-p_T and that limits the single electron R_{AA} to the range 0.5 – 0.6 for $p_T > 5$ GeV/c . Although this result is known to be higher than the previous PHENIX measured heavy flavor electron R_{AA} [11], we show the $b \to e/(b \to e + c \to e)$ predictions for gluon rapidity densities of 1000 and 3500 in Figure 7.4(a). We do note that the calculations are for 0%–10% central collisions compared to the MB data, although the calculations span a factor of 3.5 range in the gluon density. We find that the calculations with two gluon rapidity densities dN_g/dy are in good agreement with our results for $p_T < 4$ GeV/c , but are slightly above and outside the uncertainty band on our result at higher p_T.

More recent calculations which extend the theory in the previous paragraph [134] also shown in Figure 7.4(a) as a light blue line, gives a similar value to their previous result, but is only published for $p_T > 5$ GeV/c . This updated model assumes a dynamical medium with the average temperature T = 221 MeV (as extracted by PHENIX direct photon measurement [20]), including the collisional energy loss [134, 169] and initial state effects [170, 171], result in a heavy flavor electron high p_T R_{AA} closer to 0.3 and in reasonable agreement with the previous PHENIX published results [11].

Figure 7.4(b) compares the bottom electron fraction from a calculation for collisional energy loss using a T-matrix approach which take into account heavy quark-light quark resonace states in the QGP by van Hees, Mannarelli, Greco, and Rapp [124]. For 0% – 10% central Au+Au collisions, they provided us with different results by changing the coupling of the heavy-quark to the medium. The coupling is encapsulated in the diffusion parameter D, where smaller values yield a stronger coupling. Shown in Figure 7.4(b) are three results corresponding to three values of the parameter $D(2\pi T) = 4, 6, 30$. The largest $D(2\pi T)$ value (30), corresponding to the weakest coupling, agrees well with the $p+p$ reference FONLL result. The successively stronger couplings push the bottom fraction contribution higher and higher. We find that the calculations with $D(2\pi T) = 4, 6$ are in good agreement with our result for $p_T < 4$ GeV/c , but begin to deviate largely at 5 GeV/c where the calculation stops.

Figure 7.4(c) compares the bottom electron fraction from another class of calculations which employ a combination of Langevin, or transport type modeling of heavy-quarks, in the bulk QGP with energy loss mechanisms that dominate at higher p_T. In Ref. [126], Alberico *et al.* employed a Langevin

calculation in the background of an expanding deconfined medium described by ideal and viscous hydrodynamics, while the interaction of the heavy quarks with the QGP is treated within a weakly coupled framework. It is notable that this calculation has a very strong suppression of charm decay electrons such that bottom contributions dominate even at modest $p_T \geq 2 \, \text{GeV}/c$. The calculations are consistent with the data for $p_T < 4$ GeV and over-predict the bottom contribution for higher p_T values.

Figure 7.4(c) also compares the bottom electron fraction from another variant of the Langevin calculation by Cao *et al.* [125]. For this calculation, we show two results corresponding to two different input values $D(2\pi T) = 1.5$ and 6. For the lower parameter, again stronger heavy-quark to medium coupling, there is a sharp rise in the bottom contribution which then flattens out. This feature is due to the increased collisional energy loss, which has a larger effect on the charm quarks, coupled with the strong radial flow effects enabling the heavier bottom quarks to dominate even at $p_T \sim 2\text{GeV}/c$. These calculations used an impact parameter of $b = 6.5$ fm, which should roughly correspond to MB collisions. We find that the calculation using the larger value of $D(2\pi T) = 6.0$ is in reasonable agreement with the data across the calculated p_T range.

Lastly, Figure 7.4(d) shows a more recent calculation by He *et al.* employing a T-matrix approach similar to that shown in Figure 7.4(b), but with a number of updates [127]. In this model, (1) nonperturbative heavy quark scattering off light quarks is treated by the a updated T-marices [172], (2) the medium evolution model has been changed to an updated ideal hydro-dynamical model calculation which used the equation of state derived from lattice QCD and tuned initial conditions that sucssessfully reproduced all π, K, p as well as multistrange hadrons observables [173] and, (3) in hadronic phase, the diffusion of D and B mesons is continued with transport coefficients calculated from elastic scattering amplitudes off light hadrons [174]. In this case the authors provided a calculation of the bottom electron fraction in both $p+p$ and Au+Au at $\sqrt{s_{NN}}$ =200 GeV [175], and we therefore do not calculate the bottom fraction using FONLL as a baseline. The calculation is performed for the 20%–40% centrality bin, which the authors find well represents MB. We find that the calculation under-predicts the bottom fraction for $p_T < 3 \, \text{GeV}/c$, although it is worth noting that the calculation in $p+p$ is also below the FONLL curve across the full p_T range. Above $p_T \sim 3$ the calculation is in agreement with the measurement. It is also worth noting that, of the models presented here, this is the only one that shows in Au+Au a slight decrease in the bottom fraction at high p_T.

Since these models decribed above predict different bottom fraction at $p_T > 4 \, \text{GeV}/c$, it is important to reduce the uncertainty of the bottom frac-

tion in higher p_T region for future measurement. The T-matrix approach [124] and transport approaches [125, 126] also predict the elliptic flow parameter v_2 of electron from charm and bottom separately, depending on the coupling between heavy quark and QGP medium. Thus, the measurement of v_2 for electron from charm and bottom will provide further constraints on these models.

There are numerous other calculations in the literature [176–178] that require mapping charm and bottom hadrons to electrons at midrapidity to make direct data comparisons. We look forward to soon being able to test these calculations with analysis of new PHENIX data sets. We also look forward to being able to test those calculations in the form of R_{AA}.

Chapter 8

Conclusion

We have succeeded in measuring the electrons from charm and bottom hadrons decay separately as a function of p_T from Au+Au data taken at $\sqrt{s_{NN}} = 200$ GeV in 2011 with the enhanced vertexing capabilities provided by the VTX detector. In conjunction with previous PHENIX results for the heavy flavor electron invariant yield as a function of p_T [11], we performed an unfolding procedure to infer the parent charm and bottom hadron yields as a function of p_T. We have found that this procedure yields consistent agreement between the heavy flavor electron invariant yield and the newly measured electron DCA_T distributions. It was also confirmed that the extracted D^0 yield vs p_T is in good agreement with that measured by STAR [15] over the complimentary p_T region. Without a proper $p+p$ baseline extracted from a similar analysis it is difficult to make any quantitative statements about the charm or bottom hadron modification within the uncetainties on the current measurement.

We compared the extracted bottom electron fraction to measurements in $p+p$ collisions and have found agreement between Au+Au and $p+p$ for $p_T > 4$ GeV/c within the large uncertainties on both measurements. Since the total heavy flavor electron are known to be strongly suppressed in Au+Au collisions from the previous measurement, the agreement between Au+Au and $p+p$ strongly implies that electrons from charm and bottom hadron decays are suppressed.

Using the bottom fraction in Au+Au collisions obtained from present analysis and that in $p+p$ collisions measured by STAR [14], we calculated the nuclear modification for electrons from charm and bottom hadron decays. We have observed that bottom electron is suppressed for higher p_T region ($p_T > 4$ GeV/c) in Au+Au collisions compared to $p+p$ collisions for the first time in RHIC energy. It strongly implies bottom quarks suffer energy loss in the matter created in Au+Au collisions at RHIC.

The magnitude of suppression is smaller than that of charm in the region of $3 < p_T < 4$ GeV/c and similar for higher p_T region within systematic uncertainty.

We further compared the bottom electron fraction to a variety of theoretical model calculations employing various energy loss mechanisms; radiative energy loss, Langevin transport, and T-matrix approaches. We have found that the extracted bottom electron fraction agrees with a number of models within the relatively large uncertainties, while it provides new constraints on some model parameters.

Since these models predict different bottom fraction at $p_T > 4$ GeV/c , it is important to reduce the uncertainty of the bottom fraction in higher p_T region for future measurement. It is also important to measure the elliptic flow parameter v_2 of electrons from charm and bottom hadron decay, because it would be sensitive to the coupling of the heavy quark to the QGP medium.

We note that a significantly larger statistics data set of Au+Au collisions at $\sqrt{s_{NN}} = 200$ GeV was collected in 2014 with an improved performance of the VTX detector. The 2014 Au+Au data coupled with the $p+p$ data taken in 2015 should be important measurements of the nuclear modification of the charm and bottom electrons in Au+Au collisions.

Acknowledgements

Dr. M. Kurosawa Dr. T. Hachiya, Mr. T. Koblesky, Dr. A. Lebedev, Dr. D. McGlinchey, Dr. M. McCumber, Prof. J. Nagle, Prof. R. Nouicer, Mr. T. Rinn, Prof. M. Rosati, Mr. A. Shaver, , Dr. M. Shimomura , and Dr. M. Wysocki. A lot of discussions with them, their ideas and suggestions are vital for this work.

I would like to thank all of my friends met in the BNL.

Lastly, , I would like to express my gratitudes to my family for their continuous supports and encouragements.

Appendix A

Detailed Normalization of electron background components

This appendix details the calculation of the normalizations for the background components:

- Photonic electrons

- Kaon decay electrons

- Heavy quarkonia decay electrons

using the bootstrap method described in Section 5.8. We first determine the fraction of nonphotonic electrons, F_{NP}. We then calculate the normalization of Dalitz and conversion components followed by the normalization of K_{e3} and quarkonia components.

A.1 Photonic electrons simulation

π^0 simulation

The ratio of conversion electrons to electrons from Dalitz decay of π^0 in year 2011 data ($R_{CD}^{2011}(\pi^0)$) is determined by GEANT3 simulation. Since B0 hits are always required in tracking, conversion electrons come from beam pipe and B0 as shown in Figure A.1. π^0 particles are simulated flat in p_T at first and weighted with a published spectra [157] to account for momentum smearing effects from the finite momentum resolution of the drift chamber and radiative loss of electrons in the material.

As shown in the Figure A.2, the $R_{CD}^{2011}(\pi^0)$ is 1.10 and flat from 1 to 10 GeV/c . In 2004 data [11], $R_{CD}^{2011}(\pi^0)$ is 0.4 [179] and a systematic error of 10%

is conservatively assigned to account for the fact that the actual thickness of
the Be beam pipe as well as the thickness of the contributing layer of air (in
front of the He bag) are not precisely known.

We assign a systematic error of 10% to the $R_{CD}^{2011}(\pi^0)$ in 2011 data as well,
since the actual radiation length of the new Be beam pipe and B0 layer are
not precisely known.
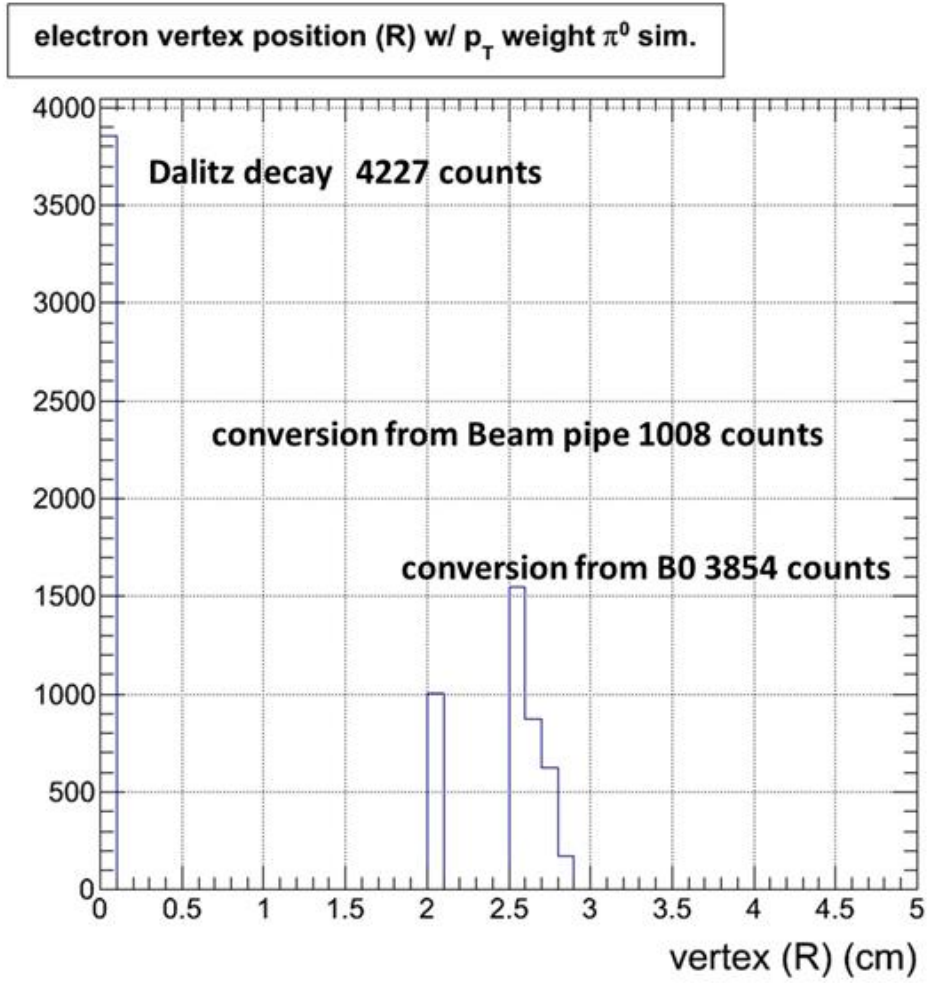
Figure A.1: Electrons' vertex position in radial direction in π^0 simulation before the application of conversion veto. All track cuts described in Chapter 5 are applied.
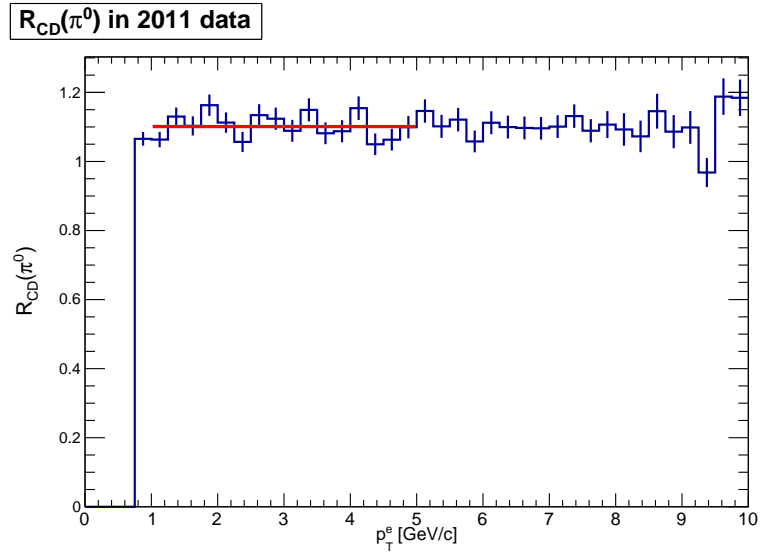
Figure A.2: The ratio of conversion electrons to electrons from Dalitz decay
from π^0 simulation as a function of reconstructed electron's p_T. The red line
is the result of a fit to constant.

η simulation

As we observed in π^0 simulation, the ratio of conversion electrons to electrons from Dalitz decay is p_T independent and not sensitive to the slope of spectra. That ratio of η in 2011 data ($R_{CD}^{2011}(\eta)$) is obtained by just scaling $R_{CD}^{2011}(\pi^0)$, using theoretical relative branching ratios [180] rather than using the experimental values which have large uncertainty.

$$R_{CD}^{2011}(\eta) = R_{CD}^{2011}(\pi^0) * \frac{\dfrac{BR(\eta \to 2\gamma)}{BR(\pi^0 \to 2\gamma)}}{\dfrac{BR(\eta \to e^+, e^-, \gamma)}{BR(\pi^0 \to e^+, e^-, \gamma)}}$$

$$= R_{CD}^{2011}(\pi^0) * \frac{0.0119}{0.0162}$$

$$= 0.809 \tag{A.1}$$

We assigned a systematic uncertainty of 10% to the $R_{CD}(\eta)$ as well.

Direct photon simulation

There are two kind of photonic electrons contributions from direct photons.

- conversion electrons from real direct photons (external conversion)

- electrons from direct virtual photon (internal conversion)

The relation between these two contributions is the same as for Dalitz decay of light neutral mesons. In both cases, we deal with a source emitting photons that can be either real ($\pi^0(\eta) \to \gamma\gamma$ or direct photon) or virtual ($\pi^0(\eta) \to \gamma e^+ e^-$ or direct virtual photon). The contribution from real direct photons are derived from GEANT3 simulation using the measured direct photon spectra published by PHENIX [20, 70]. The evaluation of contribution from direct virtual photon are more complicated, because there is no direct way to simulate it in GEANT3 simulation. For the estimation of the electron contribution from direct virtual photon, we choose to use the Dalitz decay of η shown in Figure A.3 as a representative case, because the phase space for the electron pair emission is similar up to 5 GeV/c [181, 182]. The p_T weight is applied to the virtual photon emitted from the parent η shown in Figure A.3 to match the direct photon spectra [20, 70].

136
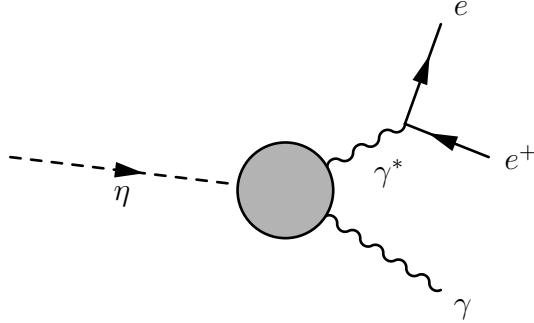
Figure A.3: Diagram of Dalitz decay of η meson.

The ratio of conversion electrons to Dalitz electrons for direct photon
(γ_{dir}) is

$$R_{CD}^{2011}(\gamma_{dir}) = R_{CD}^{2011}(\eta)/2.0 \qquad (A.2)$$
$$= 0.404$$

The factor 2 comes from the fact that π^0 and η decays into 2 photons.

A.2 Fraction of nonphotonic electrons F_{NP}

We first determine F_{NP}, the fraction of nonphotonic electrons to inclusive
electrons after the application of all analysis cuts, including the conversion
veto cut. Note that nonphotonic electrons include contributions from heavy
flavor semi-leptonic decays, quarkonia decays, and kaon decays. Photonic
electrons are from π^0 and η Dalitz decays and photon conversions.

F_{NP} in the 2011 data can be determined using the published 2004 re-
sult [11] as follows. Let Y_{NP} be the yield of nonphotonic electrons and Y_{Dalitz}
the yield of electrons from Dalitz decays. Note that both Y_{NP} and Y_{Dalitz} are
independent of the year of data taking. In the PHENIX 2004 Au+Au data
run, the ratio of the nonphotonic electron yield to the photonic electron yield
(R_{NP}^{2004}) was measured. The relation of Y_{NP} and Y_{Dalitz} is as follows:

$$Y_{\mathrm{NP}} = R_{\mathrm{NP}}^{2004}(1 + R_{CD}^{2004}) \times Y_{Dalitz}, \qquad (A.3)$$

where R_{CD}^{2004} represents the ratio of conversion electron yield to Dalitz electron
yield in the 2004 PHENIX detector. It is calculated as

$$R_{CD}^{2004} = \sum_{i=\pi^0,\eta,\gamma_{dir}} R_{CD}^{2004}(i) \cdot r_{Dalitz}(i). \qquad (A.4)$$

Section APPENDIX A. DETAILED NORMALIZATION OF ELECTRON
BACKGROUND COMPONENTS

Here $R_{CD}^{2004}(i)$ is the ratio of conversion electrons to electrons from Dalitz
decays in the 2004 PHENIX detector calculated by a full GEANT3 simulation.
The factors

- $r_{Dalitz}(\pi^0)$

- $r_{Dalitz}(\eta)$

- $r_{Dalitz}(\gamma_{dir})$

are the fractional contributions of π^0, η, and direct photon contribution to
the total Dalitz decays, respectively[1]. We only consider the contributions of
π^0, η, and γ_{dir} (direct photon) since the sum of other contributions is small
(5% or less). Thus they are normalized such that

$$\sum_i r_{Dalitz}(i) = 1. \tag{A.5}$$

Figure A.4 shows r_{Dalitz} for π^0, η, and direct photon as a function of
transverse momentum of the electrons for MB Au+Au collisions at 200 GeV.
The ratios are calculated from the invariant yield of π^0 [157], η [158], and
direct photons [20, 69].

In the 2011 data set the observed electron yields from conversion and
Dalitz decays are modified by the electron survival probability after the con-
version veto cut is applied. The yield of photonic electrons which pass the
conversion veto (Y_P^{2011}) is

$$Y_P^{2011} = R_{PD}^{2011} \times Y_{Dalitz}, \tag{A.6}$$
$$R_{PD}^{2011} = \sum_{i=\pi^0,\eta,\gamma} \left(S_D(i) + S_C \cdot R_{CD}^{2011}(i) \right) r_{Dalitz}(i), \tag{A.7}$$

where S_C is the survival probability of conversion electrons, $S_D(\pi^0), S_D(\eta), S_D(\gamma_{dir})$
are survival probabilities of Dalitz decay electrons from π^0, η, and direct
photons, respectively, as shown in Fig. 5.12. $R_{CD}^{2011}(i)$ ($i = \pi^0, \eta, \gamma_{dir}$)is the
ratio of conversion electrons to Dalitz electrons for particle i in the 2011
PHENIX detector after the addition of the VTX and the replacement of the
beam pipe. It is determined to be $R_{CD}^{2011}(\pi^0) = 1.10$, $R_{CD}^{2011}(\eta) = 0.809$ and
$R_{CD}^{2011}(\gamma_{dir}) = 0.404$ as described in the previous section.

The fraction of nonphotonic electrons to inclusive electrons can then be
calculated as

---

[1] Here we include internal conversion of direct photon in Dalitz decays. Note that the
Dalitz decay of π^0 (η) is caused by internal conversion of one of two decay photons in
$\pi^0(\eta) \to \gamma\gamma$.
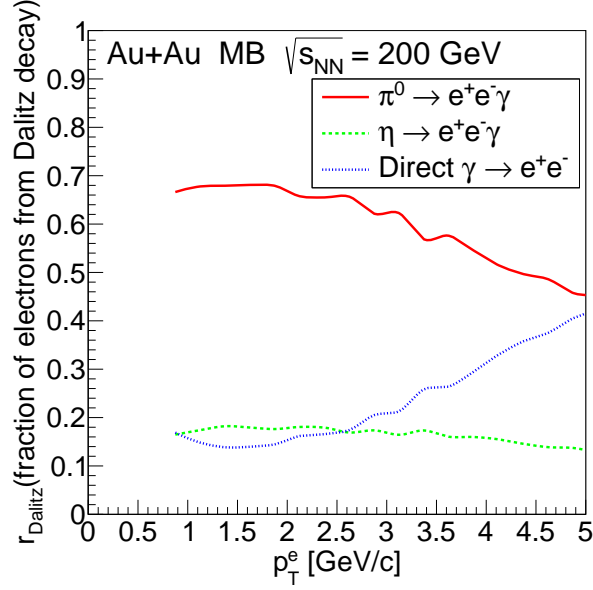
Figure A.4: The fraction of π^0, η, and direct photon Dalitz decay electrons in all Dalitz electrons as a function of electron p_T (p_T^e).

$$F_{\text{NP}} = \frac{Y_{\text{NP}}}{Y_{\text{NP}} + Y_P^{2011}} \tag{A.8}$$

$$= \frac{R_{\text{NP}}^{2004}(1 + R_{CD}^{2004})}{R_{\text{NP}}^{2004}(1 + R_{CD}^{2004}) + R_{PD}^{2011}} \tag{A.9}$$

The resulting F_{NP} as a function of p_T^e and the calculated systematic uncertainties due to the uncertainties on the input yields is shown in Fig. A.5. With F_{NP} in hand, we obtain the number of photonic electrons, N_P^e, and the number of nonphotonic electrons, N_{NP}^e as

$$N_P^e = N_e(1 - F_{\text{NP}}) \tag{A.10}$$

$$N_{\text{NP}}^e = N_e F_{\text{NP}}, \tag{A.11}$$

where N^e is the number of electrons with conversion veto after the subtraction of the hadronic contamination and random background.

139
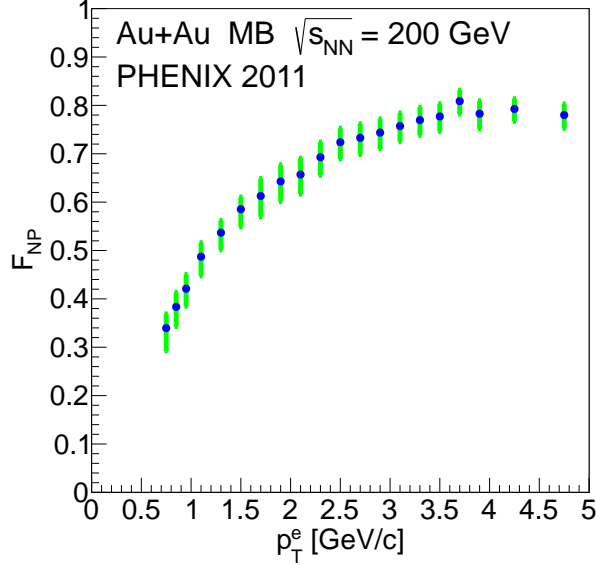
Figure A.5: The fraction of nonphotonic electrons to inclusive electrons as
a function of electron p_T (p_T^e).

A.3 Normalization of Dalitz and conversion components

In the previous section we obtained N_P^e, the number of photonic electrons
in the data after the conversion veto cut. There are two components in the
photonic electrons (N_P^e).

1. Electrons from Dalitz decays ($\pi^0 + \eta + \gamma_{dir}$)

2. Electrons from conversions in the beam pipe and B0

In the next step, we determine the normalization of Dalitz and conversions
separately. This is needed since the shape of DCA_T distribution of Dalitz
and conversions are different.

After application of the conversion veto cut, we have

$$N_C^e(i) = S_C R_{CD}^{2011}(i)(1 - \delta_{random})\epsilon_A Y_{Dalitz}, \qquad (A.12)$$

$$N_D^e(i) = S_D(i)(1 - \delta_{random})\epsilon_A Y_{Dalitz}, \qquad (A.13)$$

$$(i = \pi^0, \eta, \gamma_{dir}) \qquad (A.14)$$
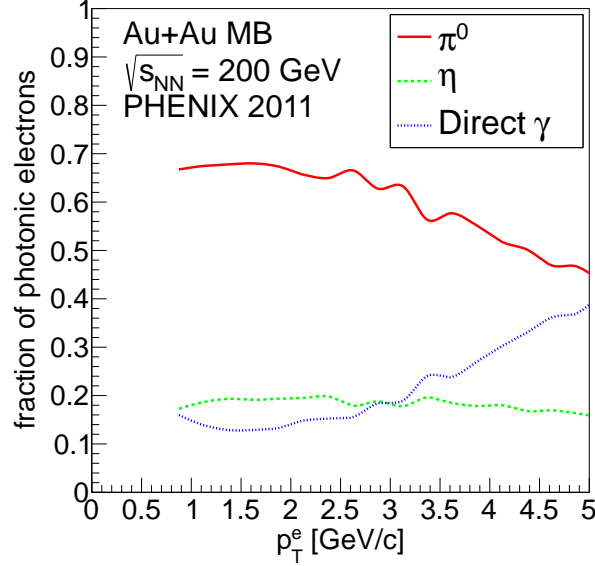
Figure A.6: The fraction of π^0, η, and direct photon electrons in all photonic electrons as a function of electron p_T (p_T^e).

where $N_C^e(i)$ and $N_D^e(i)$ are the number of electrons from conversions and Dalitz from particle i after the conversion veto cut, respectively; δ_{random} is the common reduction factor of tracks due to random hits in the windows of the conversion veto cut; and ϵ_A is the efficiency and acceptance without the conversion veto cut. Since the number of photonic electron is $N_P^e(i) = N_D^e(i) + N_C^e(i)$, the fraction of conversions and Dalitz decays in the photonic electrons are

$$\frac{N_C^e(i)}{N_P^e(i)} = \frac{S_C R_{CD}(i)}{S_D(i) + S_C R_{CD}^{2011}(i)}, \tag{A.15}$$

$$\frac{N_D^e(i)}{N_P^e(i)} = \frac{S_D(i)}{S_D(i) + S_C R_{CD}^{2011}(i)}, \tag{A.16}$$

The fraction of electrons from conversions (N_C^e/N_P^e) and Dalitz (N_D^e/N_P^e) is the average of these fractions, thus:

$$N_C^e = N_P^e \sum_{i=\pi^0,\eta,\gamma_{dir}} r^{ph}(i) \frac{S_C R_{CD}^{2011}(i)}{S_D(i) + S_C R_{CD}^{2011}(i)} \tag{A.17}$$

$$N_D^e = N_P^e \sum_{i=\pi^0,\eta,\gamma_{dir}} r^{ph}(i) \frac{S_D(i)}{S_D(i) + S_C R_{CD}^{2011}(i)}, \tag{A.18}$$

141

where $r^{ph}(i), (i = \pi^0, \eta, \gamma_{dir})$ is the relative contribution of electrons from
(conversion + Dalitz decay) for particle i after application of conversion veto
cut. Figure A.6 shows $r^{ph}(i)$ ($i = \pi^0, \eta, \gamma_{dir}$) as a function of p_T^e.

The conversion contributions are nearly the same for π^0, η and γ_{dir}, and
effectively cancel when calculating the ratio. Therefore, r^{ph} (Figure A.6) is
almost identical with r_{Dalitz} (Figure A.4).

A.4   Normalization of K_{e3} and quarkonia components

The ratio of electrons from kaons to all nonphotonic electrons before the
application of the conversion veto cut, δ_K, is calculated from the ratio of the
nonphotonic electron yield to the electron yield from kaons [11]. Compared
to Ref. [11], we find that $\sim 50\%$ of electrons from kaon decays are removed
by DCA_T and DCA_L cuts as well as the method used to subtract random
background, which contains some real electrons from kaon decays.

The ratio of electrons from J/ψ decays to all nonphotonic electrons before
the application of the conversion veto cut, $\delta_{J/\psi}$, is taken from Ref. [11]. The
survival rate for electrons from J/ψ decays , $S_{J/\psi}$, is taken to be unity, while
the survival rate for K_{e3} decays, S_K, is taken to be the same value as that for
electrons from charm and bottom decays (namely, S_{HF}). See Section 5.7.4
for details.

After application of conversion veto cut, the normalizations of these two
nonphotonic electron components are described by

$$N_{J/\psi}^e = N_{\mathrm{NP}}^e \frac{\delta_{J/\psi} S_{J/\psi}}{\delta_{J/\psi} S_{J/\psi} + \delta_K S_K + (1 - \delta_{J/\psi} - \delta_K) S_{\mathrm{HF}}} \tag{A.19}$$

$$N_K^e = N_{\mathrm{NP}}^e \frac{\delta_K S_K}{\delta_{J/\psi} S_{J/\psi} + \delta_K S_K + (1 - \delta_{J/\psi} - \delta_K) S_{\mathrm{HF}}} \tag{A.20}$$

The number of each DCA component satisfies this sum rule

$$N_e = N_{NP}^e + N_P^e \tag{A.21}$$

$$= N_c^e + N_b^e + N_K^e + N_{J/\psi}^e + N_D^e + N_C^e \tag{A.22}$$

Appendix B

Coordinate offset and coordinate offset calibration

The VTX WEST barrel and the VTX EAST barrel are mechanically independent modules and the relative position between the center of VTX-West coordinate system (O(VTX WEST)) and VTX-East coordinate system (O(VTX EAST)) can be moved on the extension rail (Figure B.1, right) in the PHENIX experimental hall.
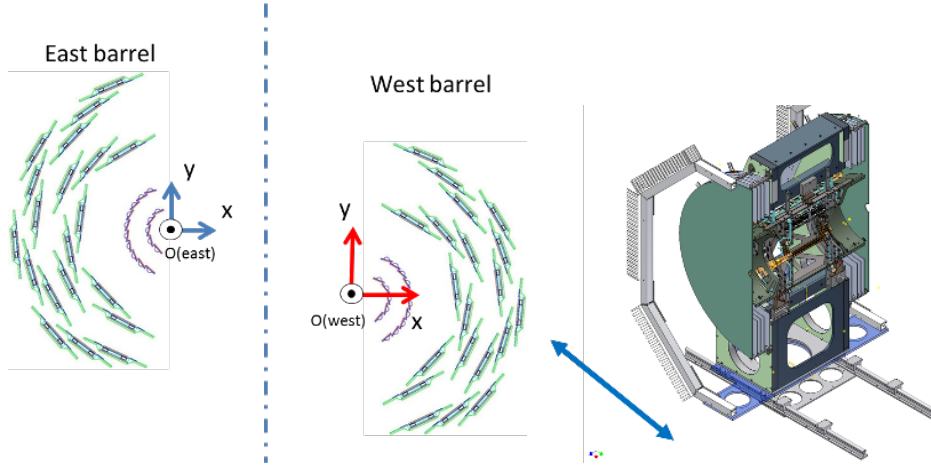
Figure B.1:   (Left) the vtx local coordinate system for the WEST VTX and the EAST VTX. (Right) the schematic view when the VTX is retracted.

There are 3 coordinate systems in the PHENIX central arm; VTX-East, VTX-West and DCH coordinate system. For the association of a central arm track with VTX described in Section 5.4.4, we need to match those 3 coordinate systems. The west and east half barrels of VTX and DCH in

143

the east and west arms are mechanically separated and the relative positions
are shifted in the PHENIX apparatus. Each time after we open up the
apparatus to access to the detectors, we need to calibrate relative positions
of the detectors. The offset calibration is done in the zero magnetic field
run, assuming the beam center position is stable during the run. The beam
center position is used to connect those 3 different coordinate system.
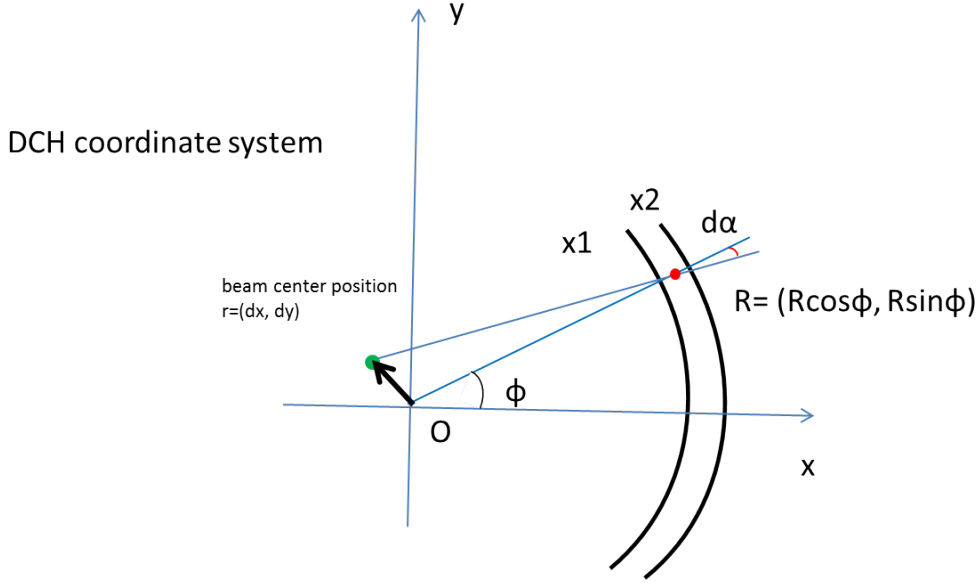
Figure B.2: Parameters of DC hit information and beam center position in
the DCH coordinate system.

Figure B.2 shows a DCH geometry and beam center position. The beam
center position in the x and y direction, dx and dy, are related to $d\alpha$ and ϕ
as follows,

$$\sin d\alpha = \frac{-dx \sin \phi + dy \cos \phi}{R}.$$

Here $dx, dy << R$ is assumed, where R (220 cm) is the middle radius of X1
and X2 plane in DCH.

The beam center position in the VTX-West and VTX-East coordinate
system can be also obtained by the center of primary vertex distribution
which is calculated by VTX half-barrel.

Bibliography

[1] A. Bazavov et al. Equation of state in (2+1)-flavor QCD. *Phys. Rev. D*, 90(9):094503, 2014.

[2] Richard D. Ball et al. Parton distributions with LHC data. *Nucl. Phys.*, B867:244–289, 2013.

[3] K. A. Olive et al. Rev. of Particle Phys. *Chin. Phys. C*, 38:090001, 2014.

[4] S. S. Adler et al. Systematic studies of the centrality and sqrt(sNN) dependence of the dE(T)/deta and d (N(ch) / deta in heavy ion collisions at mid-rapidity. *Phys. Rev.*, C71:034908, 2005. [Erratum: Phys. Rev.C71,049901(2005)].

[5] M. L. Miller, K. Reygers, S. J. Sanders, and P. Steinberg. Glauber modeling in high energy nuclear collisions. *Ann. Rev. Nucl. Part. Sci.*, 57:205, 2007.

[6] Paul Romatschke and Ulrike Romatschke. Viscosity Information from Relativistic Nuclear Collisions: How Perfect is the Fluid Observed at RHIC? *Phys. Rev. Lett.*, 99:172301, 2007.

[7] Y. L. Dokshitzer and D. E. Kharzeev. Heavy quark colorimetry of QCD matter. *Phys. Lett. B*, 519:199, 2001.

[8] M. Cacciari, P. Nason, and R. Vogt. QCD predictions for charm and bottom production at RHIC. *Phys. Rev. Lett.*, 95:122001, 2005.

[9] M. Harrison, T. Ludlam, and S. Ozaki. RHIC project overview. *Nucl. Instrum. Meth.*, A499:235–244, 2003.

[10] M. Aizawa et al. PHENIX central arm particle ID detectors. *Nucl. Instrum. Meth.*, A499:508–520, 2003.

[11] A. Adare et al. Heavy Quark Production in $p+p$ and Energy Loss and Flow of Heavy Quarks in Au+Au Collisions at $\sqrt{s_{NN}}$=200 GeV. *Phys. Rev. C*, 84:044905, 2011.

[12] J. T. Mitchell et al. Event reconstruction in the PHENIX central arm spectrometers. *Nucl. Instrum. Meth.*, A482:491–512, 2002.

[13] A. Adare et al. Measurement of Bottom versus Charm as a Function of Transverse Momentum with Electron-Hadron Correlations in p^+p Collisions at $\sqrt{s} = 200$ GeV. *Phys. Rev. Lett.*, 103:082002, 2009.

[14] M. M. Aggarwal et al. Measurement of the Bottom contribution to nonphotonic electron production in $p + p$ collisions at $\sqrt{s}$=200 GeV. *Phys. Rev. Lett.*, 105:202301, 2010.

[15] L. Adamczyk et al. Observation of D^0 Meson Nuclear Modifications in Au+Au Collisions at $\sqrt{s_{NN}}$=200 GeV. *Phys. Rev. Lett.*, 113(14):142301, 2014.

[16] Szabolcs Borsanyi, Zoltan Fodor, Christian Hoelbling, Sandor D Katz, Stefan Krieg, Claudia Ratti, and Kalman K. Szabo. Is there still any T_c mystery in lattice QCD? Results with physical masses in the continuum limit III. *JHEP*, 09:073, 2010.

[17] A. Bazavov et al. The chiral and deconfinement aspects of the QCD transition. *Phys. Rev.*, D85:054503, 2012.

[18] K. Adcox et al. Formation of dense partonic matter in relativistic nucleus-nucleus collisions at RHIC: Experimental evaluation by the PHENIX Collaboration. *Nucl. Phys. A*, 757:184, 2005.

[19] J. Adams et al. Experimental and theoretical challenges in the search for the quark gluon plasma: The STAR Collaboration's critical assessment of the evidence from RHIC collisions. *Nucl. Phys. A*, 757:102, 2005.

[20] A. Adare et al. Enhanced production of direct photons in Au+Au collisions at $\sqrt{s_{NN}}$=200 GeV and implications for the initial temperature. *Phys. Rev. Lett.*, 104:132301, 2010.

[21] P. Romatschke. New Developments in Relativistic Viscous Hydrodynamics. *Int. J. Mod. Phys. E*, 19:1, 2010.

[22] U. Heinz and R. Snellings. Collective flow and viscosity in relativistic heavy-ion collisions. *Ann. Rev. Nucl. Part. Sci.*, 63:123, 2013.

[23] P. K. Kovtun, Dan T. Son, and A. O. Starinets. Viscosity in strongly interacting quantum field theories from black hole physics. *Phys. Rev. Lett.*, 94:111601, 2005.

[24] M. Gyulassy and L. McLerran. New forms of QCD matter discovered at RHIC. *Nucl. Phys. A*, 750:30, 2005.

[25] U. W. Heinz. RHIC serves the perfect fluid: Hydrodynamic flow of the QGP. In *Proceedings, Workshop on Extreme QCD*, page 3 (2005).

[26] Peter Levai, Berndt Muller, and Xin-Nian Wang. Open charm production in an equilibrating parton plasma. *Phys. Rev.*, C51:3326–3335, 1995.

[27] R. Baier, Yuri L. Dokshitzer, Alfred H. Mueller, S. Peigne, and D. Schiff. Radiative energy loss of high-energy quarks and gluons in a finite volume quark - gluon plasma. *Nucl. Phys.*, B483:291–320, 1997.

[28] M. Baker et al. Proposal for a Silicon Vertex Tracker (VTX) for the PHENIX Experiment. BNL internal report 72204.

[29] A. Adare et al. Single electron yields from semileptonic charm and bottom hadron decays in Au+Au collisions at $\sqrt{s_{NN}} = 200$ GeV. *Phys. Rev.*, C93(3):034904, 2016. arXiv:1509.04662.

[30] David J. Gross and Frank Wilczek. Ultraviolet Behavior of Nonabelian Gauge Theories. *Phys. Rev. Lett.*, 30:1343–1346, 1973.

[31] D. J. Gross and Frank Wilczek. Asymptotically Free Gauge Theories. 1. *Phys. Rev.*, D8:3633–3652, 1973.

[32] H. David Politzer. Reliable Perturbative Results for Strong Interactions? *Phys. Rev. Lett.*, 30:1346–1349, 1973.

[33] Joseph I. Kapusta. Quantum Chromodynamics at High Temperature. *Nucl. Phys.*, B148:461–498, 1979.

[34] John C. Collins and M. J. Perry. Superdense Matter: Neutrons Or Asymptotically Free Quarks? *Phys. Rev. Lett.*, 34:1353, 1975.

[35] Y. Aoki, G. Endrodi, Z. Fodor, S. D. Katz, and K. K. Szabo. The Order of the quantum chromodynamics transition predicted by the standard model of particle physics. *Nature*, 443:675–678, 2006.

[36] Nu Xu and Masashi Kaneta. Hadron freezeout conditions in high-energy nuclear collisions. *Nucl. Phys.*, A698:306–313, 2002.

[37] Szabocls Borsanyi, Zoltan Fodor, Christian Hoelbling, Sandor D. Katz, Stefan Krieg, and Kalman K. Szabo. Full result for the QCD equation of state with 2+1 flavors. *Phys. Lett.*, B730:99–104, 2014.

[38] B. B. Back et al. The PHOBOS perspective on discoveries at RHIC. *Nucl. Phys.*, A757:28–101, 2005.

[39] I. Arsene et al. Quark gluon plasma and color glass condensate at RHIC? The Perspective from the BRAHMS experiment. *Nucl. Phys.*, A757:1–27, 2005.

[40] I. G. Bearden et al. Nuclear stopping in Au + Au collisions at s(NN)**(1/2) = 200-GeV. *Phys. Rev. Lett.*, 93:102301, 2004.

[41] J. J. Aubert et al. The ratio of the nucleon structure functions $F2_n$ for iron and deuterium. *Phys. Lett.*, B123:275, 1983.

[42] J. D. Bjorken. Highly Relativistic Nucleus-Nucleus Collisions: The Central Rapidity Region. *Phys. Rev.*, D27:140–151, 1983.

[43] R. J. Fries, Berndt Muller, C. Nonaka, and S. A. Bass. Hadronization in heavy ion collisions: Recombination and fragmentation of partons. *Phys. Rev. Lett.*, 90:202303, 2003.

[44] S. S. Adler et al. High p_T charged hadron suppression in Au + Au collisions at $\sqrt{s}_{NN} = 200$ GeV. *Phys. Rev.*, C69:034910, 2004.

[45] R. J. Glauber and G. Matthiae. High-energy scattering of protons by nuclei. *Nucl. Phys.*, B21:135–157, 1970.

[46] K. Yagi, T. Hatsuda, and Y. Miake. Quark-gluon plasma: From big bang to little bang. *Camb. Monogr. Part. Phys. Nucl. Phys. Cosmol.*, 23:1–446, 2005.

[47] R. Anni, G. Co, and P. Pellegrino. Nuclear charge density distributions from elastic electron scattering data. *Nucl. Phys.*, A584:35–59, 1995.

[48] R. Keith Ellis, W. James Stirling, and B. R. Webber. QCD and collider physics. *Camb. Monogr. Part. Phys. Nucl. Phys. Cosmol.*, 8:1–435, 1996.

[49] David d'Enterria. Jet quenching. *Landolt-Bornstein*, 23:471, 2010. arXiv:0902.2011.

[50] Stephen D. Ellis, Zoltan Kunszt, and Davison E. Soper. The One Jet Inclusive Cross-section at Order $\alpha^- s^3$ Quarks and Gluons. *Phys. Rev. Lett.*, 64:2121, 1990.

[51] K. Adcox et al. Suppression of hadrons with large transverse momentum in central Au+Au collisions at $\sqrt{s_{NN}} = 130$-GeV. *Phys. Rev. Lett.*, 88:022301, 2002.

[52] J. D. Bjorken. Energy Loss of Energetic Partons in Quark - Gluon Plasma: Possible Extinction of High p(t) Jets in Hadron - Hadron Collisions. 1982.

[53] Enke Wang and Xin-Nian Wang. Jet Tomography of Hot and Cold Nuclear Matter. *Phys. Rev. Lett.*, 89:162301, 2002.

[54] J. W. Cronin, Henry J. Frisch, M. J. Shochet, J. P. Boymond, R. Mermod, P. A. Piroue, and Richard L. Sumner. Production of Hadrons with Large Transverse Momentum at 200-GeV, 300-GeV, and 400-GeV. *Phys. Rev.*, D11:3105, 1975.

[55] A. Krzywicki, J. Engels, B. Petersson, and U. Sukhatme. Does a Nucleus Act Like a Gluon Filter? *Phys. Lett.*, B85:407, 1979.

[56] M. Lev and B. Petersson. Nuclear Effects at Large Transverse Momentum in a QCD Parton Model. *Z. Phys.*, C21:155, 1983.

[57] Alberto Accardi et al. Hard probes in heavy ion collisions at the LHC: Jet physics. 2004. arXiv:0310274.

[58] Eric Braaten and Markus H. Thoma. Energy loss of a heavy quark in the quark - gluon plasma. *Phys. Rev.*, D44:2625–2630, 1991.

[59] Simon Wicks, William Horowitz, Magdalena Djordjevic, and Miklos Gyulassy. Elastic, inelastic, and path length fluctuations in jet tomography. *Nucl. Phys.*, A784:426–442, 2007.

[60] Guang-You Qin, Jorg Ruppert, Charles Gale, Sangyong Jeon, Guy D. Moore, and Munshi G. Mustafa. Radiative and collisional jet energy loss in the quark-gluon plasma at RHIC. *Phys. Rev. Lett.*, 100:072301, 2008.

[61] Guang-You Qin and Xin-Nian Wang. Jet quenching in high-energy heavy-ion collisions. 2015. arXiv:1511.00790.

[62] Jean-Yves Ollitrault. Anisotropy as a signature of transverse collective flow. *Phys. Rev.*, D46:229–245, 1992.

[63] Arthur M. Poskanzer and S. A. Voloshin. Methods for analyzing anisotropic flow in relativistic nuclear collisions. *Phys. Rev.*, C58:1671–1678, 1998.

[64] K. H. Ackermann et al. Elliptic flow in Au + Au collisions at (S(NN))**(1/2) = 130 GeV. *Phys. Rev. Lett.*, 86:402–407, 2001.

[65] E. L. Feinberg. Direct Production of Photons and Dileptons in Thermodynamical Models of Multiple Hadron Production. *Nuovo Cim.*, A34:391, 1976.

[66] Simon Turbide, Ralf Rapp, and Charles Gale. Hadronic production of thermal photons. *Phys. Rev.*, C69:014903, 2004.

[67] S. S. Adler et al. Centrality dependence of direct photon production in s(NN)**(1/ 2) = 200-GeV Au + Au collisions. *Phys. Rev. Lett.*, 94:232301, 2005.

[68] A. Adare et al. Centrality dependence of low-momentum direct-photon production in Au+Au collisions at $\sqrt{s_{NN}}$ = 200 GeV. *Phys. Rev.*, C91(6):064904, 2015.

[69] S. Afanasiev et al. Measurement of Direct Photons in Au+Au Collisions at $\sqrt{s_{NN}}$=200 GeV. *Phys. Rev. Lett.*, 109:152302, 2012.

[70] A. Adare et al. Detailed measurement of the e^+e^- pair continuum in $p + p$ and Au+Au collisions at $\sqrt{s_{NN}}$ = 200 GeV and implications for direct photon production. *Phys. Rev.*, C81:034911, 2010.

[71] Norman M. Kroll and Walter Wada. Internal pair production associated with the emission of high-energy gamma rays. *Phys. Rev.*, 98:1355–1359, Jun 1955.

[72] M. Asakawa and T. Hatsuda. J / psi and eta(c) in the deconfined plasma from lattice QCD. *Phys. Rev. Lett.*, 92:012001, 2004.

[73] K. Adcox et al. Measurement of single electrons and implications for charm production in Au+Au collisions at $\sqrt{s}$(NN) = 130 GeV. *Phys. Rev. Lett.*, 88:192303, 2002.

150

[74] S. S. Adler et al. Centrality dependence of charm production from single electrons measurement in Au + Au collisions at $\sqrt{s_{NN}} = 200$ GeV. *Phys. Rev. Lett.*, 94:082301, 2005.

[75] A. Adare et al. Measurement of high-p(T) single electrons from heavy-flavor decays in p+p collisions at s**(1/2) = 200-GeV. *Phys. Rev. Lett.*, 97:252002, 2006.

[76] B. I. Abelev et al. Transverse momentum and centrality dependence of high-p_T non-photonic electron suppression in Au+Au collisions at $\sqrt{s_{NN}} = 200$ GeV. *Phys. Rev. Lett.*, 98:192301, 2007. [Erratum: Phys. Rev. Lett.106,159902(2011)].

[77] D. Acosta et al. Measurement of prompt charm meson production cross sections in $p\bar{p}$ collisions at $\sqrt{s} = 1.96$ TeV. *Phys. Rev. Lett.*, 91:241804, 2003.

[78] Matteo Cacciari and Paolo Nason. Charm cross-sections for the Tevatron Run II. *JHEP*, 09:006, 2003.

[79] B. A. Kniehl, G. Kramer, I. Schienbein, and H. Spiesberger. Reconciling open charm production at the Fermilab Tevatron with QCD. *Phys. Rev. Lett.*, 96:012001, 2006.

[80] R Aaij et al. Prompt charm production in pp collisions at sqrt(s)=7 TeV. *Nucl. Phys.*, B871:1–20, 2013.

[81] Georges Aad et al. Measurement of $D^{*+/-}$ meson production in jets from pp collisions at sqrt(s) = 7 TeV with the ATLAS detector. *Phys. Rev.*, D85:052005, 2012.

[82] Betty Abelev et al. Measurement of charm production at central rapidity in proton-proton collisions at $\sqrt{s} = 2.76$ TeV. *JHEP*, 07:191, 2012.

[83] Michelangelo L. Mangano, Paolo Nason, and Giovanni Ridolfi. Heavy quark correlations in hadron collisions at next-to-leading order. *Nucl. Phys.*, B373:295–345, 1992.

[84] Matteo Cacciari, Stefano Frixione, Nicolas Houdeau, Michelangelo L. Mangano, Paolo Nason, and Giovanni Ridolfi. Theoretical predictions for charm and bottom production at the LHC. *JHEP*, 10:137, 2012.

[85] D. Acosta et al. Measurement of the J/ψ meson and $b-$hadron production cross sections in $p\bar{p}$ collisions at $\sqrt{s} = 1960$ GeV. *Phys. Rev.*, D71:032001, 2005.

[86] M. Cacciari, S. Frixione, M. L. Mangano, P. Nason, and G. Ridolfi. QCD analysis of first b cross-section data at 1.96-TeV. *JHEP*, 07:033, 2004.

[87] Bernd A. Kniehl, Gustav Kramer, Ingo Schienbein, and Hubert Spiesberger. Finite-mass effects on inclusive B meson hadroproduction. *Phys. Rev.*, D77:014011, 2008.

[88] C. Albajar et al. Beauty production at the CERN p anti-p collider. *Phys. Lett.*, B256:121–128, 1991. [Erratum: Phys. Lett.B262,497(1991)].

[89] R. Aaij et al. Measurement of $\sigma(pp \to b\bar{b}X)$ at $\sqrt{s} = 7$ TeV in the forward region. *Phys. Lett.*, B694:209–216, 2011.

[90] Vardan Khachatryan et al. Prompt and non-prompt J/ψ production in pp collisions at $\sqrt{s} = 7$ TeV. *Eur. Phys. J.*, C71:1575, 2011.

[91] Betty Bezverkhny Abelev et al. Beauty production in pp collisions at $\sqrt{s} = 2.76$ TeV measured via semi-electronic decays. *Phys. Lett.*, B738:97–108, 2014.

[92] E. Norrbin and T. Sjostrand. Production and hadronization of heavy quarks. *Eur. Phys. J.*, C17:137–161, 2000.

[93] S. S. Adler et al. J/ψ production from proton proton collisions at $\sqrt{s} = 200$-GeV. *Phys. Rev. Lett.*, 92:051802, 2004.

[94] A. Adare et al. Energy Loss and Flow of Heavy Quarks in Au+Au Collisions at $\sqrt{s_{NN}} = 200$ GeV. *Phys. Rev. Lett.*, 98:172301, 2007.

[95] Nestor Armesto, Matteo Cacciari, Andrea Dainese, Carlos A. Salgado, and Urs Achim Wiedemann. How sensitive are high-p(T) electron spectra at RHIC to heavy quark energy loss? *Phys. Lett.*, B637:362–366, 2006.

[96] R. Baier, Yuri L. Dokshitzer, Alfred H. Mueller, S. Peigne, and D. Schiff. Radiative energy loss and p(T) broadening of high-energy partons in nuclei. *Nucl. Phys.*, B484:265–282, 1997.

[97] Hendrik van Hees, Vincenzo Greco, and Ralf Rapp. Heavy-quark probes of the quark-gluon plasma at RHIC. *Phys. Rev.*, C73:034913, 2006.

[98] G. D. Moore and D. Teaney. How much do heavy quarks thermalize in a heavy ion collision? *Phys. Rev. C*, 71:064904, 2005.

[99] A. Adare et al. System-size dependence of open-heavy-flavor production in nucleus-nucleus collisions at $\sqrt{s_{NN}}$=200 GeV. *Phys. Rev. C*, 90(3):034903, 2014.

[100] A. Adare et al. Quadrupole Anisotropy in Dihadron Azimuthal Correlations in Central d+Au Collisions at $\sqrt{s_{NN}}$=200 GeV. *Phys. Rev. Lett.*, 111(21):212301, 2013.

[101] Serguei Chatrchyan et al. Observation of long-range near-side angular correlations in proton-lead collisions at the LHC. *Phys. Lett.*, B718:795–814, 2013.

[102] Leonardo Milano. Long-range angular correlations at the LHC with ALICE. *Nucl. Phys.*, A931:1017–1021, 2014.

[103] Kevin Dusling and Raju Venugopalan. Azimuthal collimation of long range rapidity correlations by strong color fields in high multiplicity hadron-hadron collisions. *Phys. Rev. Lett.*, 108:262001, 2012.

[104] Kevin Dusling and Raju Venugopalan. Explanation of systematics of CMS p+Pb high multiplicity di-hadron data at $\sqrt{s}_{\mathrm{NN}} = 5.02$ TeV. *Phys. Rev.*, D87(5):054014, 2013.

[105] Kevin Dusling and Raju Venugopalan. Comparison of the color glass condensate to dihadron correlations in proton-proton and proton-nucleus collisions. *Phys. Rev.*, D87(9):094034, 2013.

[106] T. Sjostrand, S. Mrenna, and P. Z. Skands. PYTHIA 6.4 Phys. and Manual. J. High Energy Phys. **05 (2006)** 026.

[107] Andre Mischke. A New correlation method to identify and separate charm and bottom production processes at RHIC. *Phys. Lett.*, B671:361–365, 2009.

[108] L. Adamczyk et al. Measurements of D^0 and D^* Production in $p + p$ Collisions at $\sqrt{s} = 200$ GeV. *Phys. Rev.*, D86:072013, 2012.

[109] M. Anderson et al. The Star time projection chamber: A Unique tool for studying high multiplicity events at RHIC. *Nucl. Instrum. Meth.*, A499:659–678, 2003.

[110] Joachim Schambach. Proposed STAR time of flight readout electronics and DAQ. *eConf*, C0303241:MOGT006, 2003.

[111] B. B. Abelev et al. Azimuthal anisotropy of D meson production in Pb-Pb collisions at $\sqrt{s_{NN}}$=2.76 TeV. *Phys. Rev. C*, 90(3):034904, 2014.

[112] B. Abelev et al. Suppression of high transverse momentum D mesons in central Pb-Pb collisions at $\sqrt{s_{NN}}$=2.76 TeV. *J. High Energy Phys.* **09 (2012)** 112.

[113] R. Aaij et al. Measurement of the $B^{\pm}$ production cross-section in *pp* collisions at $\sqrt{s} = 7$ TeV. *JHEP*, 04:093, 2012.

[114] Vardan Khachatryan et al. Study of B Meson Production in pPb Collisions at $\sqrt{s_{\mathrm{NN}}} = = 5.02$ TeV. 2015. CMS-HIN-14-004, CERN-PH-EP-2015-209.

[115] S. Chatrchyan et al. Suppression of nonprompt J/ψ, prompt J/ψ, and Y(1S) in PbPb collisions at $\sqrt{s_{NN}}$=2.76 TeV. *J. High Energy Phys.* **05 (2012)** 063.

[116] S. Chatrchyan et al. Evidence of b-Jet Quenching in PbPb Collisions at $\sqrt{s_{NN}}$=2.76 TeV. *Phys. Rev. Lett.*, 113(13):132301, 2014. [Erratum: Phys. Rev. Lett. **115**, 029903 (2015)].

[117] Georges Aad et al. Measurement of the jet radius and transverse momentum dependence of inclusive jet suppression in lead-lead collisions at $\sqrt{s_{NN}}=$ 2.76 TeV with the ATLAS detector. *Phys. Lett.*, B719:220–241, 2013.

[118] R. Baier, Yuri L. Dokshitzer, S. Peigne, and D. Schiff. Induced gluon radiation in a QCD medium. *Phys. Lett.*, B345:277–286, 1995.

[119] S. Cao, G.-Y. Qin, and S. A. Bass. Heavy-quark dynamics and hadronization in ultrarelativistic heavy-ion collisions: Collisional versus radiative energy loss. *Phys. Rev. C*, 88(4):044907, 2013.

[120] Ralf Rapp and Hendrik van Hees. Heavy Quarks in the Quark-Gluon Plasma. In *R. C. Hwa, X.-N. Wang (Ed.) Quark Gluon Plasma 4, World Scientific, 111 (2010)*, 2009. arXiv:0903.1096.

[121] H. van Hees, M. Mannarelli, V. Greco, and R. Rapp. Nonperturbative heavy-quark diffusion in the quark-gluon plasma. *Phys. Rev. Lett.*, 100:192301, 2008.

[122] P. B. Gossiaux, J. Aichelin, T. Gousset, and V. Guiho. Competition of Heavy Quark Radiative and Collisional Energy Loss in Deconfined Matter. *J. Phys. G*, 37:094019, 2010.

[123] A. M. Adare, M. P. McCumber, James L. Nagle, and P. Romatschke. Examination whether heavy quarks carry information on the early-time coupling of the quark-gluon plasma. *Phys. Rev. C*, 90(2):024911, 2014.

[124] H. van Hees, M. Mannarelli, V. Greco, and R. Rapp. T-matrix approach to heavy quark diffusion in the QGP. *Eur. Phys. J. C*, 61:799, 2009.

[125] S. Cao, G.-Y. Qin, and S. A. Bass. Model and parameter dependence of heavy quark energy loss in a hot and dense medium. *J. Phys. G*, 40:085103, 2013.

[126] W. M. Alberico, A. Beraudo, A. De Pace, A. Molinari, M. Monteno, M. Nardi, and F. Prino. Heavy-flavour spectra in high energy nucleus-nucleus collisions. *Eur. Phys. J. C*, 71:1666, 2011.

[127] M. He, R. J. Fries, and R. Rapp. Heavy Flavor at the Large Hadron Collider in a Strong Coupling Approach. *Phys. Lett. B*, 735:445, 2014.

[128] Gert Aarts, Chris Allton, Mehmet Bugrahan Oktay, Mike Peardon, and Jon-Ivar Skullerud. Charmonium at high temperature in two-flavor QCD. *Phys. Rev.*, D76:094513, 2007.

[129] Swagato Mukherjee, Peter Petreczky, and Sayantan Sharma. Charm Degrees of Freedom in Quark Gluon Plasma. 2015. arXiv:1509.08887.

[130] Azfar Adil and Ivan Vitev. Collisional dissociation of heavy mesons in dense QCD matter. *Phys.Lett.*, B649:139–146, 2007.

[131] O. Kaczmarek, F. Karsch, P. Petreczky, and F. Zantow. Heavy quark free energies, potentials and the renormalized Polyakov loop. *Nucl. Phys. Proc. Suppl.*, 129:560–562, 2004. [,560(2003)].

[132] Olaf Kaczmarek, Shinji Ejiri, Frithjof Karsch, Edwin Laermann, and Felix Zantow. Heavy quark free energies and the renormalized Polyakov loop in full QCD. *Prog. Theor. Phys. Suppl.*, 153:287–294, 2004.

[133] M. Djordjevic, M. Gyulassy, R. Vogt, and S. Wicks. Influence of bottom quark jet quenching on single electron tomography of Au + Au. *Phys. Lett. B*, 632:81, 2006.

[134] M. Djordjevic and M. Djordjevic. Heavy flavor puzzle from data measured at the BNL Relativistic Heavy Ion Collider: Analysis of the underlying effects. *Phys. Rev. C*, 90(3):034910, 2014.

[135] Magdalena Djordjevic and Miklos Gyulassy. Heavy quark radiative energy loss in QCD matter. *Nucl. Phys.*, A733:265–298, 2004.

[136] Satoshi Ozaki and Thomas Roser. Relativistic Heavy Ion Collider, its construction and upgrade. *PTEP*, 2015(3):03A102, 2015.

[137] K. Adcox et al. PHENIX detector overview. *Nucl. Instrum. Methods Phys. Res., Sec. A*, 499:469, 2003.

[138] Mingxiu Sun J.T. Mitchell, Mike Dai. PHENIX Analysis Note 1076 - Centrality Calibration for the Run-11 200 GeV Au+Au Dataset .

[139] S. H. Aronson et al. PHENIX magnet system. *Nucl. Instrum. Meth.*, A499:480–488, 2003.

[140] Y. Akiba et al. Ring imaging Cherenkov detector of PHENIX experiment at RHIC. *Nucl. Instrum. Meth.*, A433:143–148, 1999.

[141] L. Aphecetche et al. PHENIX calorimeter. *Nucl. Instrum. Meth.*, A499:521–536, 2003.

[142] M. M. Aggarwal et al. Centrality dependence of neutral pion production in 158-A-GeV Pb-208 + Pb-208 collisions. *Phys. Rev. Lett.*, 81:4087–4091, 1998. [Erratum: Phys. Rev. Lett.84,578(2000)].

[143] Stephen Scott Adler et al. PHENIX on-line systems. *Nucl. Instrum. Meth.*, A499:560–592, 2003.

[144] Rachid Nouicer. Probing Hot and Dense Matter with Charm and Bottom Measurements with PHENIX VTX Tracker. *Nucl. Phys. A*, 904-905:647c, 2013.

[145] M. Kurosawa. Higher harmonics flow measurement of charged hadrons and electrons in wide kinematic range with PHENIX VTX tracker. *Nucl. Phys. A*, 904-905:397c, 2013.

[146] R. Ichimiya et al. Status and overview of development of the Silicon Pixel Detector for the PHENIX experiment at the BNL RHIC. *J. Inst.*, 4:P05001, 2009. and references therein.

[147] W. Snoeys et al. Pixel readout chips in deep submicron CMOS for ALICE and LHCb tolerant to 10-Mrad and beyond. In *Development and application of semiconductor tracking detectors. Proceedings, 4th International Symposium, Hiroshima, Japan, March 22-25, 2000*, volume 466, page 366, 2001.

[148] Y. Onuki et al. Assembly procedure for the silicon pixel ladder for PHENIX silicon vertex tracker. *Nucl. Instrum. Meth.*, A606:395–403, 2009.

[149] Z. Li et al. Novel silicon stripixel detector for PHENIX upgrade. *Nucl. Instrum. Methods Phys. Res., Sec. A*, 518:300, 2004.

[150] R. Nouicer et al. Status and Performance of New Silicon Stripixel Detector for the PHENIX Experiment at RHIC: Beta Source, Cosmic-rays, and Proton Beam at 120 GeV. *J. Inst.*, 4:P04011, 2009. and references therein.

[151] Rachid Nouicer. PHENIX Upgrade: Novel Stripixel Detector for Heavy Quark Detection and Proton Spin Structure Measurements at RHIC Energies. 2007. [Nucl. Instrum. Meth.B261,1067(2007)].

[152] B. Krieger et al. SVX4: A New Deep-Submicron Readout IC for the Tevatron Collider at Fermilab. *IEEE Trans. Nucl. Sci.*, 51:1968–1973, 2004.

[153] M. Garcia-Sciveres et al. The SVX4 integrated circuit. *Nucl. Instrum. Methods Phys. Res., Sec. A*, 511:171, 2003.

[154] GEANT 3.2.1 Manual (CERN, Geneva, 1993).

[155] X.-N. Wang and M. Gyulassy. HIJING: A Monte Carlo model for multiple jet production in pp, pA and AA collisions. *Phys. Rev. D*, 44:3501, 1991.

[156] Rhohji Akimoto. *Measurement of Charms and Bottoms with Semi-Leptonic Decay Modes p+p Collisions at $\sqrt{s_{NN}} = 200\ GeV$*. PhD thesis, University of Tokyo, 2014.

[157] A. Adare et al. Suppression pattern of neutral pions at high transverse momentum in Au + Au collisions at $\sqrt{s_{NN}} = 200$ GeV and constraints on medium transport coefficients. *Phys. Rev. Lett.*, 101:232301, 2008.

[158] A. Adare et al. Transverse momentum dependence of meson suppression η suppression in Au+Au collisions at $\sqrt{s_{NN}} = 200$ GeV. *Phys. Rev. C*, 82:011902, 2010.

[159] A. Adare et al. J/ψ Production vs Centrality, Transverse Momentum, and Rapidity in Au+Au Collisions at $\sqrt{s_{NN}}=200$ GeV. *Phys. Rev. Lett.*, 98:232301, 2007.

[160] S. S. Adler et al. Common suppression pattern of eta and pi0 mesons at high transverse momentum in Au+Au collisions at S(NN)**(1/2) = 200-GeV. *Phys. Rev. Lett.*, 96:202301, 2006.

[161] G. Cowan. A survey of unfolding methods for particle physics. *Conf. Proc. C*, 0203181:248, 2002.

[162] G. Choudalakis. Fully Bayesian Unfolding. arXiv:1201.4612.

[163] Goodman, J. and Weare, J. Ensemble samplers with affine invariance. *Comm. App. Math. Comp. Sci.*, 5:65, 2010.

[164] D. Foreman-Mackey, D. W. Hogg, D. Lang, and J. Goodman. emcee: The MCMC Hammer. *Publ. Astron. Soc. Pac.*, 125:306, 2013.

[165] P. Staszel. Recent results from the BRAHMS experiment. *Nucl. Phys. A*, 774:77, 2006.

[166] B. I. Abelev et al. Identified baryon and meson distributions at large transverse momenta from Au+Au collisions at $\sqrt{s_{NN}} = 200$ GeV. *Phys. Rev. Lett.*, 97:152301, 2006.

[167] G. Martinez-Garcia, S. Gadrat, and P. Crochet. Consequences of a Lambda(c)/D enhancement effect on the nonphotonic electron nuclear modification factor in central heavy ion collisions at RHIC energy. *Phys. Lett. B*, 663:55, 2008. [Erratum: Phys. Lett. B **666**, 533 (2008)].

[168] P. R. Sorensen and X. Dong. Suppression of nonphotonic electrons from enhancement of charm baryons in heavy ion collisions. *Phys. Rev. C*, 74:024902, 2006.

[169] Magdalena Djordjevic. Collisional energy loss in a finite size QCD matter. *Phys. Rev.*, C74:064907, 2006.

[170] Rishi Sharma, Ivan Vitev, and Ben-Wei Zhang. Light-cone wave function approach to open heavy flavor dynamics in QCD matter. *Phys. Rev.*, C80:054902, 2009.

[171] Zhong-Bo Kang, Ivan Vitev, and Hongxi Xing. Nuclear modification of high transverse momentum particle production in p+A collisions at RHIC and LHC. *Phys. Lett.*, B718:482–487, 2012.

[172] Kyle Huggins and Ralf Rapp. A T-Matrix Calculation for in-Medium Heavy-Quark Gluon Scattering. *Nucl. Phys.*, A896:24–45, 2012.

[173] Min He, Rainer J. Fries, and Ralf Rapp. Ideal Hydrodynamics for Bulk and Multistrange Hadrons in $\sqrt{s_{NN}}$=200 AGeV Au-Au Collisions. *Phys. Rev.*, C85:044911, 2012.

[174] Min He, Rainer J. Fries, and Ralf Rapp. Thermal Relaxation of Charm in Hadronic Matter. *Phys. Lett.*, B701:445–450, 2011.

[175] Min He. private communication.

[176] I. Vitev, A. Adil, and H. van Hees. Novel heavy flavor suppression mechanisms in the QGP. *J. Phys. G*, 34:S769, 2007.

[177] W. A. Horowitz. Fluctuating heavy quark energy loss in a strongly coupled quark-gluon plasma. *Phys. Rev. D*, 91(8):085019, 2015.

[178] W. A. Horowitz. Shock Treatment: Heavy Quark Energy Loss in a Novel AdS/CFT Geometry. *Nucl. Phys. A*, 830:773C, 2009.

[179] Y.Akiba et al. PHENIX Analysis Note 415 - Non-photonic electrons from Au+Au collisions at $\sqrt{sNN}$ = 200 GeV (Run-4) .

[180] F.W. Busser, L. Camilleri, L. Di Lella, B.G. Pope, A.M. Smith, et al. A Measurement of Single Electrons, electron Pairs, and Associated Phenomena, in Proton Proton Collisions at the CERN ISR. *Nucl.Phys.*, B113:189, 1976.

[181] Alan Dion. *Energy Loss and Flow of Heavy Quarks in Au+Au Collisions at $\sqrt{s_{NN}}$ = 200 GeV*. PhD thesis, Stony Brook University, May 2007.

[182] Fukutaro Kajihara. *Measurement of Single Electrons from Semi-Leptonic Decay of Heavy Quarks in Au+Au Collisions at $\sqrt{s_{NN}}$ = 200 GeV*. PhD thesis, University of Tokyo, 2007.